

UCSF

UC San Francisco Electronic Theses and Dissertations

Title

TGF-beta and glucocorticoids regulate bone matrix mechanical properties and composition

Permalink

<https://escholarship.org/uc/item/5473t22v>

Author

Balooch, Guive

Publication Date

2006

Peer reviewed|Thesis/dissertation

TGF-beta and glucocorticoids regulate bone matrix mechanical properties and composition

by

Guive Balooch

DISSERTATION

Submitted in partial satisfaction of the requirements for the degree of

DOCTOR OF PHILOSOPHY

in

Oral and Craniofacial Sciences

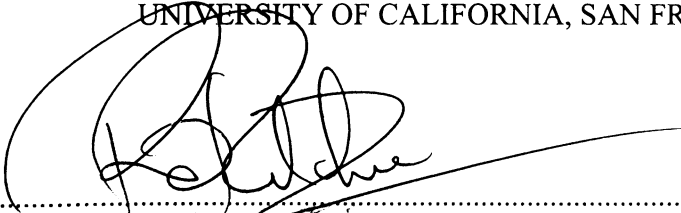
in the

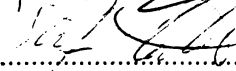
GRADUATE DIVISION

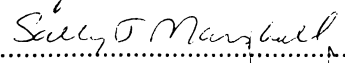
of the

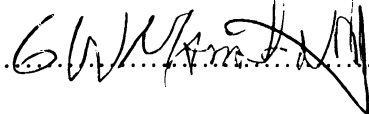
UNIVERSITY OF CALIFORNIA, SAN FRANCISCO

Approved:









Committee in Charge

Deposited in the Library, University of California, San Francisco

.....
Date

University Librarian

Degree Conferred:.....

Acknowledgments

My deepest thanks to my father, Dr. Mehdi Balooch, who has taught and mentored me throughout all of my academic years and to whom I owe an infinite amount of gratitude. I would like to give my warmest thanks to Dr. Grayson W. Marshall and Dr. Sally J. Marshall for guiding me, supporting my research, and most importantly, always supporting me during both my undergraduate and graduate career. I will always be grateful to all three of you.

The past four years that I have been a PhD student at UCSF, I have had the honor of collaborating and being mentored by amazing researchers in both biological sciences as well as physical sciences. I would specifically like to thank Dr. Rik Derynck for whom I have enormous respect and from whom I have learned a great deal, for all of his thoughtful conversations and mentoring. In addition, I would like to thank Dr. Tamara Alliston (UCSF), Dr. Robert O. Ritchie (UC Berkeley), and Dr. Ravi K. Nalla (UC Berkeley) from whom I have learned an enormous amount; and for this I am grateful. I would also like to thank all the members of the Marshall's Lab without whom I would not have been able to complete many of my studies: Grace Nonomura, Dr. Stefan Habelitz, Dr. Sunita Ho, Megan Pugach, Dr. Jim Strother, and all others.

Finally, I would like to thank the NIH/NIDCR, my advisor, and my dissertation committee: Dr. Grayson W. Marshall, Dr. Sally J. Marshall, Dr. Stefan Habelitz, and Dr. Robert O. Ritchie.

A special thanks to my mom, and my fiancé, Shabnam Zartoshtimanesh.

There are many more people I would like to thank that would not fit on one page. I apologize for not mentioning everyone.

I dedicate this work to my father

TGF- β and Glucocorticoids regulate bone matrix mechanical properties and composition

By Guive Balooch

Abstract

The ability of bone to resist fracture is determined by bone mass and architecture, and the mechanical properties and composition of bone matrix. Several signaling pathways, including glucocorticoids (GCs), and Transforming Growth Factor- β (TGF- β), are involved in the control of bone mass and architecture. Presumably bone matrix mechanical properties are highly regulated; however, the regulators themselves remain unknown. We hypothesized that TGF- β and GCs regulate mechanical properties and composition of bone matrix: including elastic modulus, fracture toughness, and bone mineral concentration (BMC).

Our group designed and utilized bones from mice treated with GCs and mice with different levels of TGF- β to evaluate local mechanical properties using atomic force microscopy and elastic modulus mapping, fracture toughness using three-point bending, and BMC using synchrotron x-ray tomography (XTM). We found that mice with elevated TGF- β signaling had reduced elastic modulus (E) and increased heterogeneity of local mechanical properties while mice in which TGF- β signaling was impaired had increased E compared to wild-type (WT) littermates. Partially inhibiting TGF- β signaling led to increased bone volume/total volume (BV/TV), increased cortical thickness, and increased BMC relative to WT. Similar to mice with elevated levels of TGF- β , GC-treated mice

showed local variation in mechanical properties surrounding osteocyte lacunae that was not seen in controls. Both in GC-treated mice as well as mice with elevated TGF- β signaling, heterogeneity in localized mechanical properties led to changes in macroscopic parameters as well.

Therefore, by evaluating mice treated with GCs, we found that localized mechanical properties play a key role in determining bone fragility, in combination with known effects of GCs on macro-structure and architecture. In addition, partial reduction of TGF- β signaling in bone is sufficient to produce bone with increased cortical thickness, structural bone parameters, mineral content and local mechanical properties, enabling these bones to better resist fracture. The implications of the effects of reduced TGF- β signaling on mechanical properties suggest possible therapeutic applications as TGF- β inhibitors are currently in clinical trials for breast metastasis. Future research will involve investigating whether partially inhibiting TGF- β chemically using TGF- β RI Kinase inhibitors can be considered as a therapeutic target to treat bone disorders.

Dr. Grayson W. Marshall (Dissertation committee Chair)

Table of Contents

	Page
Chapter 1. Introduction	1
Chapter 2. Micro-Raman spectroscopic investigation of dental calcified tissues	14
Chapter 3. Evaluation of a new modulus mapping technique to investigate microstructural features of human teeth	39
Chapter 4. Glucocorticoid treated mice have localized changes in trabecular bone material properties and osteocyte lacunar size that are not observed in placebo treated or estrogen deficient mice	68
Chapter 5. TGF- β regulates the mechanical properties and composition of bone matrix	110
Chapter 6. Conclusion and future work	140

5
0
SC
Y
C
SC
Y
CITY
C
SC
Y
CITY
C
SC
Y
CITY
C
SC
Y
CITY
C

Table of Tables

	Page
Chapter 2. Table 1.	31
Chapter 3. Table 1.	57
Chapter 4. Table 1.	101
Table 2.	102
Table 3.	103
Table 4.	104
Chapter 5. Table 1.	134

Table of Figures

	Page
Chapter 2. Figure 1.	32
Figure 2.	33
Figure 3.	34
Figure 4.	35
Figure 5.	36
Figure 6.	37
Figure 7.	38
Chapter 3. Figure 1.	58
Figure 2.	59
Figure 3.	60
Figure 4.	61
Figure 5.	62
Figure 6.	63
Figure 7.	64
Figure 8.	65
Figure 9.	66
Figure 10.	67
Chapter 4. Figure 1.	105-106
Figure 2.	107-108

	Figure 3.	109
Chapter 5.	Figure 1.	135
	Figure 2.	136
	Figure 3.	137
	Figure 4.	138
	Figure 5.	139

Chapter 1

Introduction

Skeletal development and homeostasis are regulated by growth factors and hormones, which regulate cell differentiation, cell function, and matrix deposition. Presumably bone matrix mechanical properties and composition are highly regulated, but the signaling molecules or pathways regulating them are largely unknown. In addition, the effects of growth factors and hormones on local and macro-mechanical properties of bone have not been studied extensively; however, their clinical relevance is obvious. For example, even with normal or elevated bone mass, individuals with osteogenesis imperfecta or osteopetrosis have higher incidence of bone fracture (1, 2). Therefore, in addition to structural factors, local mechanical properties and composition of bone and teeth most likely play key roles in ultimately determining when fractures will occur.

One group of extracellular signaling molecules, which is present in bone, is the transforming growth factor- β (TGF- β) family of cytokines. TGF- β 2, one member of this family, is expressed in all bone formation stages and has a complex but vital role in osteoblast proliferation, differentiation, and subsequent calcification of the bone matrix (3-5). TGF- β 2's regulation of gene expression is mediated by Smad3, a direct substrate of the TGF- β I receptor, which has been shown to be crucial in TGF- β signaling by binding with coactivators and corepressors, leading to inhibition of osteoblast differentiation markers, such as Runx2 (6, 7).

Bone architecture is, in part, determined by cortical bone thickness, trabecular bone volume and organization, and is regulated by a variety of cytokines and hormones. The complex biological role of TGF- β signaling on osteoblast proliferation and differentiation has been studied *in vitro* and *in vivo*; however, whether these events lead to regulation of the mechanical properties of the bone matrix itself, is still unknown.

Accordingly, transgenic mice with targeted alterations in the expression of defined cytokines, such as TGF- β and interleukin 6, show alterations in bone mass and architecture (8). Local mechanical properties of bone matrix are independent of bone mass and architecture and presumably bone matrix mechanical properties are highly regulated, but the signaling molecules or pathways regulating them are largely unknown. The central hypothesis of this thesis is that TGF- β signaling and glucocorticoids regulate local mechanical properties and composition of the bone matrix, ultimately leading to changes in whole bone mechanical properties.

The scope of this thesis work

Initially, our main goal was to investigate site-specific mechanical properties in an appropriate biological environment. Teeth provided a suitable system to determine these properties, as all previous assessments of the width of small interfaces in the tooth, such as the dentin-enamel junction and cementum-dentin junction, seemed to be probe size dependent. The investigation of these interfaces in the tooth is of great clinical relevance since such interfaces have special characteristics that allow them to withstand loads sufficiently and arrest cracks. By utilizing techniques with high spatial resolution (down to 15 nm), we accurately assessed the chemical (Chapter 2) and mechanical (Chapter 3) property variations near these junctions in addition to accurately determining their widths. Several of the calcified tissues in teeth, such as dentin and cementum, have very similar overall compositions to bone, although the microstructures vary greatly. Thus, after investigating the local mechanical and compositional properties of teeth, we expanded this to a highly abundant mineralized tissue in the body: bone. Our interest was

in determining whether local mechanical properties and composition of bone matrix can be regulated by various hormones and growth factors that are present in bone. This led to the bulk of this thesis work, Chapters 4 and 5, where the effect of the growth factor TGF- β and the glucocorticoid hormone family on local mechanical properties and matrix composition of mouse bone were assessed.

Background

Mechanical properties and structure of bone and teeth

Dentin, enamel and cementum formation involves a remarkable orchestration of complex molecular and cellular events that culminate in uniquely structured tissues joined at distinctive interfaces. The dentin-enamel junction (DEJ) is a complex and critical structure uniting the highly mineralized harder enamel with the less mineralized tougher and softer dentin. It plays a critical role as the initiation surface for ameloblastic and odontoblastic activity during tooth formation (9). In maturity, it appears to be critical to the biomechanical integrity of the tooth (10), because it joins these structurally diverse calcified tissues. The structure of the DEJ is generally described as scalloped with its convexities directed toward the dentin and concavities directed toward the enamel (11). The scallops house microscalops that contain finer nano-scale structures (12, 13). The scallops and the presence of a smooth gradient of mechanical properties at the junction are believed to contribute to an important toughening mechanism that reduces stress concentrations. This gradation of properties is initiated by a biomineralization process starting from the DEJ in both directions. Until recently, the nature of the cementum-dentin junction (CDJ) was quite controversial, whether it is a form of dentin, cementum,

or a tissue in its own right. This layer has been called “interzonal layer” (14), “intermediate layer of cementum” (15) and “intermediate cementum” (16). Studies on the CDJ have been mostly of histological nature and only a few physical properties of cementum have been investigated (17). However, recently Ho and colleagues reported several studies on the microscale and nanoscale mechanical and chemical properties of the CDJ (18-20). It was shown that there is an 80-200 μm wide interface between cementum and dentin, consisting of a 70-100 μm wide root mantle dentin and a 10-50 μm wide hydrophilic cementum-dentin junction (18, 19). It was also shown that the CDJ contains glycosaminoglycans in addition to the collagen fibrils that many believed was the exclusive protein comprising the CDJ (20). Aside from these 3 recent studies on the CDJ, several other mechanical properties studies and conventional morphological studies have been conducted on the DEJ and the CDJ. The techniques used lack the ability to obtain chemically related information. Mechanical property investigations are frequently limited based on the probe size used to assess them in Chapters 2 and 3, we utilized several high-resolution biomechanical techniques to investigate the local mechanical properties and chemistry of the CDJ and DEJ.

Bone tissue is anisotropic and has hierarchical structural organization. Bone, as well as dentin, consists of mineralized collagen fibrils that comprises approximately 90% of the organic matrix. These molecules then self-assemble into thin (10-300 nm in diameter) collagen fibrils, and often aggregate into large fibers that can be several micrometers in diameter, ultimately leading to the lamellar woven bone macro-structure. In addition to bone mass and architecture, the extracellular matrix plays a key role in determining overall bone fracture resistance. Two local mechanical properties that can be

measured on a nano-scale are elastic modulus and hardness. The elastic modulus is a measure of the stiffness of the bone and is a characteristic material property, whereas the hardness is an indication of its strength, specifically its resistance to plastic deformation under pressure (21). Inherent in every hard material or tissue, such as bone, are microcracks, which do not play a large role in determining local mechanical properties, but can affect the macroscopic mechanical properties as they propagate in the presence of stress and lead to ultimate fracture (22). Two macroscopic mechanical properties of bone are work of fracture and fracture toughness. Fracture toughness indicates the maximum stress intensity that the bone can resist before initiating fracture from a notch (a pre-crack), whereas “work of fracture” corresponds to the total energy required to break the bone (22). The anisotropy seen in bone leads to a much more complex relationship between mechanical properties than in homogeneous materials; therefore, the assessment of one or two mechanical properties in genetically engineered mice may be deceiving. For example, in the human tooth, the elastic modulus of enamel is very high; however, it is brittle, which would not be revealed by a simple hardness test. In addition, many times materials with high strength have compromised toughness. Therefore, as shown in Chapters 4 and 5, it is crucial to consider several different mechanical properties to fully understand the behavior of bone under load.

Multiple test strategies are needed for accurate assessment of the effects of TGF- β signaling and the glucocorticoid hormone family on overall bone matrix mechanical integrity. In addition to the macro- and microscopic mechanical properties discussed above, the composition of the bone matrix must be considered. In TGF- β signaling, TGF- β /Smad3 can regulate the expression of bone matrix proteins such as osteocalcin,

osteopontin and collagen I, each of which can affect matrix mineralization (23-25). For example, osteocalcin limits the size of apatite crystals and has been shown to increase the resistance to bone fracture (23). Bone sialoprotein regulates initiation of, while osteopontin and osteonectin inhibit apatite crystal formation (24). In this way, the regulation of gene expression in osteoblasts by TGF- β may affect not only the protein composition, but also the mineral concentration and organization of the bone matrix. It is therefore, crucial to have a collective understanding of not only physical structure but overall bone mechanical properties (local and macro) as well as changes in inorganic/organic content and bone mineral concentration. Variations in inorganic/organic ratio can be determined using Raman microspectroscopy while bone mineral concentration can be determined by x-ray tomography (XTM) as in Chapter 5.

Glucocorticoid treatment effects on bone

Glucocorticoid (GC) treatment is widely used among the adult population for a variety of inflammatory conditions and has been shown to be the most common cause of secondary osteoporosis among this population (26). Glucocorticoids alter bone metabolism, which in turn decreases bone density and affects trabecular bone architecture. Patients chronically treated with GCs often suffer significant trabecular bone loss, resulting in fractures in nearly 50% of individuals on long term treatment (27-29). Interestingly, fractures in patients treated with GCs occur at a higher bone density than normal bone (30, 31), suggesting that other factors, such as localized bone mechanical properties and composition, may be playing roles in glucocorticoid-induced bone fragility. Individuals treated with glucocorticoids also have alterations in bone remodeling (27, 31, 32). These

alterations in bone remodeling include an increase in bone resorption and suppression of bone formation such that reductions in trabecular bone mass and architecture occur, including reductions in trabecular thickness and trabecular number (31, 32). The mechanisms behind these changes have been proposed to be alterations in bone cell viability. Glucocorticoids reduce the lifespan of osteoblasts and osteocytes through apoptosis while increasing osteoclast viability (33, 34). While these proposed alterations in bone cell lifespan could explain the reduction in bone formation markers and trabecular bone architecture, neither of these observations completely explains the increased bone fragility observed in glucocorticoid-induced osteoporosis that is not observed with postmenopausal osteoporosis. Therefore, the assessment of localized bone mechanical properties and composition in response to GC treatment may lead to a better understanding of how GCs increase bone fragility. These effects will be studied using the same methods described above as reported in Chapter 4.

TGF- β family and signaling pathway

There are more than 30 members in the TGF- β super-family; in addition to 3 isoforms of TGF- β itself, there are multiple bone morphogenetic proteins (BMPs), growth differentiation factors (GDFs) and activins, which constitute the majority of the family (35). TGF- β 's action in bone is vital but complex as it has differential effects on the multiple events of osteoblast cell life. For example, TGF- β inhibits osteoblast differentiation yet stimulates the proliferation of mesenchymal progenitors and preosteoblasts, thereby allowing an expansion of the progenitor pool of cells that will differentiate into mature osteoblasts (7). TGF- β is stored in an inactive form, released

from the bone matrix, and activated in the bone microenvironment (35, 37). TGF- β signals through a heteromeric cell-surface complex of two type I and two type II transmembrane serine/threonine kinases (38, 39). In response to ligand binding, the type II receptors form a complex with the type I receptors and phosphorylate their cytoplasmic domains, thus activating the type I receptor kinases and leading to activation of intracellular targets of TGF- β signaling (3, 40). Receptor activated Smads (R-Smads), Smads2 and 3, are direct effectors of the TGF- β I receptor, and once activated, act as transcription factors by binding with Smad4 and translocating to the nucleus where, in the presence of coactivators and corepressors, they activate transcription of a defined set of genes critical for bone formation (3). Multiple coactivators exist, of which the most important in osteoblast differentiation is CBP/p300 and multiple corepressors exist, such as c-ski. One critical result of this mechanism is the ability of Smad3, following activation by the TGF- β I receptor, to functionally inhibit the expression of Runx2 (6). Runx2 is a transcription factor that induces the expression of critical osteoblast markers. TGF- β 's inhibition of Runx2, mediated by Smad3, can thereby lead to inhibition of other downstream genes affected by Runx2, such as osteocalcin, collagen type I, and Runx2 itself (6, 25, 41, 42). Although the phosphorylation of R-Smads by the type I receptor is the main mechanism for R-Smad activation, smad activity can be regulated by other kinase pathways as well. For example, the Erk mitogen-activated protein kinase (MAPK) pathway, can target R-Smads by phosphorylating the MHI domain of Smad2 and the linker segments of Smads2 and 3 (3, 43). Smad-independent signaling can occur through MAPK pathways as well (3, 44). For example, TGF- β can activate p38 MAPK signaling independent of smad signaling and regulate TGF- β induced response (44). Inhibitory

Smads, Smad6 and 7, can also regulate the activation of R-Smad signaling by competing for activation by the TGF- β type I receptor, thus preventing recruitment and activation of R-Smads. It has been shown that Smad7 is a stronger inhibitor of TGF- β signaling than Smad6 (3). Although TGF- β signaling itself can regulate I-Smad activation and action, other pathways such as the EGF-induced MAPK activation can regulate Smad6/7 expression independent of TGF- β signaling. Therefore, multiple positive and negative feedback mechanisms regulate TGF- β and Smad signaling action. The complexity of the TGF- β signaling pathway makes it difficult to study and isolate the effect of TGF- β on the mechanical properties and composition of bone using only one mouse model. Therefore, as reported in Chapter 5, we utilized six different mouse models with different levels of TGF- β signaling by using mice with a dominant negative TGF- β receptor, ligand-induced increases in TGF- β levels, as well as systemic loss of Smad3.

UCSF LIBRARY

References

1. Jamsa T, Rho JY, Fan Z, MacKay CA, Marks SC, Jr., Tuukkanen J 2002 Mechanical properties in long bones of rat osteopetrotic mutations. *J Biomech* **35**(2):161-5.
2. Misof K, Landis WJ, Klaushofer K, Fratzl P 1997 Collagen from the osteogenesis imperfecta mouse model (oim) shows reduced resistance against tensile stress. *J Clin Invest* **100**(1):40-5.
3. Derynck R, Zhang YE 2003 Smad-dependent and Smad-independent pathways in TGF-beta family signalling. *Nature* **425**(6958):577-84.
4. Massague J 1998 TGF-beta signal transduction. *Annu Rev Biochem* **67**:753-91.
5. ten Dijke P, Hill CS 2004 New insights into TGF-beta-Smad signalling. *Trends Biochem Sci* **29**(5):265-73.
6. Alliston T, Choy L, Ducy P, Karsenty G, Derynck R 2001 TGF-beta-induced repression of CBFA1 by Smad3 decreases cbfal and osteocalcin expression and inhibits osteoblast differentiation. *Embo J* **20**(9):2254-72.
7. Alliston TN, Derynck R 2000 Transforming Growth Factor-beta in Skeletal Development and Maintenance. In: Canalis E (ed.) *Skeletal Growth Factors*. Lippincott Williams & Wilkins, Philadelphia, pp 233-249.
8. Poli V, Balena R, Fattori E, Markatos A, Yamamoto M, Tanaka H, Ciliberto G, Rodan GA, Costantini F 1994 Interleukin-6 deficient mice are protected from bone loss caused by estrogen depletion. *Embo J* **13**(5):1189-96.
9. Ten Cate AR. *Oral histology: Development, structure, and function*. 4th Ed. St. Louis: Mosby; 1994. p 184-185.
10. Lin CP, Douglas WH. 1994 Structure-property relations and crack resistance at the bovine dentin-enamel junction. *J Dent Res*;73:1072-1078.
11. Bhaskar SN, editor. 1990 *Orban's oral histology and embryology*. 11th Ed. Chicago: Mosby Year Book p 70-71.
12. Marshall GW, Jr., Balooch M, Gallagher RR, Gansky SA, Marshall SJ. 2001 Mechanical properties of the dentinoenamel junction: AFM studies of nanohardness, elastic modulus, and fracture. *J Biomed Mater Res*; 54:87-95.
13. Marshall SJ, Balooch M, Habelitz S, Balooch G, Gallagher R, Marshall GW. 2003 The dentin-enamel junction-a natural, multilevel interface. *J Eur Ceram Soc*; 23:2897-2904.
14. Bodecker CFW. 1957 The distribution of living matter in human dentin, cement and enamel. *Dent Cosmos*; 20:582-590.
15. Bencz L. 1927 Befunde an der Dentinzement Grenze. *Z Stomat*; 5:877-896.
16. Blackwood HJJ. 1957 Intermediate cementum. *Brit Dent J*; 102:345-350.
17. Brear K, Currey JD, Pond CM, Ramsay MA. 1990 The mechanical properties of dentine and cement of the tusk of the narwhal *Monodon monoceros* compared with those of other mineralized tissues. *Arch Oral Biol*; 35:615-621.
18. Ho SP, Balooch M, Goodis HE, Marshall GW, Marshall SJ. 2004 Ultrastructure and nanomechanical properties of cementum dentin junction. *J Biomed Mater Res A*. Feb 1; 68(2): 343-351.

19. Ho SP, Balooch M, Marshall SJ, Marshall GW. 2004 Local properties of a functionally graded interphase between cementum and dentin. *J Biomed Mater Res A*. Sep 1;70(3): 480-9.
20. Ho SP, Sulynato RM, Marshall SJ, Marshall, GW. 2005 The cementum-dentin junction also contains glycosaminoglycans and collagen fibrils. *J Struct Biol*. 151(1): 69-78.
21. Pharr GM, Oliver WC, Brotzen FR 1992 On the generality of the relationship among contact stiffness, contact area, and elastic-modulus during indentation. *Journal of Materials Research* 7(3):613-617.
22. Nalla RK, Kruzic JJ, Ritchie RO 2004 On the origin of the toughness of mineralized tissue: microcracking or crack bridging? *Bone* 34(5):790-8.
23. Harris SE, Bonewald LF, Harris MA, Sabatini M, Dallas S, Feng JQ, Ghosh-Choudhury N, Wozney J, Mundy GR 1994 Effects of transforming growth factor beta on bone nodule formation and expression of bone morphogenetic protein 2, osteocalcin, osteopontin, alkaline phosphatase, and type I collagen mRNA in long-term cultures of fetal rat calvarial osteoblasts. *J Bone Miner Res* 9(6):855-63.
24. Hunter GK, Hauschka PV, Poole AR, Rosenberg LC, Goldberg HA 1996 Nucleation and inhibition of hydroxyapatite formation by mineralized tissue proteins. *Biochem J* 317 (Pt 1):59-64.
25. Rydziel S, Varghese S, Canalis E 1997 Transforming growth factor beta1 inhibits collagenase 3 expression by transcriptional and post-transcriptional mechanisms in osteoblast cultures. *J Cell Physiol* 170(2):145-52.
26. Rehman Q, Lane NE 2003 Effect of glucocorticoids on bone density. *Med Pediatr Oncol* 41(3):212-216
27. Lane NE 2001 An update on glucocorticoid-induced osteoporosis. *Rheum Dis Clin North Am* 27(1):235-253
28. Van Staa TP, Leufkens HG, Cooper C 2002 The epidemiology of corticosteroid-induced osteoporosis: a meta-analysis. *Osteoporos Int* 13:777-787
29. Van Staa TP, Leufkens HG, Abenhaim L, Zhang B, Cooper C 2000 Use of oral corticosteroids and risk of fractures. *J Bone Miner Res* 15(6):993-1000
30. Peel NF, Moore DJ, Barrington NA, Bax DE, Eastell R 1995 Risk of vertebral fracture and relationship to bone mineral density in glucocorticoid treated rheumatoid arthritis. *Ann Rheum Dis* 54:801-806
31. Van Staa TP, Laan RF, Barton IP, Cohen S, Reid DM, Cooper C 2003 Bone density threshold and other predictors of vertebral fracture in patients receiving oral glucocorticoid therapy. *Arthritis Rheum* 48(11):3224-3229
32. Rehman Q, Lang T, Modin G, Lane NE 2002 Quantitative computed tomography of the lumbar spine, not dual X-ray absorptiometry, is an independent predictor of prevalent vertebral fractures in postmenopausal women with osteopenia receiving long-term glucocorticoid and hormone-replacement therapy. *Arthritis Rheum* 46(5):1292-1297
33. Borah B, Gross GJ, Dufresne TE, Smith TS, Cockman MD, Chmielewski PA, Lundy MW, Jartke JR, Sod EW 2001 Three-dimensional microimaging (MRuI and uCT), finite element modeling, and rapid prototyping provide unique insights into bone architecture in osteoporosis. *Anat Rec (New Anat)* 265:101-110

34. Niebur GL, Feldstein MJ, Yuen JC, Chen TJ, Keaveny TM 2000 High-resolution finite element models with tissue strength asymmetry accurately predict failure of trabecular bone. *J Biomech* 33:1575–1583
35. Derynck R, Choy L 1998 Transforming Growth Factor-Beta and its Receptors. In: Thomson A (ed.) *The Cytokine Handbook*. Academic Press, San Diego, pp 593-636.
36. Bonewald LF 1999 Regulation and regulatory activities of transforming growth factor beta. *Crit Rev Eukaryot Gene Expr* 9(1):33-44.
37. Bonewald LF, Dallas SL 1994 Role of active and latent transforming growth factor beta in bone formation. *J Cell Biochem* 55(3):350-7.
38. Centrella M, Horowitz MC, Wozney JM, McCarthy TL 1994 Transforming growth factor-beta gene family members and bone. *Endocr Rev* 15(1):27-39.
39. Derynck R, Feng XH 1997 TGF-beta receptor signaling. *Biochim Biophys Acta* 1333(2):F105-50.
40. Derynck R, Zhang Y, Feng XH 1998 Smads: transcriptional activators of TGF-beta responses. *Cell* 95(6):737-40.
41. Harris SE, Bonewald LF, Harris MA, Sabatini M, Dallas S, Feng JQ, Ghosh-Choudhury N, Wozney J, Mundy GR 1994 Effects of transforming growth factor beta on bone nodule formation and expression of bone morphogenetic protein 2, osteocalcin, osteopontin, alkaline phosphatase, and type I collagen mRNA in long-term cultures of fetal rat calvarial osteoblasts. *J Bone Miner Res* 9(6):855-63.
42. Hunter GK, Hauschka PV, Poole AR, Rosenberg LC, Goldberg HA 1996 Nucleation and inhibition of hydroxyapatite formation by mineralized tissue proteins. *Biochem J* 317 (Pt 1):59-64.
43. ten Dijke P, Hill CS 2004 New insights into TGF-beta-Smad signalling. *Trends Biochem Sci* 29(5):265-73.
44. Yu L, Hebert MC, Zhang YE 2002 TGF-beta receptor-activated p38 MAP kinase mediates Smad-independent TGF-beta responses. *Embo J* 21(14):3749-59.

UCSF LIBRARY

Chapter 2

Micro-Raman spectroscopic investigation of dental calcified tissues

Reprinted from: Karen A. Schulze, Mehdi Balooch, Guive Balooch, Grayson W. Marshall, and Sally J. Marshall. (2004) **Micro-Raman spectroscopic investigation of dental calcified tissues.** *J Biomed Mater Res A*. May 1; 69(2):286-93. With permission from Wiley.

Abstract

The purpose of this study was to determine if dental calcified junctions (DEJ/CDJ) in human teeth contain different compositional phases compared to the adjacent dental calcified tissues. Peak positions and intensities were determined from micro Raman spectra for PO_4^{3-} and the C-H modes and were compared among the mineralized tissues and their junctions. Values of width were determined from the intersections of intensity regression lines through the junctions and in the adjacent tissues. The peaks were measured in $1\mu\text{m}$ steps along a $100\mu\text{m}$ line across the junction. High resolution analysis revealed that PO_4^{3-} band peaks for dentin, the DEJ, enamel, the CDJ and cementum were at the same position (959 cm^{-1}), while for the C-H stretching mode a significant shift of 4.6 cm^{-1} was found between enamel, the DEJ and dentin. The mean width of the DEJ was $7.6 (\pm 2.8)\mu\text{m}$, using the PO_4^{3-} band, and $8.6 (\pm 3.6)\mu\text{m}$ using the C-H stretching mode. Across the DEJ, the mineral content monotonically decreased from enamel to dentin, while the organic component monotonically increased. The DEJ width was in agreement with prior nanoindentation studies. No width estimate was possible for the CDJ because the compositional differences between cementum and dentin were small.

Introduction

Dentin, enamel and cementum formation involves a remarkable orchestration of complex molecular and cellular events that culminate in uniquely structured tissues joined at distinctive interfaces. The dentino-enamel junction (DEJ) is the natural junction

that unites the dentin with the enamel in a functionally graded region.¹⁻⁴ It has been found that the DEJ is resistant to acid attacks⁵ as well as to mechanical forces such as crack propagation.^{2,3,6} The DEJ has a unique structure with at least three levels of microstructure.⁷⁻⁹ The scallops house microscallop that contain finer nano-scale structures.^{2,10} The scallops and the presence of a smooth gradient of mechanical properties at the junction are believed to contribute to an important toughening mechanism that reduces stress concentrations. This gradation of properties is initiated by a biomineralization process starting from the DEJ in both directions.^{3,8,11} The DEJ is the junction of coronal dentin and enamel and is formed by the secretion of dentin on one side and of enamel on the other side. The nature of the cemento-dentin junction (CDJ) is controversial and it is not clear, whether it is a form of dentin, cementum, or a tissue in its own right. This layer has been called “interzonal layer”,¹² “intermediate layer of cementum”¹³ and “intermediate cementum”.¹⁴ Studies on the CDJ have been mostly of histological nature. Only few physical properties of cementum have been investigated.¹⁵ From the CDJ dentin is formed internally and cementum externally. However, the structure of the CDJ remains unclear.

Several mechanical properties studies^{1,2,16,17,18} as well as conventional morphological studies^{19,20} have been conducted on the DEJ and the CDJ, but these techniques lack the ability to obtain chemically related information. Raman microspectroscopy produces the capability to characterize the spatial distributions of organic compounds and inorganic compounds with spatial resolution of about 1 μm .²¹ Previous studies have used vibrational analysis to characterize interfaces between dentin and resin or enamel and resin, to evaluate bonding to the altered dentin/enamel surface.²¹⁻

...
c
...
sc
...
c
...
S
...
CA
...
CA
...
SC
...
Y
...
C
...
TYO
...
S
...
CA
...
O
...
CA
...
SC
...
Y

²³ The enamel Raman spectrum is dominated by bands which can be attributed to the mineral apatite at 591, 961 and 1071 cm^{-1} . The dentin and cementum spectra indicate the presence of much larger proportions of organic material. The C-H stretching bands at 2940 and 2880 cm^{-1} are more intense, and amide I and III bands at 1670 and 1243 cm^{-1} have been identified. These bands, which correlate with those found in the FT Raman spectra for bone, may indicate a similar protein composition in the two materials.²⁴

The first aim of this study was to determine if the DEJ is a different phase than the adjacent substrates. Therefore the chemical composition of these substrates was analyzed using micro Raman spectroscopy. The intensity values of the spectra obtained from the inorganic component, represented by PO_4^{3-} band peaks (apatite), as well as the spectra obtained from the organic component, represented by C-H stretching mode (collagen), reveal this information. Shift analysis of the peaks in these spectra allows the chemical contents of the tissues to be differentiated. The hypothesis tested was that the DEJ and CDJ consist of phases with different composition than the adjacent tissues. The second aim was to determine the width of the DEJ using phosphate and C-H band intensity changes.

Materials and Methods

Sample preparation

Extracted sound human third molars, from subjects requiring such extractions as part of their dental treatment, were selected for this study. These procedures have been conducted according to an informed consent protocol that has been approved by the

UCSF Institutional Committee on Human Research. Three teeth were gamma radiated²⁵ and stored at 4°C in deionized water until prepared. Saggital bucco-lingual sections were prepared to obtain slabs of 1 mm thickness, containing enamel, the DEJ, dentin, the CDJ and cementum. The specimens were polished with a series of SiO₂ papers and on polishing cloths with different diamond suspensions through 0.25 μm. Ultrasonic treatments in deionized water for 60s were used between polishing stages to clean the surface and remove the remnant smear layer.

Raman microspectroscopy

The Raman spectra were recorded on an HR 800 Raman spectrophotometer (Jobin Yvon, Horiba, France) using monochromatic radiation emitted by a He-Ne laser (632.8 nm), operating at 20 mW of power, before entrance optics. Laser scanning imaging resolution was about 0.5 μm. All measurements were made systematically under the same conditions, utilizing ~1 μm depth of laser penetration ('hole adjustment setting'). A computer-controlled translation stage was used to move the specimen under the laser beam in 1 μm increments.

The spectral processing of the data included the subtraction of the luminescence background from the total spectra and deconvoluting the peaks by curve fitting of the Raman peaks.

Compositional analysis of mineralized dental hard tissue

For the high-resolution analysis three samples were selected to obtain spectra with a 100x microscope objective with a small confocal hole (to increase spatial resolution) and slit (to improve spectral resolution). The locations were in dentin, 100 μm from the DEJ; at the DEJ; in enamel, 100 μm from the DEJ; at the CDJ; and in cementum, 50 μm from the CDJ. The latter measurement was only 50 μm from the CDJ because the cementum is quite thin in some teeth. Figure 1 is a schematic showing a tooth section and locations where Raman measurements were made on each tooth. All spectra were obtained with an acquisition time of 600 sec for the phosphate band at $\sim 960\text{ cm}^{-1}$ and for the C-H stretching mode at $\sim 2937\text{ cm}^{-1}$. The C-H stretching mode was chosen as an indicator for organic content because the luminescence at the 2900 cm^{-1} band is much smaller than at other organic band locations (1660, 1442 and 1200 cm^{-1}). The background could be reduced more accurately due to better signal to noise ratio, thus providing the best results. For the purpose of presenting a clear spectrum of the C-H stretching mode for enamel an acquisition time of 72 h was used (Figure 2). The software Labspec V4 (Jobin Yvon, Horiba, France) was used for peak fitting of the acquired spectra. Peak analysis included: a) maximum peak location; b) peak intensity; c) ratio of phosphate band/C-H stretching mode and d) ratio of phosphate /carbonate band. A grating groove density of 1800 grooves/mm instead of 600 grooves/mm was used, to obtain high resolution spectra for possible shifts due to different organic material. This was especially necessary for enamel, where the concentration of organic material is very small and different proteins than those in dentin can be identified. This automatically narrows the scanning interval down to 1108 to 811 cm^{-1} for the phosphate band and to 3037 to 2842 cm^{-1} for the C-H stretching mode. The scanning interval of the phosphate band includes

the carbonate peak at 1070 cm^{-1} . A ratio of the phosphate/carbonate peaks was analyzed based on the relative integrated intensities.

Determination of the width of the DEJ

For the determination of the width of the DEJ three different samples were placed at the focus of a 50x microscope objective and spectra were acquired at $1\text{ }\mu\text{m}$ intervals across the DEJ. A $100\text{ }\mu\text{m}$ line perpendicular to the interface was scanned with an acquisition time of 30 sec for each measurement. The sample moved in $1\text{ }\mu\text{m}$ intervals across the interface while the laser remained stationary. Lines at three different positions, as shown in Figure 1, were run per sample. Spectra were acquired for the phosphate band in an interval of $1700\text{ to }600\text{ cm}^{-1}$ and for the C-H stretching mode in an interval of $3300\text{ to }2400\text{ cm}^{-1}$. The computer program automatically selected these intervals because 600 grooves/mm were used since higher resolution was not needed, and so a broader range could be sampled. The intensity of the phosphate peak at 960 cm^{-1} was obtained from each measurement. The measurements were then repeated to collect the intensity values for the C-H stretching mode at the position using the band from $3000\text{ to }2850\text{ cm}^{-1}$, which represents the three peaks of the C-H stretching mode. There was a total of eighteen lines (nine for PO_4^{3-} and nine for C-H measurements). On each sample three lines for PO_4^{3-} and three lines of C-H at different locations were scanned. Each line was $100\text{ }\mu\text{m}$ long and the data were collected in $1\text{ }\mu\text{m}$ steps. Three samples were done this way resulting in a total of 1800 measurements in the area of the DEJ. The intensity values were plotted as graphs (see Figure 3). To evaluate the width of the DEJ, linear regression lines were estimated from 1) the data in dentin, 2) the data in enamel and 3) from the slope between

dentin and enamel. The intersections of the three regression lines were used to obtain estimates of the DEJ width for each data set, one using the PO_4^{3-} peaks and one using the C-H stretching mode.

In addition to the analysis of the 100 μm lines in different areas of the teeth, the DEJ width was determined from one area of 100 x 100 μm by scanning in 1 μm steps, to see the variation in a small region. A distinct width was calculated for each line of that region, i.e. a total of 100 values. The scan direction was not perpendicular to the DEJ thus the measured widths needed to be multiplied by cosine of the angle between the scan direction and the perpendicular to the DEJ to correct this geometry.

A distribution curve of the estimated widths was plotted for the PO_4^{3-} peaks (total: 100 values) as well as with the C-H stretching mode (total: 100 values).

Statistical methods

A one-way ANOVA (SAS statistical software, version 7, SAS Institute Inc., Cary, NC, USA) and Student-Newman-Keuls-test were used to determine statistical significance of compositional differences and confirm peak shifts of the phosphate band at $\sim 960\text{ cm}^{-1}$ and the C-H stretching mode at $\sim 2937\text{ cm}^{-1}$. A student's t-test was used to determine any statistical differences between the width of the DEJ using the phosphate band intensity changes and C-H stretching mode changes. Intra-tooth differences in the width of the DEJ in buccal, lingual and occlusal regions were evaluated using one-way ANOVA and Student-Newman-Keuls tests.

Results

Compositional analysis of mineralized dental hard tissue

Table 1 includes high resolution peak analysis for each of the tissue substrates and junctions: dentin, DEJ, enamel, CDJ and cementum. The peaks for the phosphate bands were located for all substrates between 959.5 and 960.2 cm^{-1} . The mean was 959.8 cm^{-1} . No significant differences could be found among the tissues or junctions ($p = 0.47$). The C-H peaks for dentin, CDJ and cementum were located between 2937.9 and 2938.6 cm^{-1} . A shift of the C-H stretching mode was clearly seen (Figure 2) for the enamel and the DEJ compared to the dentin C-H stretching mode. The peaks were located at 2934.3 and 2935.7 cm^{-1} and 2938.6 cm^{-1} , respectively. Statistically significant differences at the $p < 0.05$ confidence level among all mineralized tissues with respect the C-H peak location were found, except between cementum and the CDJ ($p = 0.093$) and between cementum and dentin ($p = 0.099$).

The phosphate/C-H ratio clearly showed that enamel had a different average composition than the adjacent hard tissues. The cementum had the lowest (2.8) and enamel the highest ratio (94.2). The phosphate/C-H intensity ratio for dentin was approximately 10 % that of enamel. Comparing the phosphate with the carbonate intensities the ratios were similar for dentin, the CDJ and cementum with 3.7 4.5 and 4.7, while for the DEJ and enamel it resulted in 17.6 and 18.1, respectively (Table 1). Figure 2 shows the C-H stretching for enamel and dentin between 3100 and 2800 cm^{-1} . The spectra have two different scales because of different acquisition times. The enamel spectrum shows an additional fourth peak at 2850 cm^{-1} .

Determination of the width of the DEJ

Using the intensity of the phosphate peaks at 959 cm^{-1} , lines across the DEJ yielded a mean width of $7.6 (\pm 2.8)\ \mu\text{m}$ for this gradient zone. The intensities of the C-H stretching mode and the phosphate band are plotted in Figure 3 for a representative $100\ \mu\text{m}$ line across the DEJ. When using the gradient measurement method for the C-H stretching mode a somewhat wider DEJ was determined, with a mean width of $8.6 (\pm 3.6)\ \mu\text{m}$. A t-test showed no significant difference between the two estimates of the width of the DEJ ($p = 0.56$). A one-way ANOVA showed that there were no significant differences in DEJ width at buccal, lingual or occlusal locations of the tooth ($p = 0.18$). Figure 4 shows three-dimensional images of the DEJ and CDJ locations with the intensity of phosphate band peaks (4a and 4c) or with the C-H stretching mode peaks (4b and 4d) in $1\ \mu\text{m}$ steps and an acquisition time of 30 sec. The DEJ images show strong intensity differences when scanned with the phosphate band (4a) or with the C-H band (4b). For the area displayed in Figures 4a and 4b width values were determined for 100 lines in the $100 \times 100\ \mu\text{m}$ area, resulting in a distribution curve for the width of the DEJ, as shown in Figure 5. In this graph widths of 7 and $8\ \mu\text{m}$ were most abundant followed by widths of 4 and $6\ \mu\text{m}$. The range of values was large, from 1 – $10\ \mu\text{m}$. However, the median values of 6 and $7\ \mu\text{m}$ confirmed the findings estimated with single lines in different regions of the tooth.

The images in 4c and 4d suggest that there is no clear distinguishable zone that can be identified as the CDJ. There was no gradient zone as seen between dentin and enamel. Therefore the width could not be determined using this gradient zone method. However, a highly fluorescent zone of about 20 to $30\ \mu\text{m}$ was detected at this junction.

Figure 6 displays a two dimensional total emission image with a resolution of $1 \times 1 \mu\text{m}$ and an acquisition time of 30 sec per measurement. After subtracting the fluorescence from the image, no difference could be seen between dentin, CDJ and cementum as demonstrated in Figure 4d.

A shallow valley was present in the intensity plot of the C-H band at each side of the CDJ, as shown in Figure 7 and in the three-dimensional image Figure 4d.

Discussion

Raman spectroscopy is an advanced, fast analytical technique to determine the structure and chemical composition of materials. It provides chemical information based on molecular vibrations of the molecules in the sample. In this study the spectra from human dental hard tissues were analyzed in two specific wave number locations, the phosphate stretching band and the C-H stretching mode.

Apatite mineral exhibits characteristic spectra in the frequency range from 1700 to 600 cm^{-1} .²¹ The mineral portion of the Raman spectra from all substrates exhibited the characteristics of carbonated hydroxyapatite (HAP) with stronger peaks for the phosphate stretching mode PO_4^{3-} (959 cm^{-1}) than for the carbonate mode CO_3^{2-} at 1072 cm^{-1} . The envelope of the C-H stretching mode (3300 to 2400 cm^{-1}) was used in this study because it had the potential to detect differences in non-collagenous proteins as well as collagen. It is less often investigated as a signature of the organic content in dental hard tissues but has been studied frequently in bone deproteinization analysis, as discussed by Pelletier,²¹ and Termine, *et al.*²⁶

The gradient zone between dentin and cementum was difficult to measure because the zone exhibited fluorescence. This may be due to impurities incorporated during sample preparation or to the luminescent nature of proteins which are more abundant in this area. Further studies need to address this question.

The gradient zone between enamel and dentin seen with the C-H stretching mode is due to the very low organic content (~4%) in enamel. No collagen type I is present, but proteins of this matrix include the tyrosine-rich amelogenin polypeptide and other “non-amelogenin” proteins, such as enamelin, tuftelin, ameloblastin, serum albumin and proteinases, although the origin of the serum proteins is thought to lie in post-extraction contamination.^{10, 27} The difference between collagen type I in dentin and the organic component of enamel was clear in the shift of the C-H stretching mode with long acquisition time. The enamel spectrum in Figure 2 was obtained with 72 h acquisition time to diminish the noise, while the dentin spectrum required only 600 sec. This adjustment was made to better visualize the differences in the two C-H stretching mode locations. The C-H stretching mode usually absorbs near 2890 cm^{-1} , but this band is found in a broader region, $3000\text{ to }2850\text{ cm}^{-1}$, when the C-H is adjacent to a non carbon atom.²¹ It is likely that apatite forming molecules surround the C-H, causing the entire band to shift. Visual examination did not reveal any apparent change in the enamel but prolonged laser exposure may have caused the peak shift.^{28,29} Further studies are necessary to eliminate these possibilities.

The present study found pronounced changes in peaks from mineral and organic components, which yielded information about the connecting zones, such as the DEJ. However, this system has limitations and could not identify a well-differentiated junction

between dentin and cementum, since the mineral and organic contents are very similar. The long acquisition times per measurement point yielded a high resolution analysis, shown in Table 1, with precise maximum peak locations with low standard deviations. The statistically significant differences, found with respect to the peak locations from the C-H mode, between the DEJ, dentin and enamel may support the hypothesis that the DEJ has a different chemical composition than the adjacent tissues, dentin and enamel. However, these significant peak shifts might be due to the blending of different organic compounds or due to the differences in composition between the organic contents in dentin³⁰ and non-collagen type proteins in enamel.³¹ This is likely since the C-H peak from the DEJ was 2935.7 cm^{-1} , between the peaks for dentin and enamel. Whether it is a combination of organic and non-organic compounds or a new material remains unclear. Therefore, the hypothesis that the DEJ is a separate entity could not be clearly established and it is assumed to be a gradient zone.

No peak shifts between the CDJ and cementum and between cementum and dentin could be seen using the C-H mode. This indicates that the latter materials are composed of similar structures and the hypothesis that the junction has similar composition to cementum and dentin can be verified. Analyzing the peak locations with respect to the PO_4^{3-} band, all substrates showed the same peak location at 959 cm^{-1} . The Raman intensities for both, the PO_4^{3-} band and the C-H stretching mode from the DEJ exhibited linear gradient zones, as presented in Figure 3. This suggests that the concentration of organic and inorganic materials is monotonically changing. The phosphate/C-H ratios demonstrate a ratio difference from 2.8 for cementum to 94.2 for enamel. The phosphate/carbonate ratios varied from 7.1 for dentin to 19.6 for enamel.

The value of 18.7 for the DEJ was closer to that of enamel, in contrast to the phosphate/C-H ratios, where the DEJ was similar to dentin. (Table 1)

The width of the DEJ has been evaluated based on the morphological structure⁷ as well as mechanical properties. The DEJ functional width was reported as being 27 - 100 μm wide⁴ using Vickers microhardness measurements. Nanomechanical techniques have yielded a significantly narrower DEJ width. Fong *et al.*³ reported a DEJ width of 15 to 25 μm , while Marshall *et al.*² found 10 – 13 μm , both using nanoindentation. A nanoscratching method using the atomic force microscope (AFM) measured by Habelitz *et al.*¹ revealed a very narrow transitional zone of 1-3 μm , established with friction properties. The latter can provide improved estimates of mechanical property changes because it continuously measures the friction coefficient. Nano- and microindentations require spacing to avoid interaction of the plastic zones and the contact stress fields. The present study measured the chemical composition in 1 μm steps and with a laser penetration of about 1 μm in depth in the sample. Thus the micro Raman data suggests that the DEJ contains no unique chemical component and its characteristics can be explained as a mixture of enamel and dentin. The results in Figure 5 demonstrate that the calculation of the width of the DEJ gives almost the same answer when using the C-H mode or the phosphate band. The present study showed that the micro Raman technique can be used to discriminate between different proteins as in collagen type I in dentin³⁰ and amelogenin or other proteins in enamel.³¹ The specific peak position for collagen type I in dentin was 2938.6 cm^{-1} and for the protein composition in enamel was 2934.3 cm^{-1} .

In conclusion, mineralized tissues in the tooth were compared using Raman spectroscopy, showing the DEJ and the CDJ as zones of chemical transition rather than separate phases. The DEJ width yielded similar results to those determined using nanomechanical methods. Also a peak shift of 4.6 cm^{-1} was found when comparing organic components of dentin with enamel, revealing that collagen type I molecules in dentin have a different maximum peak position for the C-H stretching mode than the non-collagen proteins in enamel.

Acknowledgement

This study was supported by NIH/NIDCR Grants R01 DE 13029 and P01DE09859.

UCSF LIBRARY

References

1. Habelitz S, Marshall SJ, Marshall GW, Jr., Balooch M. The functional width of the dentino-enamel junction determined by AFM- based nanoscratching. *J Struct Biol* 2001; 135:294-301.
2. Marshall GW, Jr., Balooch M, Gallagher RR, Gansky SA, Marshall SJ. Mechanical properties of the dentinoenamel junction: AFM studies of nanohardness, elastic modulus, and fracture. *J Biomed Mater Res* 2001; 54:87-95.
3. Fong H, Sarikaya M, White SN, Snead ML. Nano-mechanical properties profiles across dentin-enamel junction of human incisor teeth. *Mat Sci Engi C, Biomim Supramol Sys* 2000; C7:119-128.
4. White SN, Paine ML, Luo W, Sarikaya M, Fong H, Yu ZK, Li ZC, Snead ML. The dentino-enamel junction is a broad transitional zone uniting dissimilar bioceramic composites. *J Am Ceram Soc* 2000; 83:238-240.
5. Tramini P, Pelissier B, Valcarcel J, Bonnet B, Maury L. A Raman spectroscopic investigation of dentin and enamel structures modified by lactic acid. *Caries Res* 2000; 34:233-240.
6. Lin CP, Douglas WH. Structure-property relations and crack resistance at the bovine dentin-enamel junction. *J Dent Res* 1994; 73:1072-1078.
7. Arsenault AL, Robinson BW. The dentino-enamel junction - a structural and microanalytical study of early mineralization. *Calcified Tissue Int* 1989; 45:111-121.
8. Brännström M. *Dentin and pulp in restorative dentistry*, London: Wolfe Medical Publications; 1982:125.
9. Scott JH, Symons NBB. *Introduction to dental anatomy*. 6th ed, Edinburgh,: Livingstone; 1971:448.
10. Marshall SJ, Balooch M, Habelitz S, Balooch G, Gallagher R, Marshall GW. The dentin-enamel junction-a natural, multilevel interface. *J Eur Ceram Soc* 2003; 23:2897-2904.
11. Ten Cate AR. *Oral histology: development, structure, and function*. 5th ed, St. Louis: Mosby; 1998:497.
12. Bodecker CFW. The distribution of living matter in human dentin, cement and enamel. *Dent Cosmos* 1957; 20:582-590.
13. Benz L. Befunde an der Dentinzement Grenze. *Z Stomat* 1927; 5:877-896.
14. Blackwood HJJ. Intermediate cementum. *Brit Dent J* 1957; 102:345-350.
15. Brear K, Currey JD, Pond CM, Ramsay MA. The mechanical properties of the dentine and cement of the tusk of the narwhal *Monodon monoceros* compared with those of other mineralized tissues. *Arch Oral Biol* 1990; 35:615-621.
16. Habelitz S, Marshall SJ, Marshall GW, Balooch M. Mechanical properties of human dental enamel on the nanometre scale. *Arch Oral Biol* 2001; 46:173-183.
17. Kinney JH, Balooch M, Marshall GW, Marshall SJ. A micromechanics model of the elastic properties of human dentine. *Arch Oral Biol* 1999; 44:813-822.
18. Balooch M, Wu-Magidi IC, Balazs A, Lundkvist AS, Marshall SJ, Marshall GW, Siekhaus WJ, Kinney JH. Viscoelastic properties of demineralized human dentin measured in water with atomic force microscope (AFM)-based indentation. *J Biomed Mater Res* 1998; 40:539-44.

19. Yamamoto T, Domon T, Takahashi S, Islam MN, Suzuki R. The fibrillar structure of the cemento-dentinal junction in different kinds of human teeth. *J Periodontal Res* 2001; 36:317-321.
20. el Mostehy MR, Stallard RE. Intermediate cementum. *J Periodontal Res* 1968; 3:24-29.
21. Pelletier MJ. Analytical applications of Raman spectroscopy, Vol, Oxford; Malden, MA: Blackwell Science; 1999:478.
22. Suzuki M, Kato H, Wakumoto S. Vibrational Analysis by Raman Spectroscopy of the Interface between Dental Adhesive Resin and Dentin. *J Dent Res* 1991; 70:1092-1097.
23. Lemor RM, Kruger MB, Wieliczka DM, Swafford JR, Spencer P. Spectroscopic and morphologic characterization of the dentin/adhesive interface. *J Biomedical Optics* 1999; 4:22-27.
24. Hendra P, Jones C, Warnes G. Fourier transform Raman spectroscopy: instrumentation and chemical applications. Ellis Horwood series in analytical chemistry, New York: Ellis Horwood; 1991:311.
25. White JM, Goodis HE, Marshall SJ, Marshall GW. Sterilization of teeth by gamma radiation. *J Dent Res* 1994; 73:1560-1567.
26. Termine JD, Eanes ED, Greenfield DJ, Nysten MU. Hydrazine-deproteinized bone mineral. *Calc Tiss Res* 1973; 12:73-90.
27. Chadwick D, Cardew G. Dental enamel. Chiba Foundation symposium; Chichester; New York: Wiley; 1997:284.
28. Wiekuczja DM, Spencer P, Kruger MB. Raman Mapping of the Dentin/Adhesive Interface. *Appl Spectr* 1996; 50:1500-1504.
29. Wieliczka DM, Kruger MB, Spencer P. Raman Imaging of Dental Adhesive Diffusion. *Appl Spect* 1997; 51:1593-96.
30. Butler WT, Ritchie H. The Nature and Functional Significance of Dentin Extracellular Matrix Proteins. *Int J Dev Biol* 1995; 39:169-179.
31. Robinson C, Brookes SJ, Shore RC, Kirkham J. The developing enamel matrix:nature and function. *Eur J Oral Sci* 1998; 106:282-291.

UCSF LIBRARY

Tables

Table 1. Shift analysis of phosphate band versus C-H stretching mode, phosphate/C-H stretching mode ratios, and phosphate/carbonate ratios

	Maximum Peak Location (cm ⁻¹), Phosphate	Maximum Peak Location (cm ⁻¹), C-H	Intensity Ratio PO ₄ ³⁻ /C-H	Intensity Ratio PO ₄ ³⁻ /CO ₃ ²⁻
Dentin	959.9 +/- 0.2	2938.9 +/- 0.5	9.9	7.1
DEJ	959.9 +/- 0.4	2935.7 +/- 0.6	10.5	18.7
Enamel	959.6 +/- 0.2	2934.3 +/- 0.3	94.2	19.6
CDJ	959.8 +/- 0.1	2937.4 +/- 0.4	3.3	6.8
Cementum	959.8 +/- 0.6	2938.2 +/- 0.4	2.8	6.5

UCST LIBRARY

Figures and Captions

Figure 1

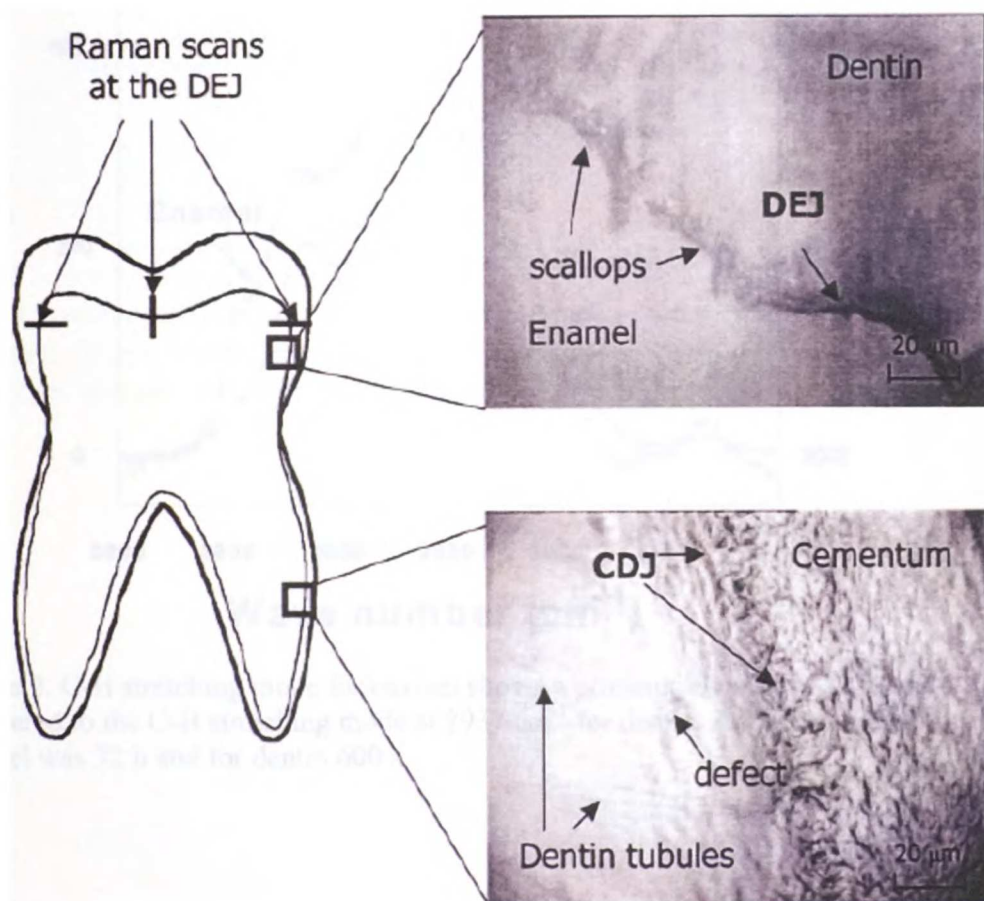


Figure 1. Schematic illustration of the tooth specimen showing areas where Raman spectra were acquired in a perpendicular line across the DEJ and CDJ. The insets show microscopic photos at 50X the DEJ and CDJ.

Figure 2

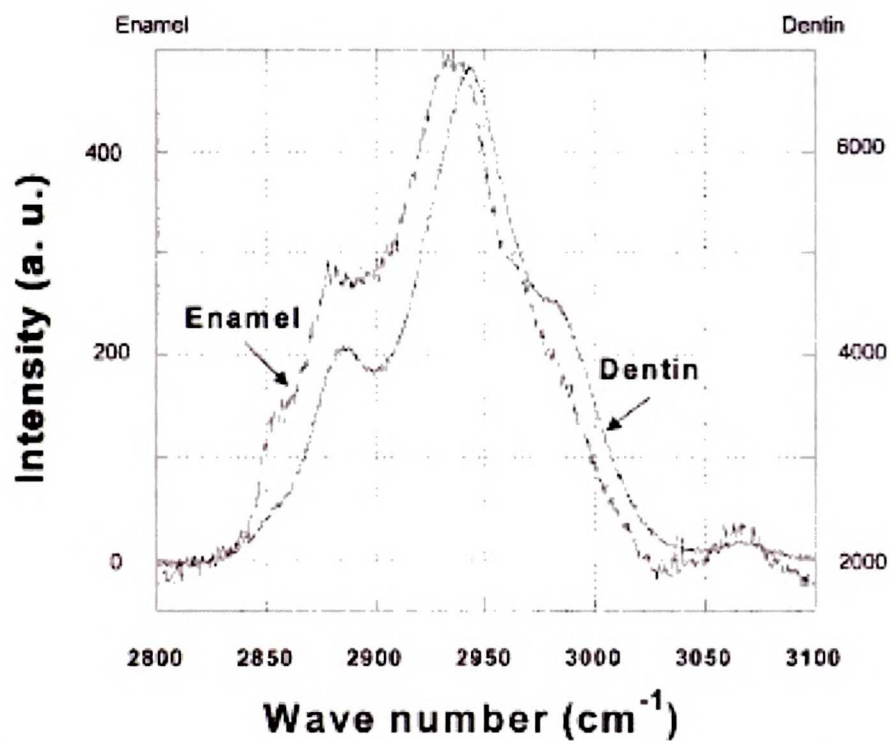


Figure 2. C-H stretching mode for enamel shows a pronounced shift to 2934 cm^{-1} compared to the C-H stretching mode at 2937 cm^{-1} for dentin. Acquisition time for enamel was 72 h and for dentin 600 s.

Figure 3

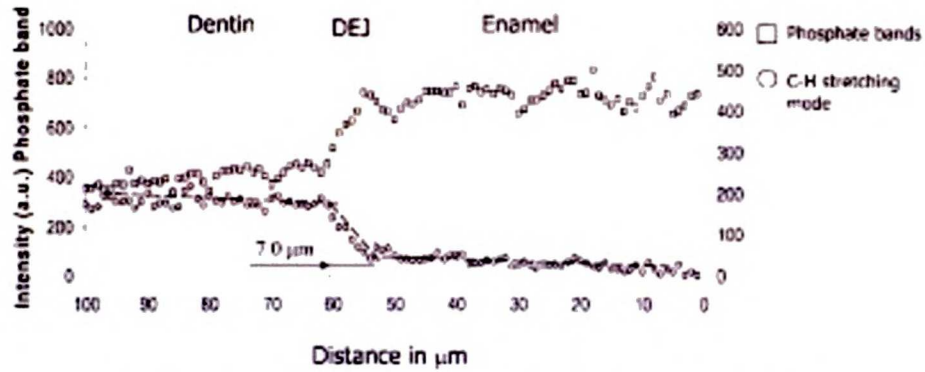


Figure 3. Analysis of a representative course of Raman spectra obtained by scanning perpendicularly across the DEJ in 1 μm steps with an acquisition time of 30 s for a total length of 100 μm . The width of the sloped region relates to the width of the DEJ. Phosphate intensity on left axis, C-H intensity on right axis.

UCSF LIBRARY

Figure 4

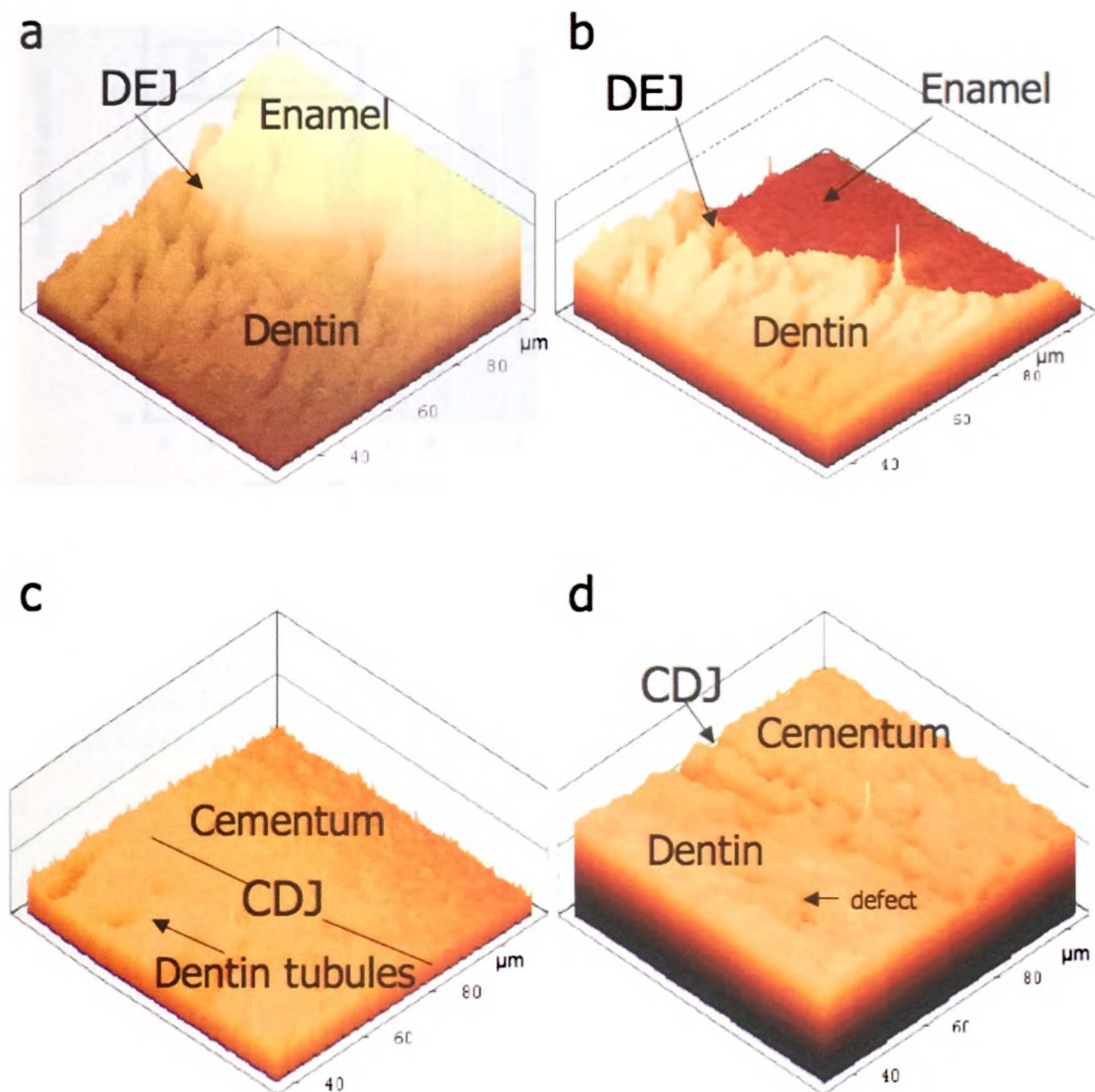


Figure 4. 3D Raman spectroscopic analysis of the areas shown in Figure 1. (a) Scanning DEJ area with respect to phosphate band. (b) Scanning DEJ area with respect to C-H stretching mode. (c) Scanning CDJ area with respect to phosphate band. (d) Scanning CDJ area with respect to C-H stretching mode (defect in collagen is visible and congruent with defect in Fig.1 CDJ area).

UIC LIBRARY

Figure 5

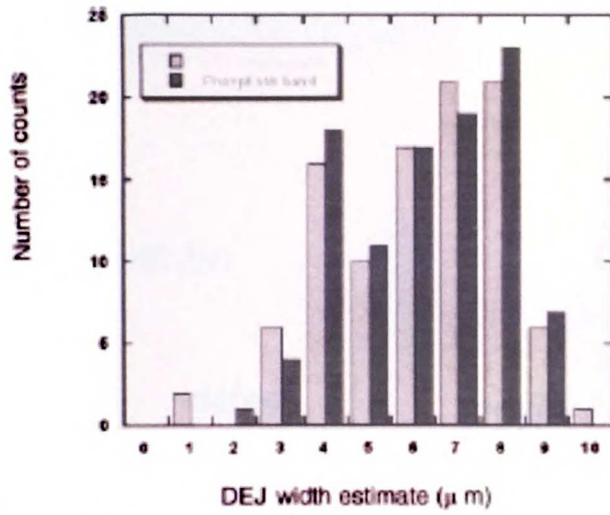


Figure 5. Distribution curve for DEJ width determined with phosphate band peaks and C-H stretching mode peaks.

UCSF LIBRARY

Figure 6

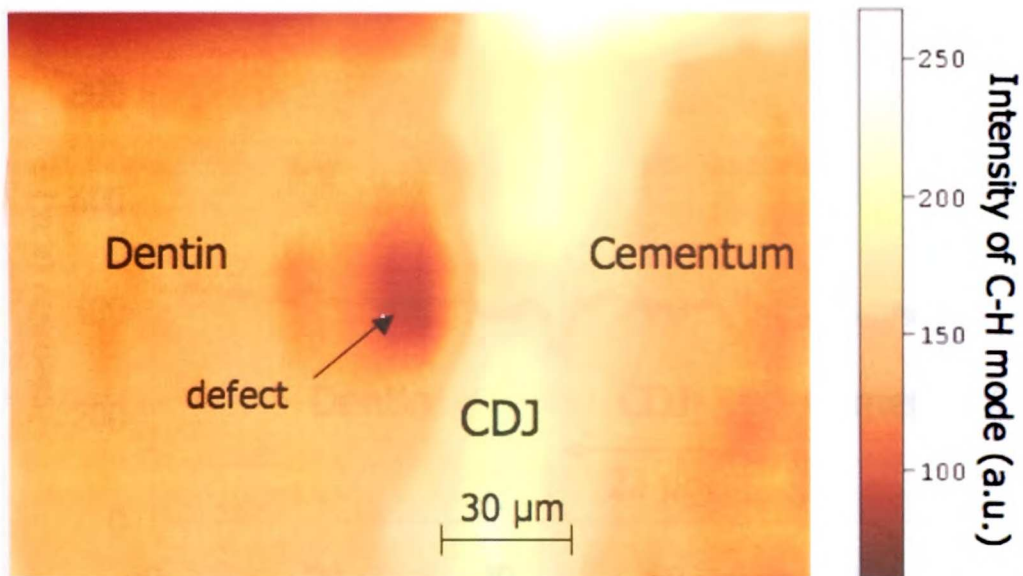


Figure 6. 2D Raman image of the CDJ area. The scanned area shows total emission of the C-H stretching mode only. The image shows a highly fluorescent band of about 30 μm highlighting the CDJ.

UCSF LIBRARY

Figure 7

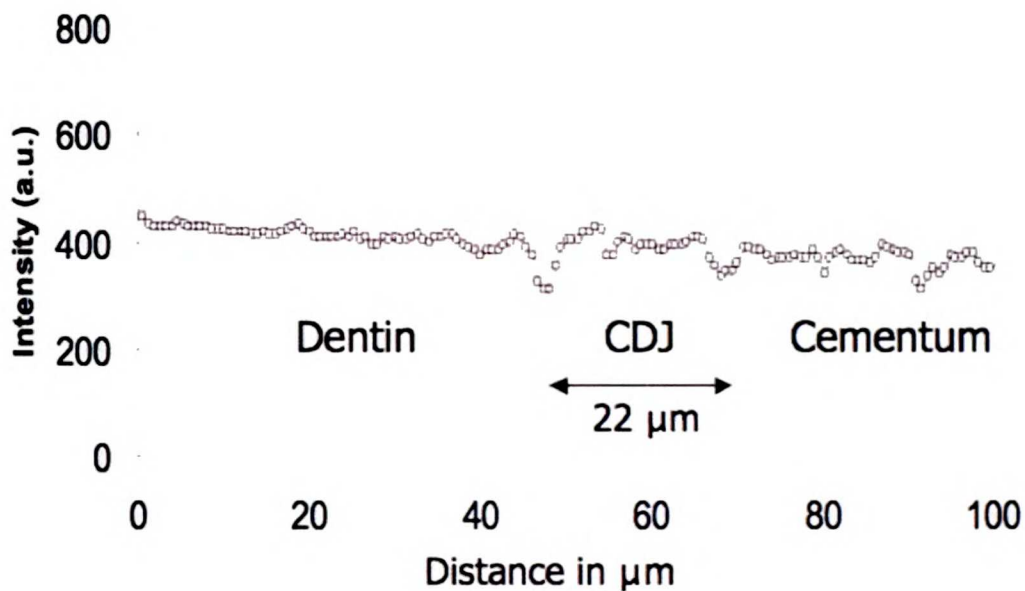


Figure 7. Scanned line of 100 μm across the CDJ using Raman spectroscopy at the C-H stretching mode including the 2882-, 2934-, and 2989- cm^{-1} bands. A shallow valley adjacent to the CDJ marks the CDJ band. This observation was made on several CDJ samples. Figure 3(d) shows these valleys in a 3D image.

UCSF LIBRARY

Chapter 3

Evaluation of a new modulus mapping technique to investigate microstructural features of human teeth

Reprinted from: Balooch, G., Marshall, G.W., Marshall, S.J., Warren, O.L., Asif, S.A., Balooch, M. (2005) **Evaluation of a new modulus mapping technique to investigate microstructural features of human teeth** *J Biomech.* Aug; 37(8):1223-32. With permission from Elsevier.

between 17-23 GPa with a mean value of 21 GPa. The range of storage modulus for enamel near the DEJ was between 51-74 GPa with a mean value of 63 GPa.

Introduction

The dentino-enamel (DEJ) and peritubular-intertubular junctions (PIJ) are natural regions that combine hard and brittle tissues with relatively soft and ductile tissues in the tooth. The locations of these features are shown schematically in Figure 1 and the microstructures of enamel and dentin have been described recently (Habelitz et al, 2001; Marshall et al, 1997 for review). The junctions may play important roles in preventing crack propagation across the boundary between the two different phases and thus, may serve as useful biomimetic models for joining mechanically dissimilar biomaterials to restore form and function (Fong et al., 2000; Marshall et al., 2001).

The structure of the DEJ is described in recent literature as having 25 to 100 μm scallops shaped with convexities directed toward dentin. Each scallop includes finer structures down to nanometer-scale features. In addition to these topographic features that enhance the surface area of junctions, gradients in phase are suggested by a precise control of protein expression and biomineralization near the junction. These gradients in phase changes result in monotonic variations in mechanical properties (Fong et al., 2000; White et al., 2000).

In recent years, the nanomechanical properties (e.g. hardness and elastic modulus) of dentin and enamel have been determined using various indentation methods (Pethica et al., 1983; Kinney et al., 1996a; White et al., 2000 Marshall et al., 2001; Habelitz et al., 2001). These methods require numerous indentations with a step size of at least 1-2 μm

to avoid the effect of overlapping or interaction of adjacent indentations. These large step sizes have limited the effectiveness of measuring relatively small transition zones, such as the DEJ or PIJ. As a result, estimates of the functional width of such interfaces appear to depend on probe size and load (Habelitz et al., 2001). Using the AFM-based nanoscratching technique, we recently determined the functional width of the DEJ as $2.0 \pm 1.1 \mu\text{m}$ (Habelitz et al., 2001); this is lower than the previous value obtained by discrete nanoindentation techniques in our laboratory (Marshall et al., 2001). However, the nanoscratch technique does not provide quantitative variation of mechanical properties. As a result, obtaining reliable DEJ width and its properties has been a daunting task due to required numerous and tedious measurements.

Much less information has been reported in the literature related to PIJ width and its local property variations. Earlier, by modulation of conventional AFM tips in contact mode, we were able to detect phase shifts that were sensitive to the stiffness of the specimen's interface. We used this modified AFM to provide qualitative imaging of the PIJ (Kinney et al., 1996a). However, the difficulty with quantification of this method has limited its applications.

In this study, the force modulation technique was used to quantitatively map dynamic nanomechanical properties of the DEJ and PIJ. In addition, the local variation of elastic modulus within the intertubular dentin and enamel also are reported.

Materials and methods

Sample Preparation

Three extracted non-carious human third molars from subjects requiring such extractions as part of dental treatment were used. These procedures were conducted according to an informed consent protocol that has been approved by the UCSF Institutional Committee on Human Research. Two sections of each of the 3 teeth were obtained (one for PIJ analysis and one for DEJ analysis) to measure mechanical properties. Sections were prepared to obtain 1 mm thick slabs containing enamel, the DEJ, and intertubular and peritubular dentin. All specimens were sectioned occlusally and the central portion was used for experimentation. The specimens were polished initially with a series of SiC papers and then on polishing cloths with different diamond suspensions down to 0.25 μm . Between each polishing stage, ultrasonic treatments in deionized water were used for time periods of 60 seconds. All specimens were placed in Hank's balanced salt solution (to avoid surface demineralization, Habelitz et al, 2002, J Biomech) and AFM imaging and dynamic stiffness mapping measurements were all conducted under dry conditions.

Modulus Mapping Technique

Quantitative modulus maps in the form of SPM (Scanning Probe Microscopy) images were acquired using the direct force modulation (nanoDMA[®]) operating mode of a TriboScope nanoindenter (Hysitron, Minneapolis, MN) mounted on a Multimode AFM controlled by NanoScope IIIa electronics (Digital Instruments, Santa Barbara, CA). Scanning Probe Microscopy is a general term for various probes that are used for imaging and measuring surfaces on a fine scale (such as AFM). The commercial implementation of quantitative modulus mapping closely followed the work of Asif et al. (1999, 2001),

and a schematic representation of the instrument configuration is shown in Fig. 2. More specifically, the electrostatic force acting on the spring-suspended center plate of the force-displacement transducer of the nanoindenter was sinusoidally modulated at 200Hz while contact mode imaging was conducted. A cube-corner diamond tip was attached to this transducer. The amplitude and the phase of the resulting transducer displacement signal were measured with a dual-channel lock-in amplifier, and this information used to determine the local indentation moduli of the sample at each pixel of the imaging process. The modulus mapping technique was calibrated using a standard quartz sample with 69.7 GPa elastic modulus. The tip contact radius is determined by calibration on a quartz standard. When the tip is examined by SEM, the resulting tip radius is in good agreement with this calibration radius

For small transducer displacements, the electrostatic force (F_c) acting on the center plate is adequately described in detail by Asif et al. (1999, 2001) as

$$F_c = K_o V^2 \quad (1)$$

where K_o is a calibrated proportionality constant and V is the applied voltage. This parabolic relationship leads to

$$F_c(t) = K_o[(V_{dc}^2 + \frac{1}{2}V_{ac}^2) + 2V_{dc}V_{ac}\sin(\omega t) - \frac{1}{2}V_{ac}^2\cos(2\omega t)] \quad (2)$$

where the applied voltage takes the form

$$V(t) = V_{dc} + V_{ac}\sin(\omega t) \quad (3)$$

and ω is the angular frequency.

The mode of direct force modulation implies a parallel loading configuration, and can be modeled as force applied to a mass that is attached to two otherwise fixed Voigt elements as long as machine compliance can be ignored. One Voigt element represents

stiffness and damping of the transducer and the other represents the same quantities for the contact. The relevant equation of motion is

$$F_c(t) = F_o \sin(\omega t) = m(dz^2/dt^2) + \beta(dz/dt) + kz \quad (4)$$

where F_o is the amplitude of the applied sinusoidal force, m is the moving mass of the transducer, $\beta = \beta_t + \beta_c$ is the combined damping coefficient of transducer and contact, $k = k_t + k_c$ is the combined stiffness of transducer and contact, z is the resulting sinusoidal displacement, and t is time. The solution to this differential equation is well known as

$$z = z_o \sin(\omega t + \varphi) \quad (5)$$

where the displacement amplitude, z_o , is given by the dynamic compliance function

$$z_o/F_o = 1/[(k - m\omega^2)^2 + (\beta\omega)^2]^{1/2} \quad (6)$$

and the phase φ of the displacement is dictated by

$$\tan(\varphi) = -\beta\omega/(k - m\omega^2) \quad (7)$$

We adhere to the convention that $\sin(\varphi)$ is negative for the lagging phase; therefore, φ asymptotically approaches $-\pi$ as ω sweeps to infinity.

Determination of m , β and k_t is accomplished by non-linear curve fitting of the dynamic compliance vs. frequency trace obtained in air. The best-fit solution corresponds to $m = 244$ mg, $\beta_t = 0.0297$ kg/s, and $k_t = 171$ N/m for the transducer-tip combination used in this study. These dynamic calibration constants are consistent with a displacement resonance centered at 132 Hz and a quality factor of 6.7

When operating in the mode of direct force modulation imaging, the nominal contact force is determined solely by the transducer spring deflection and is maintained at constant value between 1-3 μ N by the imaging feedback controller. The amplitude of the

modulated electrostatic force is set to 0.5-2.0 μN , which is large enough to maintain good signal-to-noise ratio for all material phases of the sample but sufficiently small to prevent intermittent contact. Nominal contact force, displacement amplitude, displacement phase, and topography are signals available for recording at each of the 256 x 256 pixels of the imaging process. The AFM instrument used in this study supports simultaneous acquisition of three signal channels; therefore, precise spatial correlation is not possible for all available signals. We chose to collect the first three channels listed at the same time and measure topography separately.

The storage and loss components of the complex contact stiffness were extracted from the spatially correlated set of amplitude and phase images to generate quantitative stiffness maps.

$$K' = k_c \quad (8)$$

$$K'' = \beta_c \omega \quad (9)$$

Converting this data to quantitative modulus maps required knowledge of the contact radius at each pixel. We assumed the nominal contact force was sufficiently low to justify the use of Hertzian theory (for contacts involving only the rounded apex of the tip). Rearrangement of the familiar equations of Hertzian theory yields the following relationship for the contact radius:

$$a = (3FR/2K')^{1/2} \quad (10)$$

where F corresponds to the nominal contact force, and R is the tip radius, which is determined to be 150 nm by standard nanoindentation protocol. The local storage modulus then can be formulated as

$$E' = \frac{1}{2}K'/a \quad (11)$$

and the loss component as

$$E'' = \frac{1}{2}K''/a \quad (12)$$

This method of accounting for the contact radius does not require knowledge of tip penetration, and thus is immune from thermal drift over the 10 minutes required to collect each set of images.

Results

Figure 3a shows a typical topographic image of discrete indentations and their calculated values of elastic modulus and hardness across the DEJ (Figure 3b) using a conventional indentation/AFM technique employed in our laboratory for many years. Indentations normally are at least a fraction of a micrometer deep, producing plastic deformation of a material to insure accurate contact area determination.

Figure 4 is a topographical map of an area of 8750 x 8750 nm² obtained by conventional AFM in contact mode, which contains dentin, DEJ and enamel. The color scale is proportional to the height variation (z-scale of 300 nm). Close to the DEJ a step in height resulted from polishing. A protrusion was observed at the bottom of the image (white arrow), which was used as a marker for subsequent mapping.

Figure 5a shows the contact force image of the area displayed in Fig. 4, calculated from the measured displacement and previously calibrated transducer spring constant. The average force across the scan was held at 1.6 μN. The variation in the dentin area was larger than in the enamel since the feedback error signal was more active due to the rougher surface. The protrusion could not be detected from this image, as expected. Figure 5b represents the displacement amplitude X_0 (nm) and Figure 5c shows the phase

difference between the displacement modulation and the applied force modulation ϕ (deg.). This amplitude was about 0.2 nm for enamel as compared to 0.7 to 0.8 nm in dentin, while the protrusion was about 0.3 nm. The protrusion (shown using arrows) and enamel had lower amplitudes of modulation, indicating these materials were harder than dentin.

Knowing these phase differences and amplitude variations of modulation, along with the spring constant and damping coefficient of the transducer, the variations of stiffness and damping of the sample were calculated at each pixel, using equations 8 and 9. Finally the storage and loss moduli of the area were calculated from equations 11 and 12, and displayed in images in Fig. 6. In these images quantitative variations in values are shown as different color values. The loss components of dry dentin and enamel were relatively small compared to storage components, suggesting that the storage modulus was practically equal to that of the elastic modulus. However, clearly, the damping coefficient was larger for dentin than enamel, suggesting that dentin is more viscoelastic than enamel. The average magnitudes of storage modulus for enamel and dentin were 63 GPa and 21 GPa, respectively. However, appreciable local variations in both dentin and enamel were evident from the cross sections drawn across the DEJ, as shown in the figure. This could not be deduced easily from conventional indentation techniques. The figure also was used to obtain variations of DEJ width, by measuring the change in properties across 256 cross sectional lines accessible on a single image. This function is shown in Figure 6. By fitting a Gaussian distribution function to the data, the average width of DEJ was 2500 nm and the full width half maximum was 700 nm.

It is important to emphasize that the present apparatus cannot be used for soft materials since the minimum applied force is $\sim 1 \mu\text{N}$ with the transducer employed. It has been reported that the compressive strength of dentin is 20.8 MPa (Craig et al., 2002). In general, when using modulus mapping, the calculated contact radius is much less than the radius of curvature of the tip. Therefore, even for dentin, application of $3 \mu\text{N}$ of force and a tip with radius of curvature of 150 nm can reach this compressive strength and cause a plastic signature on the surface. This is shown in Figure 7, where a scan of $5 \mu\text{m}$ with $3.0 \mu\text{N}$ was performed first, then a $10 \mu\text{m}$ scan was obtained to include the previous scan, with force modulation of $1.5 \mu\text{N}$. As a result, the signature of the initial scan (square) is evident and the values for storage and loss moduli were drastically altered as a result of plastic deformation of the area.

In the dentin microstructure each dentin tubule is surrounded by a highly mineralized zone, $\sim 1 \mu\text{m}$ thick, called the peritubular dentin (See Fig. 1). The junction (PIJ) between the peritubular and intertubular dentin has been particularly difficult to study. Previous qualitative imaging of the PIJ was carried out using the force modulation mode of a standard Digital Instruments (DI) AFM (Kinney et al., 1996a). The results revealed a sharp interface between peritubular and intertubular dentin. However, since then, abrupt changes in mechanical properties across the PIJ have been difficult to document (Kinney et al., 1999). The loss and storage moduli of 3 normal dentin (occlusal) samples are shown in Figures 8, 9, and 10. The variations of the elastic moduli along cross-sections shown as white lines also are included. For the three samples, the peritubular dentin exhibited a mean of 48 GPa for storage modulus, 24% lower than enamel. As shown in Figures 9 and 10, the PIJ width for these lines in samples 2 and 3

was about 0.5 μm . However, larger width measurements for the PIJ also were found, as shown in Figure 7, where the PIJ width for that line was about 0.8 μm . The PIJ width distribution functions for all three samples studied in are shown in Figures 8, 9, and 10. The most probable width was 0.7 μm (FWHM = 0.3), which is about a third of the width of the DEJ.

Using the present technique, a typical scan took approximately 10 minutes. However, after the scan was completed, 256 lines of data were available with 256 data points in each line. These data points then were transferred to a spreadsheet and analyzed in a matter of minutes. Since the probing remained in the elastic region, the spatial resolution depended only on the radius of curvature of the tip and the contact area. This contact area, using equation 10, was calculated as 15 nm for dentin and 20 nm for enamel. In conventional indentation techniques; however, separation between indentations is required to be large enough to avoid the effects of residual stress and plastic deformation from the neighboring indents.

Discussion

The new modulus mapping method allowed evaluation of both storage and loss moduli for small areas of calcified tissues with high spatial resolution. This permitted the first quantitative determinations of these modulus variations at the dentin-enamel junction and peritubular-intertubular dentin junction. The width estimates for the DEJ were in good agreement with estimates extracted from variations in frictional properties made by nanoscratching (Habelitz et al, 2001). Quantitative studies of PIJ width have not previously been made to our knowledge.

WEST LIBRARY
UNIVERSITY OF MICHIGAN
1997

This approach appears to have substantial advantages over discrete nanoindentation. For cube-corner diamond tips, the lateral dimension of the indentation is greater than the depth of indentation. Therefore, to avoid error in elastic modulus due to possible interaction between adjacent indentations, a separation of 5 to 10 times the lateral indentation dimensions is used as a general guide, which means a minimum separation of two micrometers. As a result, junctions on the order of a few micrometers cannot be accurately probed by this method. For junctions connecting materials with large differences in mechanical properties, such as the DEJ, the softer material dictates the minimum separation required. This clearly can be seen in Fig. 3a, as the indentations in the enamel zone are far apart, while in dentin they almost touch one another, causing concerns about the accuracy of the measurements. As a result, determination of local variation at the nanometer level is practically impossible using this technique. Modulus mapping in the form of SPM images described here can overcome these shortcomings. This is because the material under the tip is probed within the elastic region; and therefore, once the tip force is removed, the material returns to its original shape with no local residual stress or permanent deformation. The current technique can only be used to determine mechanical property variation in a small area (maximum of $50\mu\text{m} \times 50\mu\text{m}$). This can be extremely useful when investigating narrow transition zone widths and local variations of mechanical property; however, for larger areas, this technique would be inconvenient and time consuming since a typical scan of $20\mu\text{m} \times 20\mu\text{m}$ takes 10-20 minutes.

The intertubular storage modulus measured in this study was 21 GPa (range of 17-23 GPa). The storage modulus for enamel (near the DEJ) was 63 GPa (range of 51-74 GPa).

These values, as indicated in Table 1, are generally consistent with previous studies using discrete nanoindentation (Kinney et al., 1996a; 1999). This study is the first that is known to evaluate the loss modulus of enamel, dentin or the peritubular dentin. The loss modulus values are small for both enamel and peritubular dentin, supporting the fact that both tissues are elastic brittle solids. In this study, the PIJ width was measured as 0.5-2 μm . Due to the small transition zone width of the peritubular-intertubular junction, this zone has been relatively unnoticed (Weiner et al., 1999), and study of both peritubular dentin and the PIJ mechanical properties have received little attention (Kinney et al., 1999; 1996b). In previous work the indentation modulus of peritubular dentin was estimated as 29 GPa, while the values in this study were between 40 and 50 GPa. The higher values in this study could be a result of, but are not limited to, the age, race, location or gender of the samples and these possibilities are being investigated.

The higher loss modulus of intertubular dentin compared to enamel and peritubular dentin is due to high concentration of collagen fibrils in the dentin matrix. As a result, dentin is more viscoelastic than both enamel and peritubular dentin. This is a result of higher energy dissipation as heat while dentin is deformed in comparison with enamel and peritubular dentin. The higher loss modulus makes dentin less prone to fracture. Even though the values of loss moduli in peritubular dentin and enamel are low, the loss modulus of peritubular dentin is generally less than enamel. This could be due to the fact that peritubular dentin has a lower overall protein content than enamel. It should be mentioned that all the experiments in this study were performed in dry conditions. To perform experiments in liquid, one has to account for the meniscus force applied to the

UNIVERSITY OF
MICHIGAN
LIBRARY

tip holder that is partially immersed in liquid. In the present design this force varies as the tip assembly is partially immersed in liquid.

Summary

The local variations in AFM-based nanomechanical properties of human intertubular dentin, enamel, dentin-enamel junction (DEJ) and peritubular-intertubular dentin junctions (PIJ) were obtained with viscoelastic modulus imaging. The data suggested a DEJ width of 2-3 μm . Earlier studies using a Vickers microindentation indenter indicated the DEJ transition zone width was 27-100 μm . One might attribute this dramatically large range to the 50 μm step size and large indentation size used (17 μm) (White et al., 2000). More recently, the DEJ width was estimated using a Berkovich nanoindenter with a step size of greater than 2 μm that gave values of 15-25 μm (Fong et al., 2000). This led to studies of the transition zone using a cube corner nanoindenter with a step size of 1-2 μm that yielded the DEJ width of 10-13 μm (Marshall et al., 2001). A wide range of different probes has been used to study these transition zone widths and as the step sizes decreased, so did the transition zone width values. Nanoscratching results agreed with values found in this study indicating a DEJ width of 1-3 μm (Habelitz et al., 2001).

Values for storage modulus for dry enamel were in good agreement with elastic modulus values from nanoindentation studies (Habelitz et al, 2001, Marshall et al, 2001) and enamel had low loss modulus values. Values for dry intertubular dentin storage modulus were also close to values previously reported, but intertubular dentin also exhibited a significant loss modulus, indicative of its viscoelastic character.

UNIVERSITY OF
MICHIGAN
JAN 10 2001

Acknowledgment

This research was supported by National Institutes of Health/ National Institute of Dental and Craniofacial Research Grants R01DE13029 and P01DE09859.

UNOT LIBRARY

References

- Asif, S.A. Syed, Wahl, K.J., Colton, R.J., 1999. Nanoindentation and contact stiffness measurement using force modulation with a capacitive load-displacement transducer. *Review of Scientific Instruments* 70, 2408-2413.
- Asif, S.A. Syed, Wahl, K.J., Colton, R.J., Warren, O.L., 2001. Quantitative imaging of nanoscale mechanical properties using hybrid nanoindentation and force modulation. *Journal of Applied Physics* 90, 1192-1200.
- Craig, R.G., Powers, J.M., 2002. *Restorative Dental Materials*.
- Fong, H., Sarikaya, M., White, S. N., Snead, M. L., 2000. Nano-Mechanical properties profiles across dentin-enamel junction of human incisor teeth. *Materials Science and Engineering C7*, 119-128.
- Habelitz, S., Marshall, S.J., Marshall G.W Jr., Balooch, M., 2001. Mechanical properties of human dental enamel on the nanometer scale. *Archives of Oral Biology* 46, 173-183.
- Habelitz, S., Marshall, S.J., Marshall, G.W. Jr., Balooch, M., 2001. The functional width of the dentino-enamel junction determined by AFM-based nanoscratching. *Journal of Structural Biology* 135, 294-301.
- Johnson, K.L. 1985. *Contact Mechanics* (Cambridge: University Press), 464pp.
- Kinney, J.H., Balooch M., Marshall, S.J., Marshall, G.W., Weihs, T.P., 1996a. Atomic force microscope measurements of the hardness and elasticity of peritubular and intertubular dentin. *Journal of Biomechanical Engineering* 118, 133-135.
- Kinney, J.H., Balooch, M., Marshall, S.J., Marshall, G.W., Weihs, T.P., 1996b. Hardness and young's modulus of human peritubular and intertubular dentine. *Archives of Oral Biology* 41, 9-13.

UJOL LIBRARY

Kinney, J.H., Balooch, M., Marshall G.W. Jr., Marshall, S.J., 1999. A micromechanics model of the elastic properties of human dentine. *Archives of Oral Biology* **44**, 813-822.

Marshall, G. W., Balooch, M., Gallagher, R. R., Gansky, S. A., Marshall, S. J., 2001. Mechanical properties of the dentino-enamel junction. AFM studies of nanohardness, elastic modulus and fracture. *Journal of Biomedical Materials Research* **54**, 87-95.

Pethica, J. B., Hutchings, R., Oliver, W. C., 1983. Hardness measurement at penetration depths as small as 20 nm. *Philosophical Magazine A* **48**, 593-606.

Weiner, S., Veis, A., Beniash, E., Arad, T., Dillon, J.W., Sabsay, B., Siddiqui, F., 1999. Peritubular dentin formation: crystal organization and the macromolecular constituents in human teeth. *Journal of Structural Biology* **126**, 27-41.

White, S. N., Paine, M. L., Luo, W., Sarikaya, M., Fong, H., Yu, Z. K., 2000. The dentino-enamel junction is a broad transitional zone uniting dissimilar bioceramic composites. *Journal of the American Ceramic Society*, **83**, 238-240.

UNIVERSITY OF
MICHIGAN LIBRARY

Tables

Table 1. Comparison of biomechanical properties with various probes

<i>Probe Type</i>	<i>Load</i>	<i>Step Size</i>	<i>DEJ Width</i>	<i>Enamel Elastic Modulus</i>	<i>Peritubular Dentin Elastic Modulus</i>	<i>Intertubular Dentin Elastic Modulus</i>	<i>PLJ Width</i>
Vickers microindentation	147 mN	50 μm	27-100 μm				
Berkovich nanoindentation	1 mN	>2 μm	15-25 μm				
Cube Corner nanoindentation	500 μN	1-2 μm	10-13 μm	72.7-87.5 GPa	28-32 GPa	17.7-21.1 GPa	
Micro-Raman spectroscopy		1 μm	6-8 μm				
Spherical nanoscratching	300 μN	40 nm	1-3 μm				
This Work	2.5 μN	30 nm	2-3 μm	60-70 GPa	40-50 GPa	17-23 GPa	.5-8 μm

Figures and Captions

Figure 1

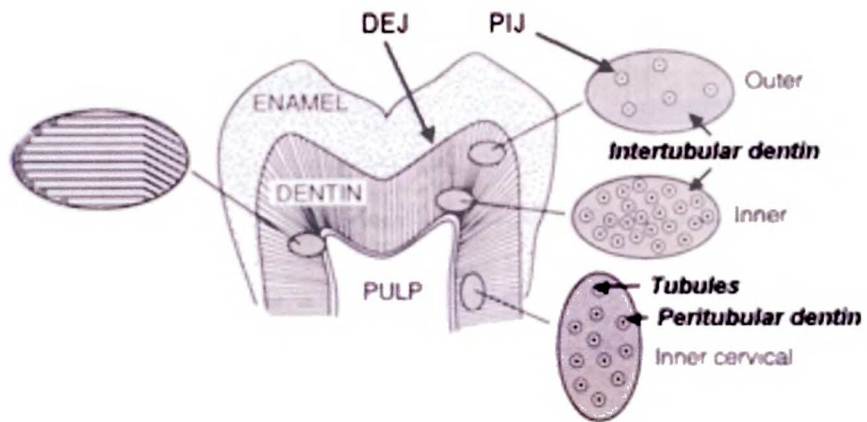


Figure 1. Schematic diagram of the tooth with important interfaces.

UWAT LIBRARY

Figure 2

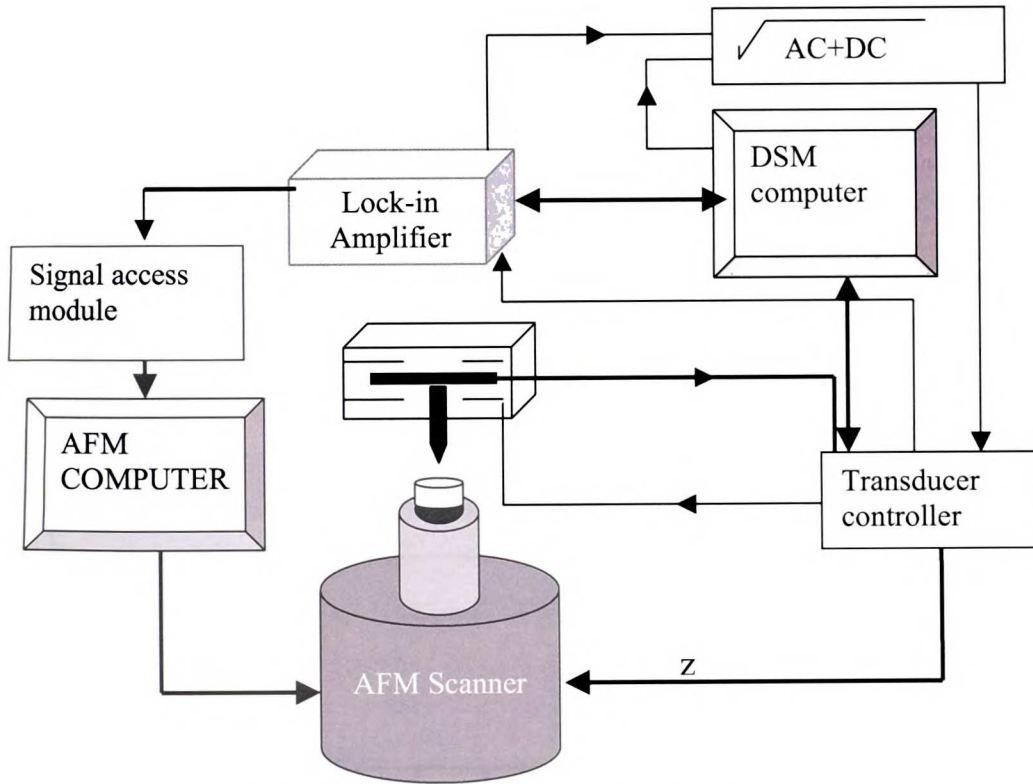


Figure 2. Schematic diagram of the stiffness imaging technique

UJST LIBRARY

Figure 3a

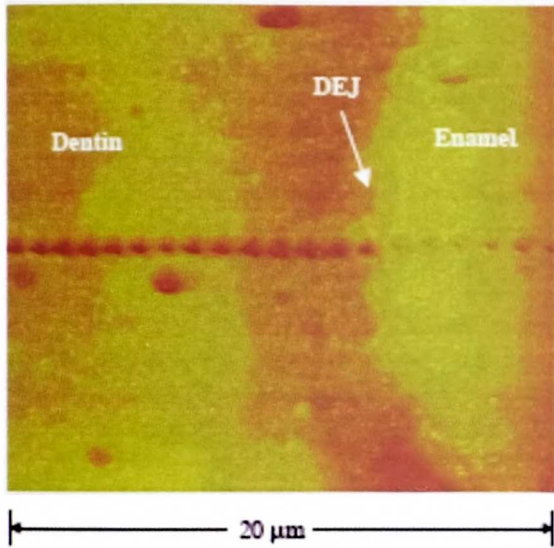


Figure 3b

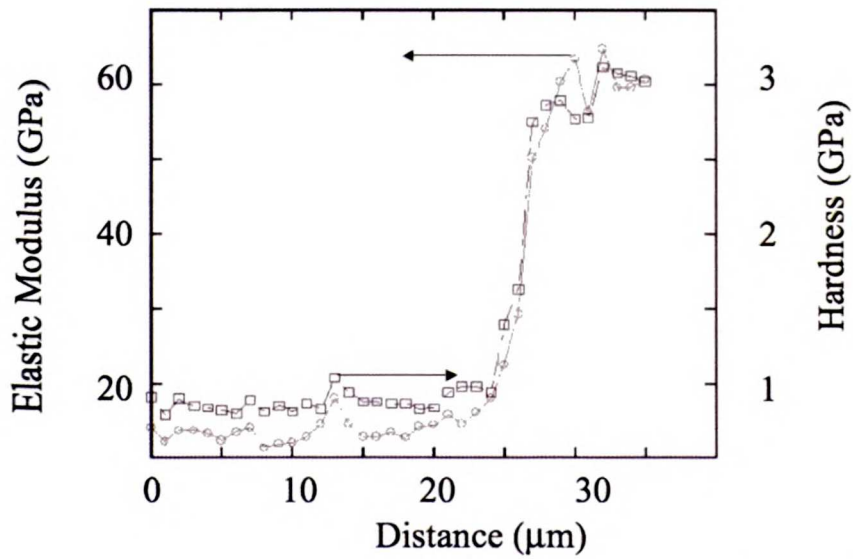


Figure 3. (a) Indentations across the dentin-enamel junction: Topographic image. (b) Elastic Modulus and Hardness

UOJ LIBRARY

Figure 4

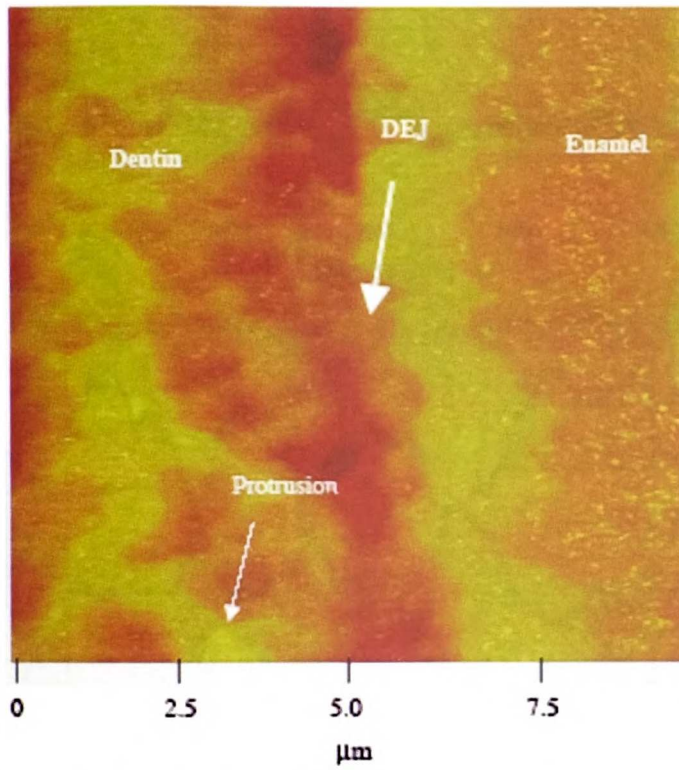


Figure 4. Topography of DEJ

UWST LIDYAN I

Figure 5.

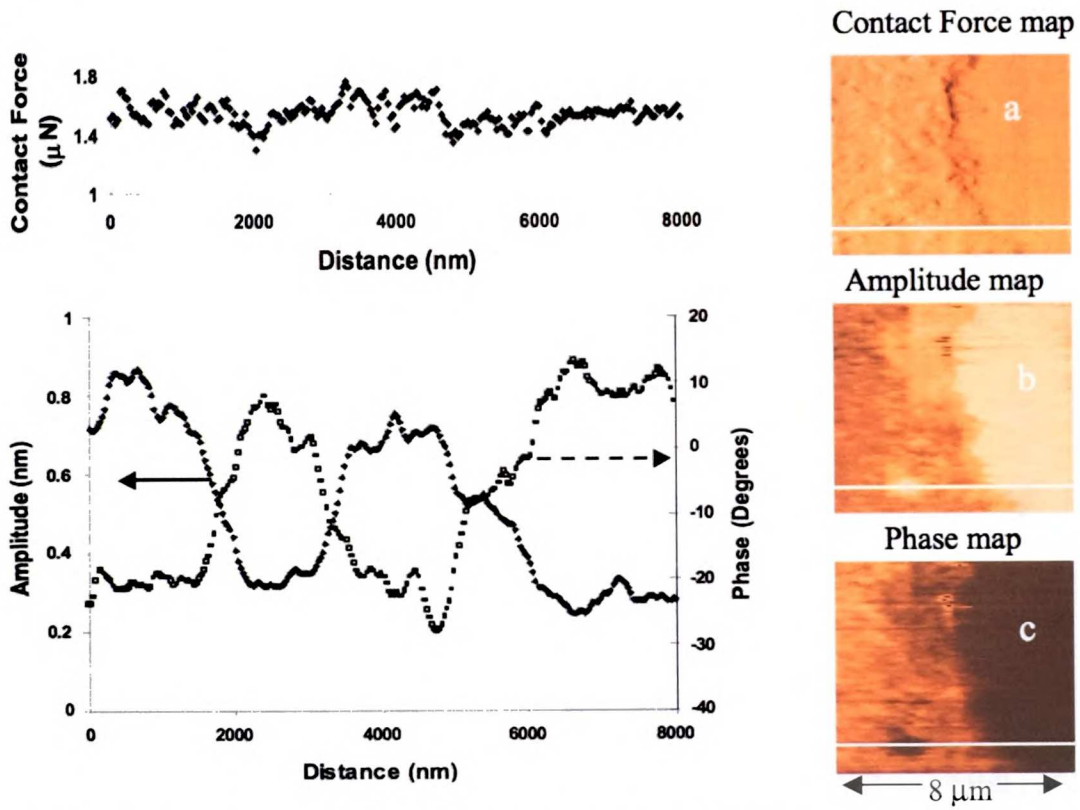


Figure 5. Images and specific site cross sections of the DEJ. (a) the contact force, (b) the amplitude, and (c) the phase shift.

Figure 6.

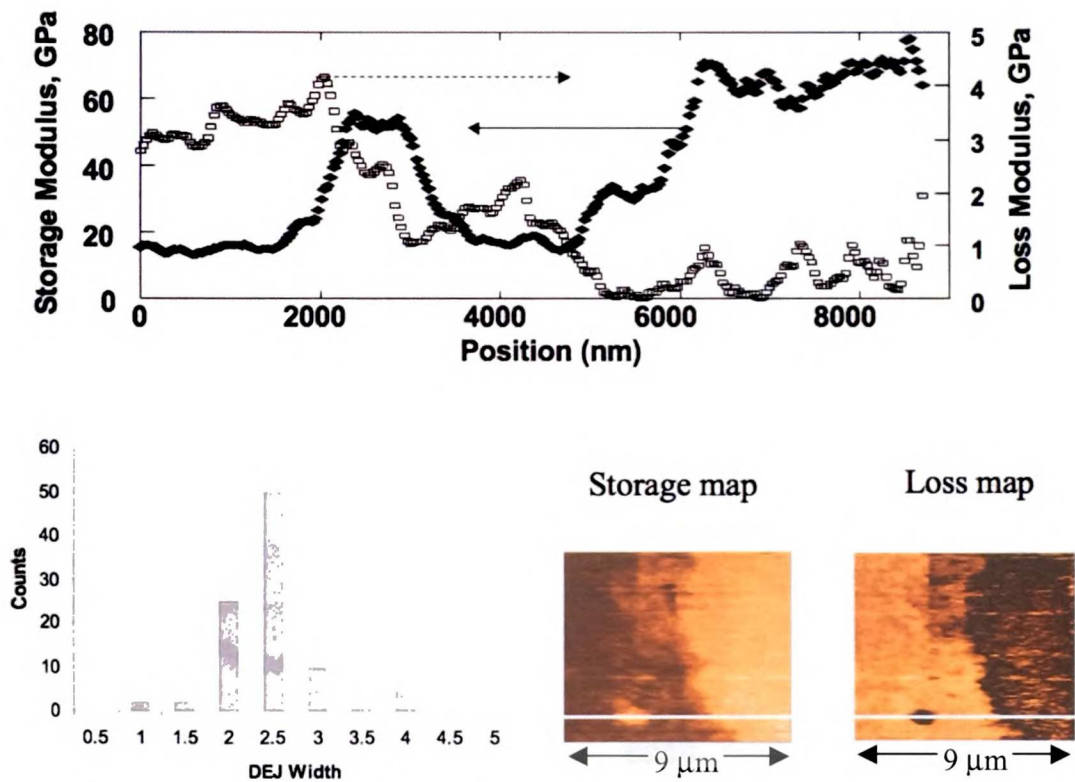


Figure 6. DEJ storage and loss variation cross-sections (top) and corresponding storage and loss maps (lower right); DEJ width estimates at lower left.

UWF LIBRARY

Figure 7

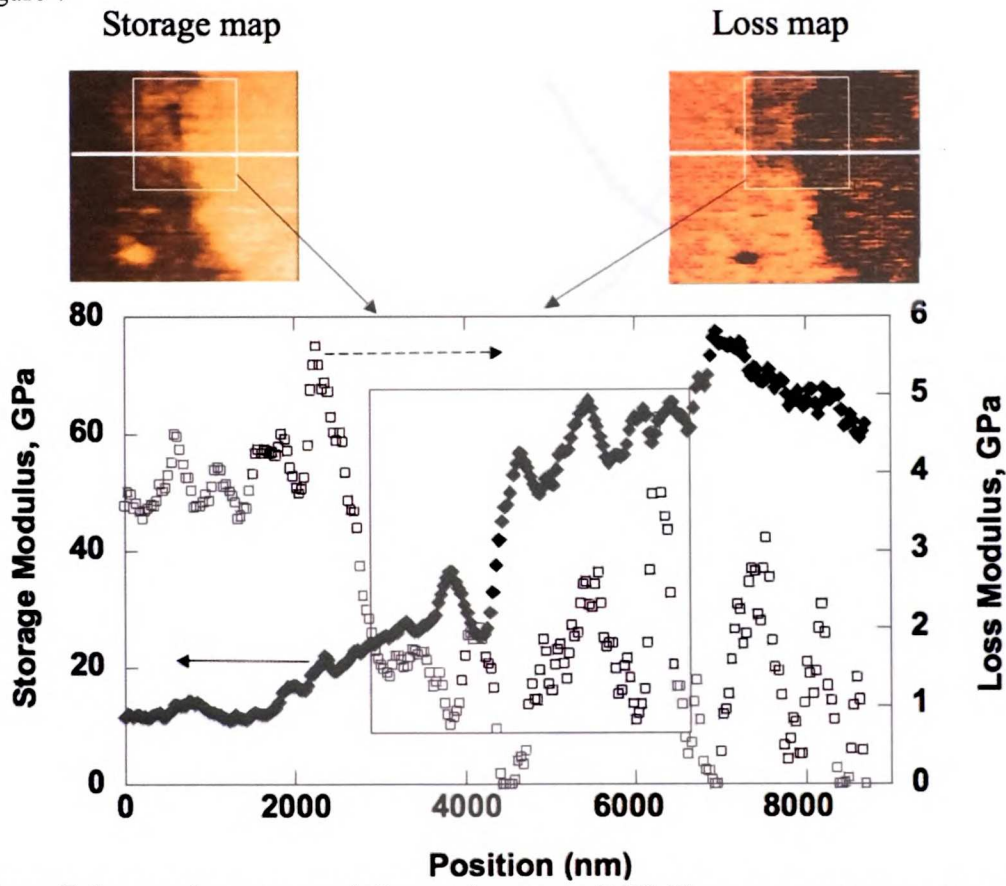


Figure 7. Loss and storage moduli mapping across DEJ. The square area was scanned previously with higher force causing an indentation.

UWF LIDIANI

Figure 8

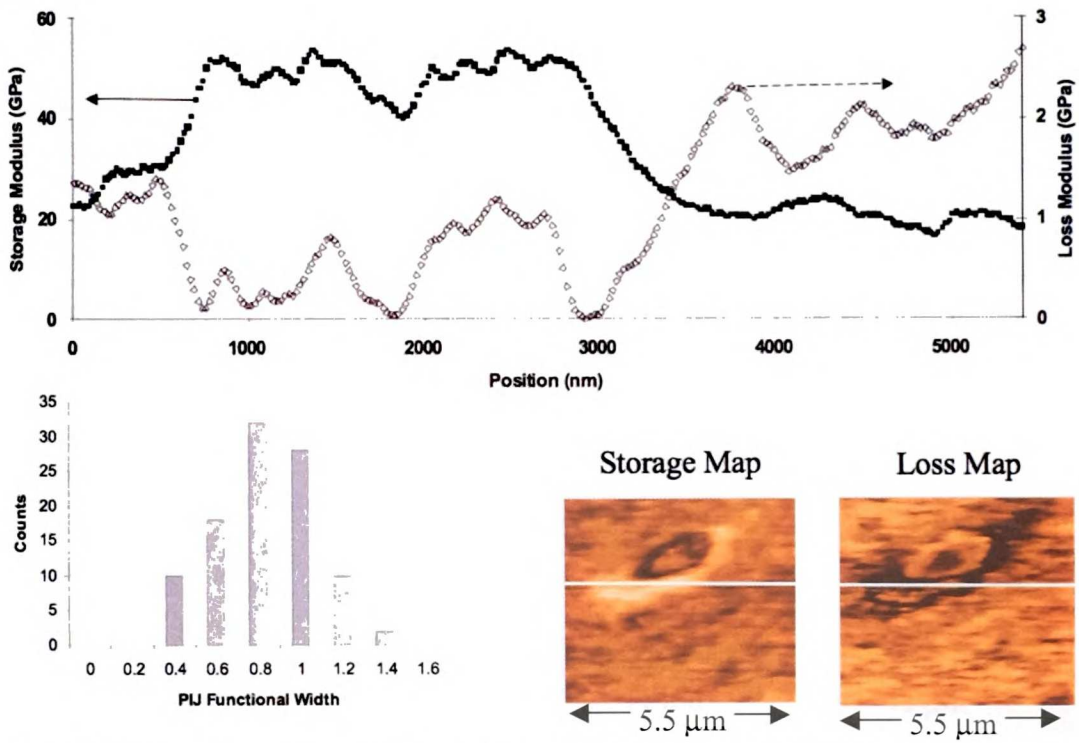


Figure 8. Loss and storage modulus mapping of PIJ Sample 1 and its distribution function.

UWF LIBRARY

Figure 9

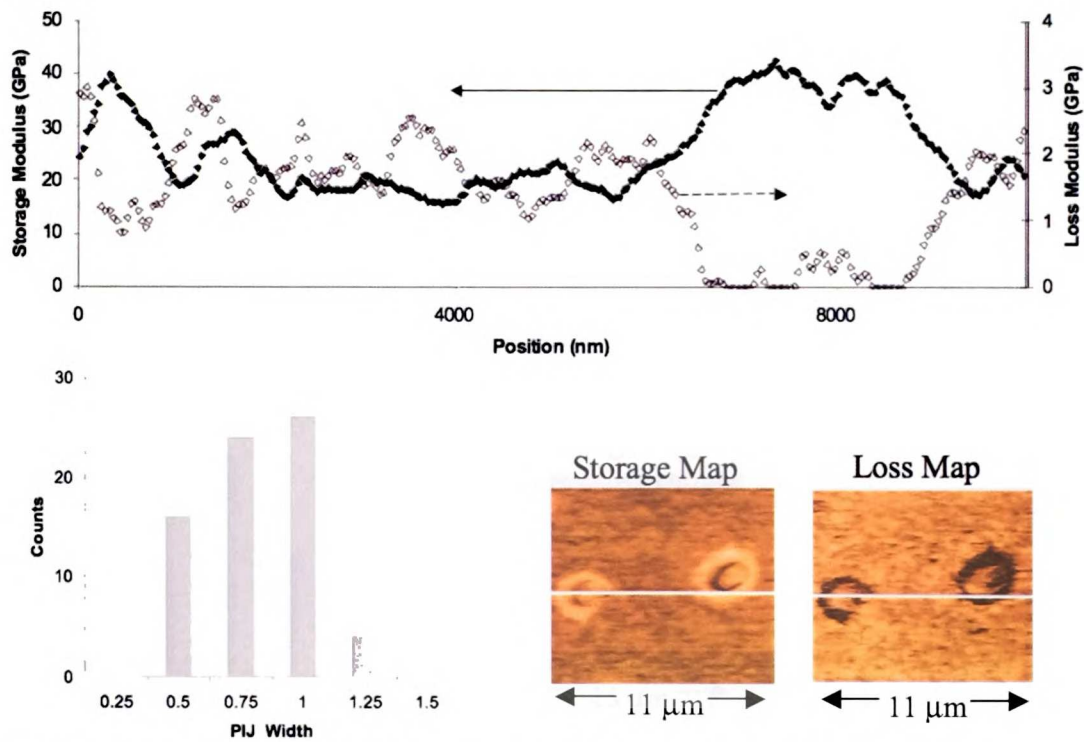


Figure 9. Loss and storage modulus mapping of PIJ Sample 2 and its distribution function.

WUOL LIBRARY

Figure 10

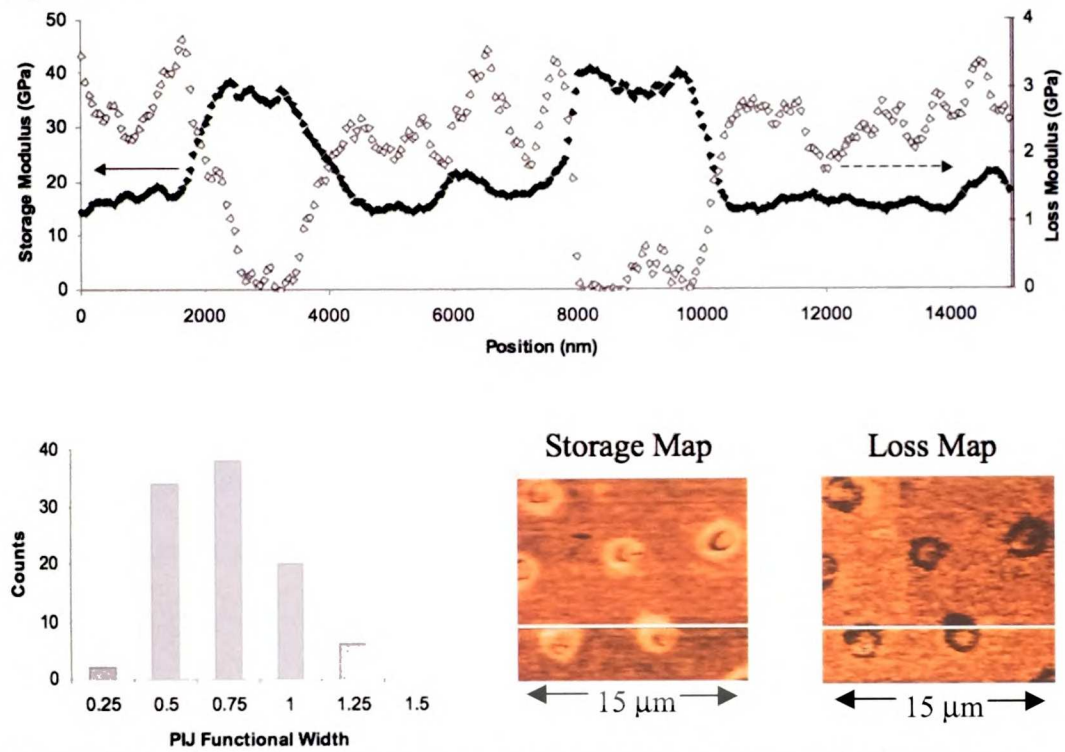


Figure 10. Loss and storage modulus mapping of PIJ Sample 3 and its distribution function.

Chapter 4

Glucocorticoid treated mice have localized changes in trabecular bone material properties and osteocyte lacunar size that are not observed in placebo treated or estrogen deficient mice

Reprinted from: Nancy E. Lane, Wei Yao, Mehdi Balooch, Ravi K. Nalla, Guive Balooch, Stefan Habelitz, John H. Kinney, and Lynda F. Bonewald. (2006) **Glucocorticoid treated mice have localized changes in trabecular bone material properties and osteocyte lacunar size that are not observed in placebo treated or estrogen deficient mice** *J Bone Miner Res.* 21:466-476
With permission from the American Society of Bone and Mineral Research (ASBMR).

11/10/07 10:00

MicroAbstract

The purpose of this study was to assess changes in bone microstructure in glucocorticoid, GC, treated mice. In addition to a reduction in trabecular bone volume, GC treatment reduced bone mineral and elastic modulus of bone adjacent to osteocytes that was not observed in control mice nor estrogen deficient mice. These microstructural changes would amplify the increased bone fragility due to macrostructural changes in this metabolic bone disease.

Abstract

Introduction: Patients with glucocorticoid-induced secondary osteoporosis tend to fracture at higher bone mineral densities than patients with postmenopausal osteoporosis. This suggests that glucocorticoids may alter bone material properties in addition to bone mineral density and bone macro-structure.

Methods: We assessed the changes in the fifth lumbar vertebral body for trabecular bone structure (microCT and histomorphometry), elastic modulus of individual lumbar vertebrae trabecula (Scanning Probe Microscopy), mineral to matrix ratio (Raman microspectroscopy), whole bone strength (3rd lumbar vertebral body compression testing), and bone turnover (serum and urine biochemical markers and histomorphometry) in prednisolone-treated mice and placebo-treated controls for comparison to estrogen deficient mice and sham-operated controls.

Results: Significant reductions in trabecular bone volume and whole bone strength occurred in both prednisolone-treated and estrogen deficient mice compared to controls after 21 days ($p < 0.05$). The average elastic modulus over the entire surface of each trabecula was similar in all the experimental groups. However, localized changes within the trabeculae in areas surrounding the osteocyte lacunae were observed only in the prednisolone-treated mice. The size of the osteocyte lacunae was increased, reduced elastic modulus around the lacunae was observed, and a “halo” of hypomineralized bone surrounding the lacunae was observed. This was associated with reduced (nearly 40%) mineral to matrix ratio determined by Raman microspectroscopy. These localized changes in elastic modulus and bone mineral to matrix ratio were not observed in the other three experimental groups.

Conclusions: Based on these results, it appears that glucocorticoids may have direct effects on osteocytes resulting in a modification of their microenvironment. These changes, including an enlargement of their lacunar space and the generation of a surrounding sphere of hypomineralized bone, appear to produce highly localized changes in bone material properties that may influence fracture risk.

Key Words: Glucocorticoid, mice, elastic modulus, mineralization, bone strength

11/11/17 10:20

Introduction

Glucocorticoid treatment is frequently associated with an increase in the risk of bone fracture, especially in the spinal vertebrae and the femoral head (1,2,3). Glucocorticoids alter bone metabolism, which in turn decreases bone density and affects trabecular bone architecture. These changes in trabecular bone architecture and bone density do not explain the observed increase in fracture risk as individuals treated with glucocorticoids frequently experience bone fractures at higher bone mineral densities than women with postmenopausal osteoporosis (4,5).

The explanation for bone fragility in adults with either estrogen deficient osteoporosis or glucocorticoid-induced osteoporosis is that changes in bone remodeling are responsible for altered trabecular bone volume and architecture such that the bone can no longer resist load; and therefore, fractures occur (6,7). Indeed, iliac crest biopsies from patients with bone loss due to estrogen deficiency demonstrate reductions in trabecular bone volume, trabecular number and connectivity and these are associated with an increase fracture risk (6,8). Recently, biochemical markers of bone turnover have emerged as surrogate measures of bone remodeling activity at the bone surface that can predict fracture risk independent of bone mass (9). Individuals with high levels of bone turnover markers and low bone mineral density have a higher risk of fracture (9). Postmenopausal women who take bone active agents that reduce bone remodeling, eg. bisphosphonates,

11/11/17 10:27

and have reductions in bone turnover markers are protected against bone fracture whether due to postmenopausal osteoporosis or glucocorticoid-induced osteoporosis (10,11,12).

Individuals treated with glucocorticoids also have alterations in bone remodeling (2,6,13). These alterations in bone remodeling include an increase in bone resorption and suppression of bone formation such that reductions in trabecular bone mass and architecture occur, including reductions in trabecular thickness and trabecular number (6,7,13,14,15). The mechanisms behind these changes have been proposed to be alterations in bone cell viability. Glucocorticoids reduce the lifespan of osteoblasts and osteocytes through apoptosis while increasing osteoclast viability (14,15). While these proposed alterations in bone cell lifespan could explain the reduction in bone formation markers and trabecular bone architecture, neither of these observations completely explains the increased bone fragility observed in glucocorticoid-induced osteoporosis that is not observed with postmenopausal osteoporosis.

11/11/17 10:20

Therefore, we hypothesized that in addition to its alteration of bone mass and trabecular bone architecture; glucocorticoids may also alter the localized material properties of trabecular bone, thereby increasing bone fragility. To test this hypothesis we have evaluated trabecular bone from mice treated with prednisolone, placebo, and estrogen deficient ovariectomized mice and sham-operated controls.

Material and Methods

Animals and Experimental procedures:

For the glucocorticoid study, 6-month-old male Swiss-Webster mice were obtained from Charles River, Inc. (San Jose, CA). The mice were maintained on commercial rodent chow (22/5 Rodent Diet; Teklad, Madison, WI) available ad libitum with 0.95% calcium and 0.67% phosphate. Mice were housed in a room that was maintained at 70⁰F with a 12-hour light/dark cycle. The mice were randomized by body weight into 2 groups with 8 animals each. Slow release pellets (Innovative Research of American, Sarasota, FL) of placebo or 1.4 mg/kg/d of prednisolone were administered for 21 days by subcutaneous implantation (15).

For the estrogen deficiency study, 6-month old Swiss –Webster female mice were obtained from Charles River, Inc. (San Jose, California). Animals were either Sham-operated or ovariectomized (OVX) by the dorsal approach as previously described (16,17). The animals were sacrificed 21 days after surgery. All animals were treated

11/11/17 10:50

according to the USDA animal care guidelines with the approval of the UCSF Committee on Animal Research (16).

For all study animals, calcein (10mg/kg i.p.) was given 14 and 4 days before sacrifice to determine bone formation surface and rate. One day prior to sacrifice, the mice were housed in individual metabolic cages and a fasting 24-hour urine sample was collected. Serum samples were obtained during necropsy and both the urine and serum samples were stored at -80°C prior to the assessment of biochemical markers of bone turnover. At necropsy, the mice were exsanguinated by cardiac puncture and successful removal of the ovaries in the OVX group was confirmed by failure to detect ovarian tissue and marked atrophy of the uterine horns. At the time of sacrifice, the 3rd and 5th lumbar vertebral body (LVB) and femurs were placed in 10% phosphate-buffered formalin for 24 hours and then transferred to 70% ethanol for micro-CT, bone histomorphometry, scanning probe microscopy, cell apoptosis and whole bone compression measurements.

Biochemical markers of bone turnover:

Urinary levels of deoxypyridinoline cross-links and creatinine (DPD/Cr) were analyzed in duplicate using enzyme linked immunoassay (ELISA) kits from Quidel (Mountain View, CA). Serum levels of osteocalcin (OSC) were measured using a mouse sandwich ELISA kit from Biomedical Technologies (Stroughton, MA). The manufacturer's protocols were followed and all samples were assayed in duplicate. A standard curve was generated from each kit and the absolute concentrations were extrapolated from the standard curve. The coefficients of variation (CVs) for inter-assay and intra-assay

measurements were less than 8% for DPD, Cr, and OSC (16,17), which is similar to the manufacturer's reference.

Micro-computed tomography, Micro-CT:

The 5th lumbar vertebral body from each of the animals were scanned with a desktop MicroCT (μ CT viva 40, Scanco Medical, Bassersdorf, Switzerland), with an isotropic resolution of 10.5 μ m for the vertebral body in all three spatial dimensions (18). The number of slices varied according to the size of the vertebrae, ranging from 300 to 400 slices per specimen for the vertebral body. The scans were initiated in the sagittal plane of the vertebral body, covering the entire cortical and trabecular bone of the vertebral body. The scanning was initiated from the left periosteal margin to the right periosteum. The sagittal plane was chosen instead of the axial plane because this position compensates for the irregularity of the growth plate. Therefore, secondary spongiosa was consistently selected, and the primary spongiosa was excluded from analysis.

3D trabecular structural parameters were measured directly, as previously described (18). Mineralized bone was separated from bone marrow with a marching cube 3D segmentation algorithm in which the grayscale images were segmented using a constrained Gaussian filter ($\sigma = 0.8$, support = 1) to remove noise, and a fixed threshold (235 grayscale value for vertebrae) was used to extract the structure of the mineralized tissue. Bone volume (BV) was calculated using tetrahedrons corresponding to the enclosed volume of the triangulated surface. Total volume (TV) was the volume of the sample that was examined. A normalized index, BV/TV, was utilized to compare

samples of varying size. The methods used for calculating trabecular thickness (Tb.Th), trabecular separation (Tb.Sp) and trabecular number (Tb.N) have been described (19).

Cortical thickness was expressed as the average cortical thickness of 3 sections. For the vertebral body, one section was the center section, and the other two sections were 20 sections or 320 microns lateral to the center section. Both cortexes were measured at the middle height of the vertebral body. These methods have been used and previously published by our research group (16,17).

Bone histomorphometry:

The 5th lumbar vertebral bodies were dehydrated in ethanol, embedded undecalcified in methylmethacrylate and sectioned longitudinally with a Leica/Jung 2255 microtome at 4 μm and 8 μm thick sections. Bone histomorphometry was performed using a semi-automatic image analysis Bioquant system (Bioquant Image Analysis Corporation, Nashville, TN) linked to a microscope equipped with transmitted and fluorescence light (20,21).

A counting window, allowing measurement of the entire trabecular bone and bone marrow within the growth plate and cortex, was created for the histomorphometric analysis. Static measurements included total tissue area (T.Ar), bone area (B.Ar) and bone perimeter (B.Pm). Dynamic measurements included single- (sL.Pm) and double-labeled perimeter (dL.Pm), osteoid perimeter (O.Pm), and interlabel width (Ir.L.Wi). These indices were used to calculate bone volume (BV/TV), trabecular number

UNIVERSITY OF TENNESSEE

(Tb.N), trabecular thickness (Tb.Th) and trabecular separation (Tb.Sp), mineralizing surface (MS/BS), percentage of osteoclast surface (Oc.S) and mineral apposition rate (MAR). Surface-based bone formation rate (BFR/BS) was calculated by multiplying mineralizing surface (single labeled surface/2 + double labeled surface) by MAR according to Parfitt et al. (20,21). We have reported similar methodology in other experiments in our laboratory (16,17,19).

Measurement of apoptosis in undecalcified bone sections:

Osteocyte apoptosis assays were performed using the undecalcified bone sections. The sections were mounted, deplasticized, and incubated in 20 µg/ml of proteinase K in PBS for 15 minutes at room temperature. Apoptotic cells were detected using terminal deoxynucleotidyl transferase (TdT)-mediated deoxyuridinetriphosphate (dUTP) nick end-labeling (TUNEL) technology by using an in-situ cell detection kit, Peroxidase (POD) (Roche Applied Science, Indianapolis, IN). The sections were then counterstained with 1% methyl green. Negative controls were generated by omitting the TdT from the labeling mix. ApopTag positive controls were generated from weaned rat mammary tissue fixed in 10% formalin (22). To calculate the percentage of osteocyte apoptosis, an average of 2000 ± 216 (SD) osteocytes were counted per vertebral bone section (this included all trabeculae in the section). The percentage of apoptotic osteocytes was expressed as the number of apoptotic osteocytes divided by the total number of osteocytes present per vertebral bone section. Only osteocytes within the trabeculae were

11/11/17 10:20 AM

assessed from this analysis. These methods are similar to those reported by Weinstein et al (14, 15, 23, 24).

Elastic modulus mapping by Scanning Probe Microscopy:

A force modulation technique, elastic modulus mapping (EMM), was used to quantitatively map dynamic nanomechanical properties across the surface of the individual trabeculae with high spatial resolution (~15 nm). Modulus maps in the form of Scanning Probe Microscopy (SPM) images were acquired using the direct force modulation-operating mode of a TriboScope nanoindenter (Hysitron, Minneapolis, MN) mounted on a Multimode atomic force microscope (AFM) controlled by NanoScope IIIa electronics (Veeco, Santa Barbara, CA) (25). For this experiment, the conventional AFM head was replaced by an electrostatic operated transducer that allowed for simultaneous topographic and elastic modulus imaging. The electrostatic force acting on the spring-suspended center plate of the force-displacement transducer of the nanoindenter was sinusoidally modulated at 200 Hz while contact mode imaging was conducted. A cube corner diamond tip was attached to this transducer. The amplitude and the phase of the resulting transducer displacement signal were measured with a dual-channel lock-in amplifier. This information was used to determine the local indentation moduli of the sample at each pixel in the imaging process. The tip contact radius was determined by calibration using a quartz sample with known 69.7 GPa elastic modulus. When the tip was examined by SEM, the resulting tip radius was in good agreement (90%) with this calibration radius (25).

UNIVERSITY OF MINNESOTA

To prepare the specimens for EMM, the methylmethacrylate embedded lumbar vertebral bodies that had been used to generate sections for bone histomorphometry were further polished with different diamond pastes, starting from 10 μ m down to 0.1 μ m in diameter, to obtain smooth surfaces. The measurements were performed on 3 randomly selected vertebral specimens per treatment group and on all of the trabeculae that were in the specimen, roughly 6-10 different trabeculae from each sample. The amplitude of the modulated electrostatic force was set to 0.5 to 1.0 μ N to maintain a good signal-to-noise ratio, but sufficiently small to prevent plastic deformation of the sample. Voigt and Hertzian models were used to extract the elastic modulus map of 256 X 256 pixels from the amplitude and phase of displacements at each pixel (25-27). The entire surface area of each trabecula was covered in a mosaic fashion by small-overlapping individual 50 by 50 μ m scans. After obtaining the elastic modulus image for each trabecula, the images were separated into different zones based on the elastic modulus results. Statistical analyses of the variations in elastic moduli were performed both on the entire trabecula as well as the individual zones.

Determination of mineral to matrix ratios using Raman microspectroscopy:

Raman microspectroscopy was used to determine the inorganic (mineral) to organic (matrix) ratio of trabecular bone tissue surrounding the osteocyte lacunae across one trabecula from prednisolone-treated and placebo groups. Raman spectra and resulting images were recorded using monochromatic radiation emitted by a He-Ne laser (632.8 nm), operating at 20 mW on a HR 800 Raman spectrophotometer (JobinYvon, Horiba, France). With the confocal capability of the instrument, a laser beam spot of less than 1

11/11/17 10:20

μm can be focused just below the surface to minimize the effect of possible surface contamination by the methylmethacrylate surrounding the bone.

The intensity values of the spectra obtained from the inorganic component, represented by PO_4^{3-} (960 cm^{-1}) band peaks (apatite), were compared to the organic component (matrix), represented by the Amide I peak at 1670 cm^{-1} . For the image acquisition, an area of ~ 70 by $70\text{ }\mu\text{m}$ was scanned pixel-by-pixel with a step size of $1\text{ }\mu\text{m}$ and an acquisition time of 30 s. The matrix and mineral bands were obtained separately. All measurements were made systematically under the same conditions, utilizing $\sim 1\text{ }\mu\text{m}$ depth in laser penetration. A computer-controlled translation stage was used to move the specimen under the laser beam in $1\text{ }\mu\text{m}$ increments. The spectral processing of the data included the subtraction of the background luminescence from the total spectra and deconvolution of the peaks by curve fitting the Raman peaks and comparing the total area ratios to maximum intensity ratio calculations (28, 29). In the present study, the two provided negligible differences in the results.

Lacunar size and volume measurement:

We assessed lacunar size and volume by two different methods. The sizes of lacunae were estimated using SPM imaging of polished cross sectional areas of trabecular bone using the same diamond tip utilized for elastic modulus mapping. The lacunae with the largest areas were located and assumed to be the closest approximation to the mid-cross section of a 3-D ellipsoidal lacuna. These methods are similar to those reported by other investigators (30,31). The error in the measurement of lacunar size, assessed by repeating

11/11/17 10:11 AM

our measurements on 100 randomly selected lacunae, was approximately $10 \mu\text{m}^2$, and therefore, was estimated to be approximately 10%.

Biomechanical testing:

After sacrifice, the 3rd lumbar vertebrae were excised from all mice from each experimental group (n=8 per group) and stored in Hanks' Balanced Salt Solution until just before testing. The relevant cross-sectional dimensions and the height of the specimens were measured using an optical microscope (Olympus STM-UM Measuring Microscope, Olympus American Inc., Melville, NY; 0.5um resolution), after which they were subjected to unconfined compression tests along the long axis of the 3rd lumbar vertebra. The tests were performed using a mechanical test frame (ELF 3200 TEC Inc. Minnetonka, MN) with a cross-head displacement rate of 0.01 mm/s, and involved loading the samples to failure, while continuously recording the corresponding loads and displacements. The measured cross-sectional dimensions, length and height, were used to determine the compressive strength and compression modulus following Akher et al (32).

Statistical Analysis:

The group means and standard deviations (SDs) were calculated for all outcome variables. Statistical differences between the prednisolone-treated and control groups and OVX and sham-operated groups were analyzed using Students t-test for continuous variables and chi-squared tests for dichotomous variables. The nonparametric Kruskal-Wallis test with post-hoc comparisons (SPSS Version 10; SPSS Inc., Chicago, IL, USA) was used to assess the differences in elastic modulus and osteocyte lacunae size across

11/11/17 10:00

the vertebral trabeculae in the placebo, prednisolone, sham-operated and OVX mice. In all of the analyses, a priori, $p < 0.05$ was considered statistically significant.

Results

General Observations:

The animals tolerated the surgery and the implantation of the pellets without complications. The mice implanted with prednisolone pellets had a modest weight loss over the first 7 days of the study (10% below baseline) but then regained weight such that there were no differences in weights at day 21 between prednisolone and placebo treated animals. The mice that were OVX or sham-operated and observed over 21 days had a weight increase of 14-21% over baseline values ($p < 0.05$ within groups); however, no significant differences between the two groups was observed at day 21.

Trabecular and cortical bone changes measured by micro-CT:

Fifth Lumbar Vertebral Body. At day 21, compared to the placebo treated mice, total trabecular bone volume was 22% lower ($p < 0.05$) in the prednisolone-treated animals (Table 1). Although trabecular connectivity was on average 10% lower, trabecular number was 4% lower and trabecular thickness was 7% lower in the prednisolone treated animals compared to the controls (no statistical difference). The cortical thickness was 15% lower in prednisolone-treated mice compared to the placebo ($p < 0.05$). Compared to the sham-operated mice, total trabecular bone volume was approximately 18% lower, trabecular connectivity was 12% lower and trabecular number was 7% lower in OVX mice ($p < 0.05$).

Raman Microspectroscopy determination of mineral to matrix ratios:

Figure 2 shows examples of a Raman image of Amide I peaks (matrix) and phosphate peaks (major component of apatite) over methylmetacrylate (Figure 2a) and around an osteocyte lacuna from a prednisolone-treated animal and a placebo treated animal (Figure 2b). The lower values are signified by the darker color. There is a loss of mineral as shown by a halo of the Amide I and phosphate peaks around the osteocyte lacunae from the prednisolone-treated animals, compared to the placebo group. To quantify the reduction in mineral surrounding the osteocyte lacunae, we determined the ratio of phosphate to Amide I as plotted along a horizontal line in each sample evaluated (Figure 2c). The mean value within the “halo” zone around the osteocyte lacuna in GC mice shows approximately a 40% reduction in mineral to matrix ratio from a normal value of approximately 9 in the placebo and estrogen deficient samples to a ratio of approximately 6 in the prednisolone-treated sample.

Quantification of osteocyte lacunae size and osteocyte apoptosis:

We utilized the images obtained by SPM to calculate the cross-sectional area of the lacunae from 3 vertebral bone sections from 4 experimental groups (placebo, prednisolone, sham-operated and OVXed). The mean values and standard deviations are shown in table 4. The prednisolone-treated and OVX lacunae midsection areas are statistically larger than the placebo and sham-operated animals ($p < 0.05$), while prednisolone treated lacunae were larger than OVX ($p < 0.05$). Assuming an ellipsoid shape, the lacunar volume were estimated as $402.4 \mu\text{m}^3$ for placebo, $477.3 \mu\text{m}^3$ for prednisolone-treated, $405.3 \mu\text{m}^3$ for sham-operated, and $426.4 \mu\text{m}^3$ for OVX samples.

osteocyte lacunae was not seen in either the estrogen deficient or the control mice. The reduction in elastic modulus surrounding the osteocyte lacunae was accompanied by a reduction in the mineral to matrix ratio. Similar to estrogen deficiency, changes in trabecular microarchitecture and whole bone strength occur, but unlike estrogen deficiency, changes in mechanical integrity surrounding osteocytes along with increased lacunar size are observed. These data suggest that glucocorticoid induced bone fragility occurs not only from changes in the trabecular microarchitecture but is compounded by changes in the local mechanical properties of the bone tissue itself (33).

Earlier studies have shown that glucocorticoids induce both osteoblast and osteocyte apoptosis *in vitro* and *in vivo* in both mice and humans (14,15,23,24,34). Weinstein and coworkers have found that glucocorticoid treatment of mice resulted in reduced bone formation, increased bone resorption and increased apoptosis of osteocytes and osteoblasts (15). We found greater numbers of apoptotic osteocytes in prednisolone-treated mice compared to the controls, but substantially less than reported by Weinstein et al (14,25). Bellido et al reported in an *in vitro* study that glucocorticoids induced apoptosis of osteocytes (35). They assessed apoptosis with three different types of assays (trypan blue exclusion, nuclear morphology, and Annexin V/Propidium iodide ratios by FACS analysis) to accurately detect apoptosis and not non-programmed cell death (35). However, within bone slices, only the TUNEL assay can be utilized, and in the present study, we may have missed the detection of some of the osteocytes within the prednisolone- treated bone undergoing apoptosis.

O'Brien et al reported prednisolone-treated mice had lower bone strength measured by compression testing of the 5th lumbar vertebrae than the control group (23). The major predictors of bone strength are total bone volume and architecture. Prednisolone-treated mice showed reductions in both total trabecular bone volume and trabecular thickness compared to the control group. In addition, the reduction in bone strength was similar between the prednisolone-treated mice and the estrogen deficient mice, albeit the gender was different. Since both of these bone loss models have reductions in trabecular structure and bone mass of similar magnitude as their controls, we conclude that the loss of trabecular elements (e.g. number, thickness or connections) was the most important element in the reduction in bone strength. However, the alterations observed in the osteocyte microenvironment of demineralization with prednisolone-treatment, may contribute to the overall reduction in bone strength with prolonged periods of prednisolone exposure. Indeed, clinical studies of individuals on glucocorticoids have demonstrated rapid bone loss occurring within a few months of initiating the therapy; however, new fractures are delayed until at least one year (10). Therefore, both trabecular bone structural changes and localized changes within the trabeculae may contribute over time to increased bone fragility in glucocorticoid-treated subjects.

In the present study, we observed changes in elastic modulus surrounding osteocyte lacunae, reduced mineral to matrix ratios in the same areas, and an increase in lacunar size. This suggests that glucocorticoid may alter the metabolism and function of the osteocyte and is not just inducing cell death. It has been hypothesized that the osteocyte can remodel its local environment, which includes both the lacunae and canaliculi (36).

UNIVERSITY OF MICHIGAN

Osteocyte lacunae have been shown to uptake tetracycline, called “periosteocytic perilacunar tetracycline labeling” indicating the ability to calcify or form bone (37). Alternatively, these investigators also found acid phosphatase positive osteocytes near endosteal osteoclastic resorbing surfaces suggesting potential capacity to resorb. They also found greater solubility of the intralacunar mineral surrounding the normal osteocyte (38). These observations suggest that the osteocyte can both add and remove mineral; our data support the latter.

In this study, we also observed larger osteocyte lacunae in prednisolone- treated mice compared to estrogen deficient and control mice. The term “osteolytic osteolysis” was initially used to describe the enlarged lacunae in patients with hyperparathyroidism (39) and later in immobilized rats (40). This term and concept became unfavored and was not used for more than two decades. This may be due to the fact that only enlargement and irregularity of the lacunae were the main morphological findings. Osteolytic osteolysis has been confused with the resorption mechanisms used by osteoclasts. Removal of mineral by osteocytes (weeks/months) would certainly be slower than osteoclastic resorption (days). Removal of mineral by osteocytes may involve a combined proteolytic (enzymes) and leaching (acid phosphatase) process. There are two ways that lacunar ultrastructure can be modified. One is by poor mineralization when the osteocyte is being formed. Bonucci and Gherardi (42) suggested this to be the reason for enlarged lacunae with renal osteodystrophy. In the case of our observations of decreased elastic modulus and halos surrounding osteocyte in prednisolone-treated mice, the original mineralization state of the osteocyte was normal; therefore, the defect must be due to the osteocyte

7. Dalle Carbonare L, Arlot ME, Chavassieux PM, Roux JP, Portero NR, Meunier PJ 2001 Comparison of trabecular bone architecture and remodeling in glucocorticoid-induced and postmenopausal osteoporosis. *J Bone Miner Res* 16:97-103.

8. Parfitt AM, Mathews CHE, Villanueva A, Kleerekoper M, Frame B, Rao DS 1983 Relationships between surface, volume and thickness of iliac trabecular bone in aging and in osteoporosis. Implications for the microanatomic and cellular mechanisms of bone loss. *J Clin Invest* 72:1396-1409.

9. Garnero P, Hausherr E, Chapuy MC, Marcelli C, Grandjean H, Muller C, Cormier C, Breart G, Meunier PJ, Delmas PD 1996 Markers of bone resorption predict hip fracture in elderly women: the EPIDOS Prospective Study. *J Bone Miner Res* 11(10):1531-8.

10. Saag KG, Emkey R, Schnitzer TJ, Brown JP, Hawkins F, Goemaere S, Thamsborg G, Liberman UA, Delmas PD, Malice MP, Czachus M, Diafortis AG 1998. Alendronate for the prevention and treatment of glucocorticoid-induced osteoporosis. *N Engl J Med* 339:292-299.

11. Bauer DC, Black DM, Garnero P, Hochberg M, Ott S, Orloff J, Thompson DE, Ewing SK, Delmas PD 2004 Fracture Intervention Trial Study Group. Change in bone turnover and hip, non-spine, and vertebral fracture in alendronate-treated women: the fracture intervention trial.

J Bone Miner Res 19(8):1250-8.

12. Eastell R, Barton I, Hannon RA, Chines A, Garnero P, Delmas PD 2003 Relationship of early changes in bone resorption to the reduction in fracture risk with risedronate. *J Bone Miner Res* 18(6):1051-6.

13. Dovio A, Perazzolo L, Ostella G, Ventura M, Termine A, Milano E, Bertolotto A, Angeli AJ 2004 Immediate fall of bone formation and transient increase of bone resorption in the course of high-dose, short-term glucocorticoid therapy in young patients with multiple sclerosis. *Clin Endo and Metab* 89(10):4923-4928, 2004

14. Manolagas SC, and Weinstein RS 1999 New Developments in the pathogenesis and treatment of steroid-induced osteoporosis. *J Bone Miner Res* 14 (7): 1061-1066.

15. Weinstein RS, Jilka RL, Parfitt AM, Manolagas SC 1998 Inhibition of osteoblastogenesis and promotion of apoptosis of osteoblasts and osteocytes by glucocorticoids. *J Clin Invest* 102: 2 :274-282.

16. Lane, NE, Yao W, Kinney JH, Modin G, Balooch M, Wronski T 2003 Both hPTH (1-34) and bFGF increase trabecular bone mass in osteopenic rats, however they have different effects on trabecular bone architecture. *J Bone Miner Res* 18(12):2105-2115.

17. Lane NE, Yao W, Nakamura MC, Humphrey MB, Kimmel D, Hunag X, Sheppard , Ross FP, Teitelbaum SL 2005 $\beta 5$ Integrin deficiency increases osteoclast generation and

40. Kremlien B, Manegold C, Ritz E, Bommer J 1976 The influence of immobilization on osteocyte morphology: osteocyte differential count and electron microscopic studies. *Virchows Arch A Pathol. Anat. Histol* 370(1): 55-68.
41. Parfitt AM, 1976 The actions of parathyroid hormone on bone: relation to bone remodeling and turnover, calcium homeostasis, and metabolic bone disease. Part I of IV parts: mechanisms of calcium transfer between blood and bone and their cellular basis: morphological and kinetic approaches to bone turnover. *Metabolism* 25: 809-844.
42. Bonucci E, Gherardi G 1977 Osteocyte ultrastructure in renal osteodystrophy. *Virchows Arch A Pathol Anat Histol* 373(3): 213-31.
43. Heuck F, 1970 Comparative investigations of the function of osteocytes on bone resorption. *Calcif Tissue Res Suppl* 1:148-149.
44. Marie PJ, Glorieux FH. 1983 Relation between hypomineralized periosteocytic lesions and bone mineralization in vitamin D-resistant rickets. *Calcif. Tissue Int.* 35 (4-5): 443-558
45. Bai, X, Miao D, et al. 2002. Partial rescue of the Hyp phenotype by osteoblast-targeted PHEX (phosphate-regulating gene with homologies to endopeptidases on the X chromosome) expression. *Mol. Endocrinol.* 16(12): 2913-25.

Tables

Table 1. Trabecular and Cortical Bone Structural Variables of the 5th Lumbar Vertebral Body Measured by Micro-CT (Mean \pm Standard Deviation)*

Treatment Groups	Trabecular Bone Volume (%)	Trabecular Connectivity (1/mm ³)	Trabecular Number (1/mm)	Trabecular Thickness (μ m)	Cortical Thickness (μ m)
Distal Femur					
1. Placebo	19.7 \pm 1.6	206.8 \pm 34.7	4.8 \pm 0.5	50.7 \pm 0.7	165.5 \pm 32.5
2. Prednisolone	15.4 \pm 2.9 ^a	187.9 \pm 80.6	4.6 \pm 0.9	47.3 \pm 0.8	139.9 \pm 15.4 ^a
3. Sham-operated	20.6 \pm 4.3	184.4 \pm 38.3	4.4 \pm 0.5	47.9 \pm 0.1	99.7 \pm 14.0
4. OVX	16.9 \pm 4.7 ^b	162.7 \pm 52.2 ^b	4.1 \pm 0.5 ^b	43.7 \pm 0.6	86.8 \pm 13.6

a= p < 0.05 from placebo 1; b= p < 0.05 from sham.

*= Statistical tests were performed between groups 1 and 2 (prednisolone vs. placebo) and groups 3 and 4 (OVX vs. sham-operated).

Table 2. Trabecular Bone Static and Dynamic Variables Assessed by Histomorphometry (Mean \pm Standard Deviation)* and number of apoptotic osteocytes (%) from the 5th Lumbar Vertebral Body

Treatment Groups	BV/TV (%)	Tb.N (1/mm)	Tb.Th. (μ m)	Tb.Sp (μ m)	Oc.S (%)	MS/BS (%)	MAR (μ m)	BFR/BS (μ m ³ / μ m ² /d)	Apoptosis Osteocytes (%)
1. Placebo	17.9 \pm 0.7	4.4 \pm 0.5	24.9 \pm 3.5	88.6 \pm 10.0	0.8 \pm 0.1	42.9 \pm 12.9	1.03 \pm 0.04	0.24 \pm 0.05	1.9 \pm 1.1
2. Prednisolone	14.5 \pm 0.3 ^a	4.0 \pm 0.8	14.4 \pm 4.0 ^b	125.0 \pm 17.8 ^b	1.7 \pm 0.4 ^b	29.5 \pm 6.5 ^a	0.64 \pm 0.07 ^b	0.05 \pm 0.01 ^b	3.9 \pm 1.0 ^b
3. Sham-operated	18.6 \pm 1.3	5.5 \pm 1.1	28.5 \pm 2.9	118.0 \pm 11.0	1.3 \pm 0.3	20.9 \pm 8.8	0.90 \pm 0.05	0.20 \pm 0.16	1.0 \pm 0.5
4. OVX	13.1 \pm 4.4 ^b	3.0 \pm 0.8 ^b	22.8 \pm 6.0	156.4 \pm 21.8 ^b	3.3 \pm 0.8 ^b	23.4 \pm 4.5	1.22 \pm 0.11	0.28 \pm 0.06	1.2 \pm 0.6

a= p < 0.05 from group 1; b= p < 0.05 from group 3.

* = Statistical tests were performed between groups 1 and 2 (prednisolone vs. placebo) and group 3 and 4 (OVX vs. Sham-operated).

Table 4. Osteocyte Lacunae size, percentage of osteocytes with reduced elastic modulus around the perimeter of the osteocyte lacunae from the 4 experimental groups (mean \pm SD)

Groups	No. of Lacunae	Mean (μm^2) \pm SD	Number (%) with reduced E (mean <20GPa) around osteocytes
1. Placebo	314	67.1 \pm 5.1	10 (3%)
2. Prednisolone	385	91.8 \pm 4.4 ***	86 (22%)*, **
3. Sham -operated	410	73.0 \pm 5.0	7 (2%)
4. OVX	360	82.0 \pm 4.3*	16 (4%)

*= p<0.05 from Placebo and Sham -operated mice

**= p<0.05 from OVX

Figures and Captions

Figure 1a

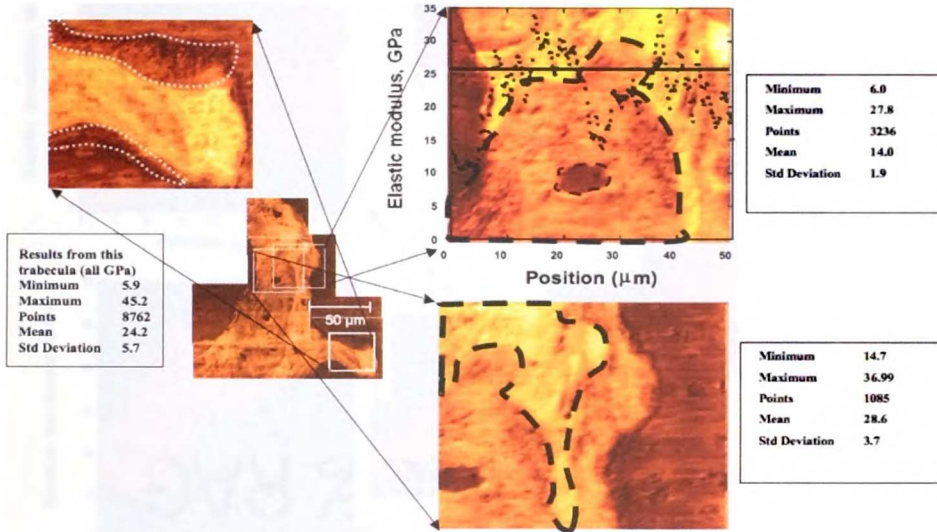


Figure 1b

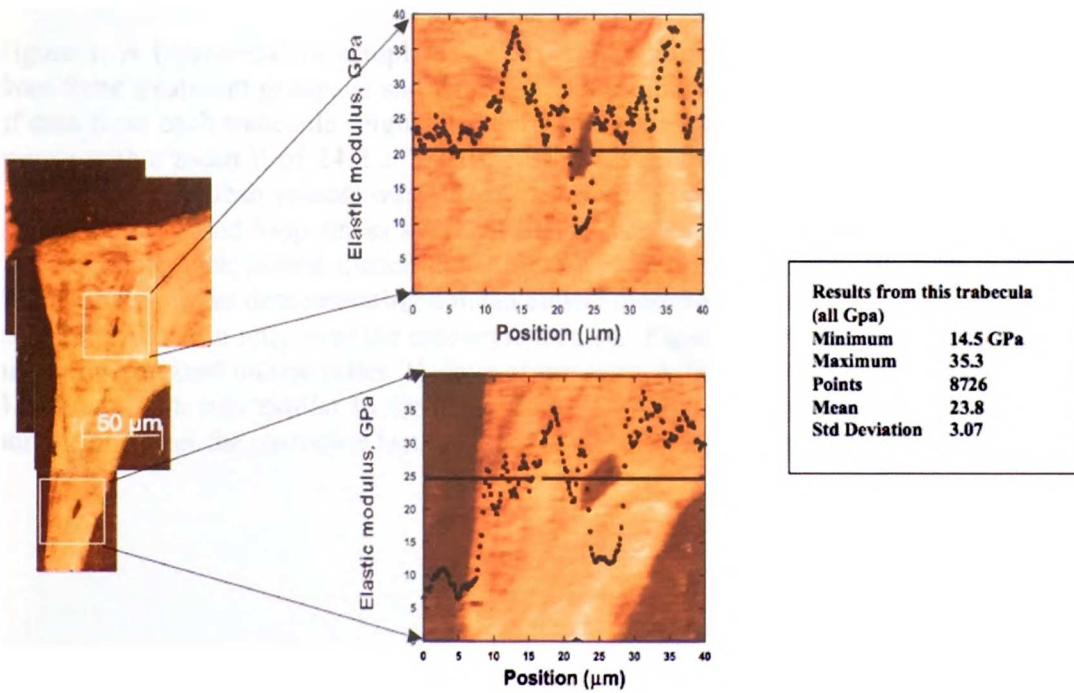


Figure 1c.

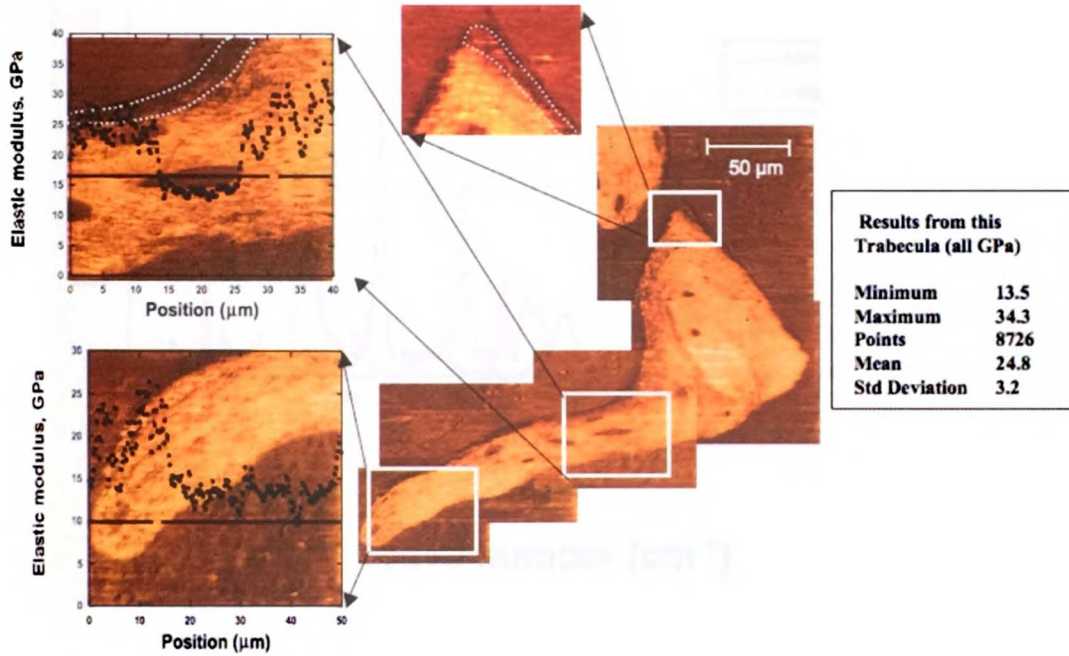


Figure 1. A representative sample of an elastic modulus map of an individual trabecula from three treatment groups is shown. Each figure represents a mean of over 8000 points of data from each trabecula. Figure 1a represents a trabecula from a prednisolone-treated mouse with a mean E of $24.2 \pm 1.9 \cdot 10^9$ Newton/m² (GPa). A significant reduction in E (30% below the mean values) was observed at both the remodeling surface (shown within white dotted closed-loop lines) and around the osteocyte lacunae within the trabeculae (shown with black dotted closed-loop lines). Figure 1b is a trabecula from a placebo treated male mouse demonstrating a mean elastic modulus (E) of 23.8 ± 3.1 GPa with the expected reduction only over the osteocyte lacunae. Figure 1c represents a trabecula from an ovariectomized mouse (after 21 days of estrogen deficiency) with a mean E of 24.8 ± 3.2 GPa, which was similar to the other study groups. E was reduced at the remodeling surface and over the osteocyte lacunae but not surrounding the osteocyte lacunae.

Figure 2a

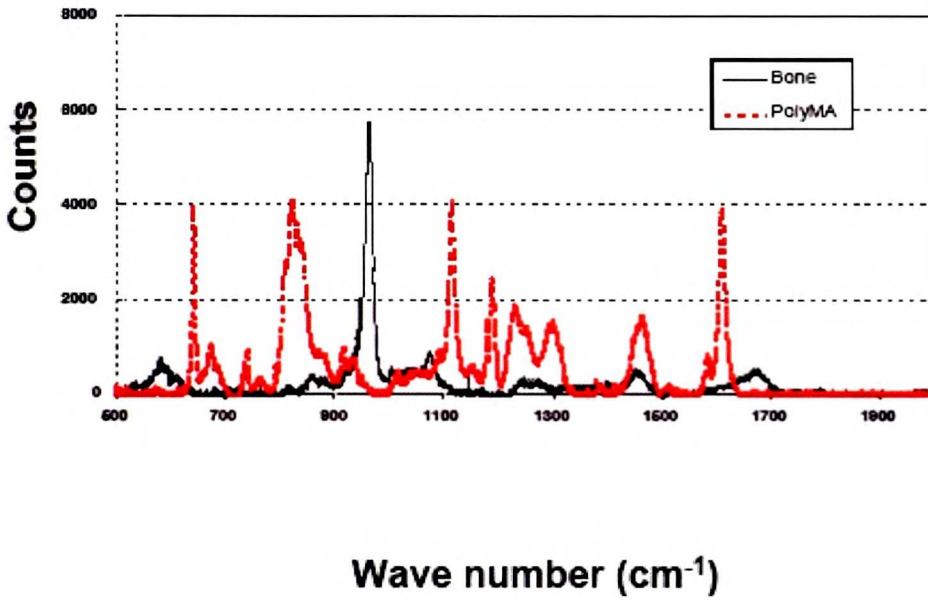


Figure 2b

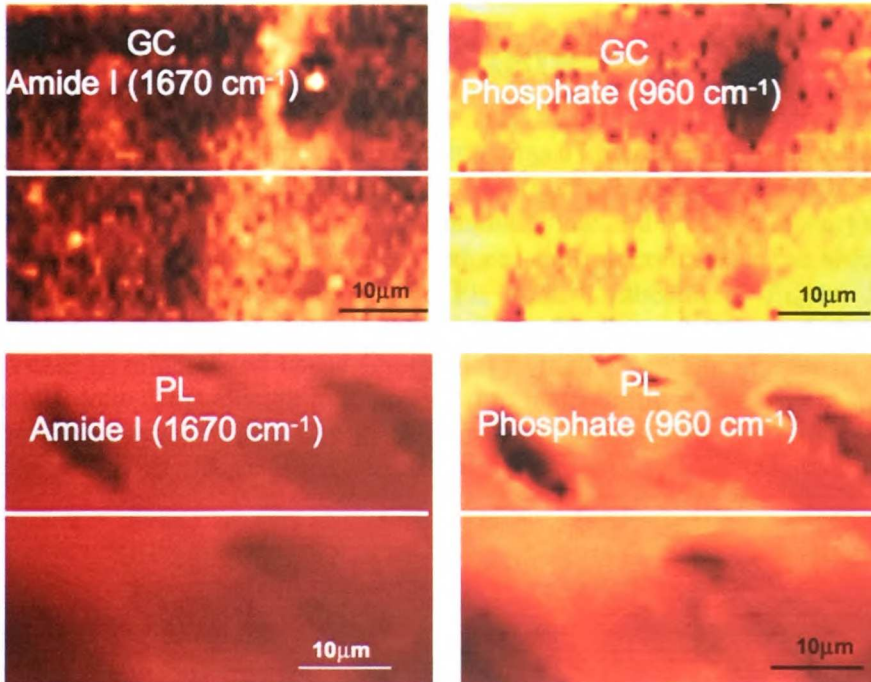


Figure 2c

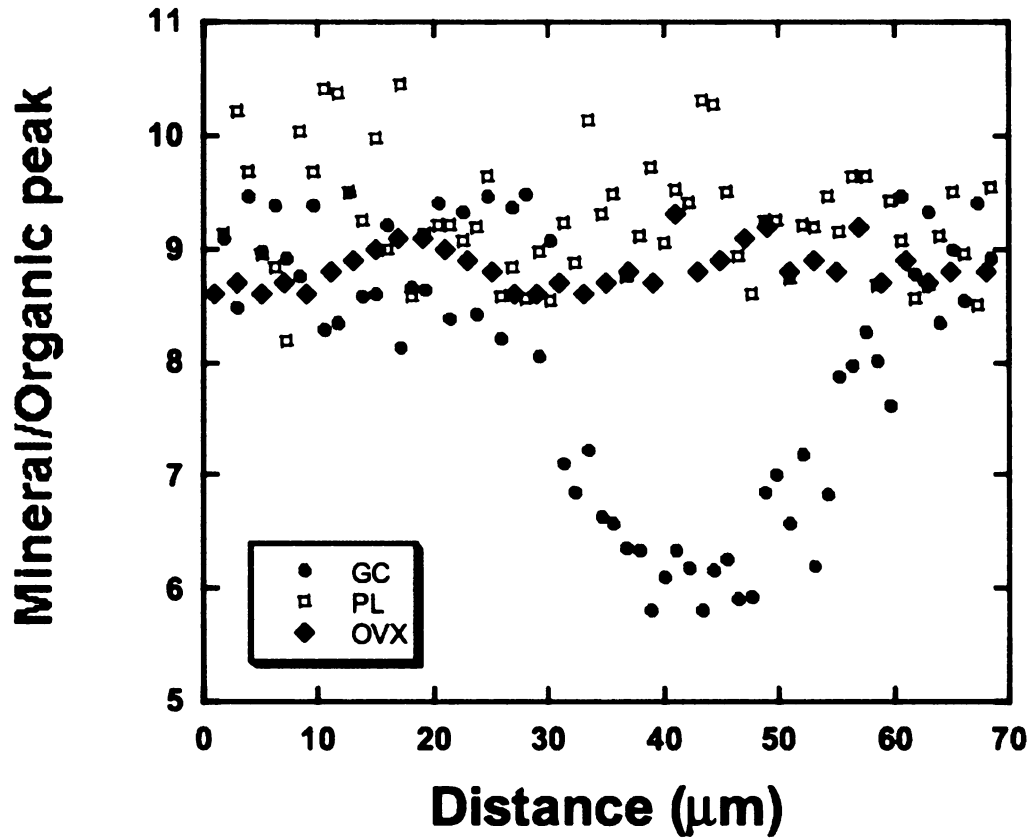


Figure 2. Raman microspectroscopic imaging of prednisolone-treated (GC) and placebo (PL) treated mouse trabecula. Figure 2a represents a comparison of the Raman spectrum of a typical bone embedded in methylmethacrylate and methylmethacrylate alone. Figure 2b demonstrates that GC treatment reduces the mineralized tissue around the osteocyte lacunae and this is not seen in the PL treated trabecula. Figure 2c represents the quantitative mineral to organic ratios along the lines shown in Figure 2b. There is a decrease in mineralized tissue (inorganic) to matrix (organic) peaks in mice treated with prednisolone. This change in the mineral to matrix ratio is not seen in the placebo treated or estrogen deficient (OVX) mice (Figure 2c).

Figure 3

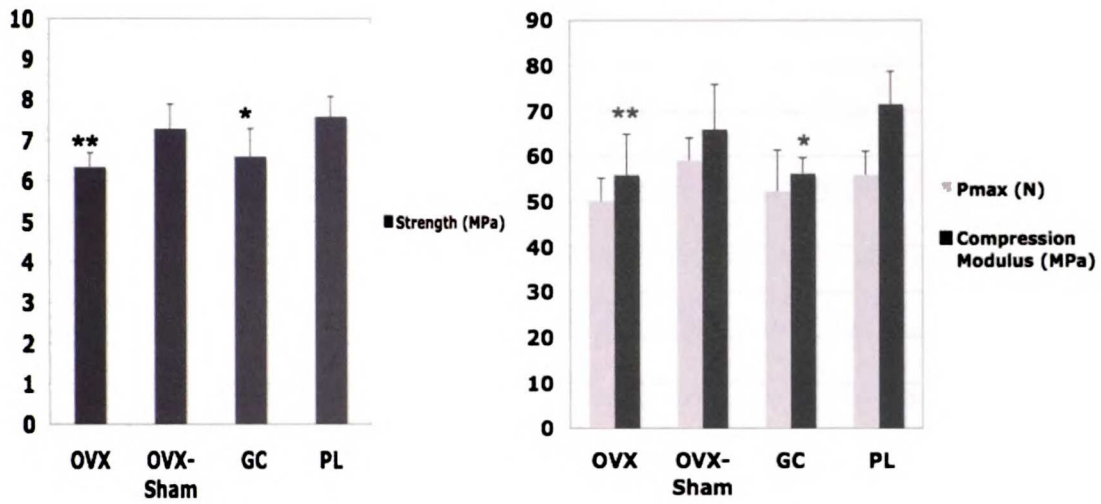


Figure 3. Biomechanical tests of the 3rd lumbar vertebral body of mice from each treatment group (n=8 per group). Animals treated with prednisolone and estrogen deficient mice have significant reductions in all measured mechanical property parameters compared to the control groups.
* p<0.05 from prednisolone-treated mice, and ** p< 0.05 from sham-operated mice.

Chapter 5

TGF- β regulates the mechanical properties and composition of bone matrix

Reprinted from: Guive Balooch, Mehdi Balooch, Ravi K. Nalla, Stephen Schilling, Ellen H. Filvaroff, Grayson W. Marshall, Sally J. Marshall, Robert O. Ritchie, Rik Derynck, and Tamara Alliston (2005) **TGF- β regulates the mechanical properties and composition of bone matrix** *Proceedings of the National Academy of Science*. Dec 27; 102(52):18813-18818. Copyright 2005 National Academy of Sciences, U.S.A.

ABSTRACT

The characteristic toughness and strength of bone result from the nature of bone matrix, the mineralized extracellular matrix produced by osteoblasts. The mechanical properties and composition of bone matrix, along with bone mass and architecture, are critical determinants of a bone's ability to resist fracture. Several regulators of bone mass and architecture have been identified, but factors that regulate the mechanical properties and composition of bone matrix are largely unknown. We used a combination of high-resolution approaches, including atomic-force microscopy, X-ray tomography, and Raman micro-spectroscopy, to assess the properties of bone matrix independently of bone mass and architecture. Properties were evaluated in genetically modified mice with differing levels of TGF- β signaling. Bone matrix properties correlated with the level of TGF- β signaling. Thus, a reduction in TGF- β signaling, through its effector Smad3, enhanced the mechanical properties and mineral concentration of the bone matrix, as well as the bone mass, collectively enabling the bone to better resist fracture. Our results provide the first evidence that bone matrix properties are controlled by growth factor signaling.

INTRODUCTION

The ability of bones to resist fracture is determined by the bone mass and architecture, and the mechanical properties and composition of the bone matrix (1). Bone architecture is, in part, determined by cortical bone thickness, trabecular bone volume and organization. Several signaling pathways, including estrogen, parathyroid hormone, TGF- β and other cytokines, have been implicated in the control of bone mass and architecture and its deregulation in metabolic bone diseases such as osteoporosis (2, 3). Much less is known about the mechanical properties and composition of bone matrix, the unique protein- and mineral-rich extracellular material produced by osteoblasts and osteocytes. However, the importance of bone matrix quality is clinically apparent in bone disorders such as osteogenesis imperfecta and osteopetrosis (4, 5). Osteopetrosis patients have increased bone fragility despite elevated bone mass (4). Presumably bone matrix properties are highly regulated, but the regulators themselves are unknown, partly due to the inaccessibility of methods to define these properties independently of bone mass and architecture. Nevertheless, the regulation of bone-matrix properties must be understood to more effectively treat bone disorders.

TGF- β plays stage-dependent roles in osteoblast and osteoclast differentiation. TGF- β inhibits osteoblast differentiation, yet stimulates the proliferation of mesenchymal progenitors, thereby expanding the cell population that will differentiate into osteoblasts (6). TGF- β signals through a complex of type I and type II transmembrane serine/threonine kinases (7). Upon ligand binding, the receptor complex phosphorylates the intracellular effector Smad3, which translocates to the nucleus to interact with specific transcription factors to regulate gene expression (7, 8). For example, TGF- β -

activated Smad3 binds Runx2 at the runx2 and osteocalcin promoters to repress transcription of genes required for osteoblast differentiation and bone matrix production (9, 10). TGF- β also regulates the expression of other bone matrix proteins including osteopontin, osteonectin, type I collagen, and matrix metalloproteinases (11, 12). As these proteins play roles in bone matrix organization and mineralization (13), the regulation of their expression by TGF- β may affect the material properties of bone matrix.

We utilized high-resolution biomechanical and imaging techniques to investigate the role of TGF- β signaling in the regulation of the composition and mechanical properties of bone matrix, independently of its effects on bone mass and architecture. These bone matrix properties were defined using transgenic mice with alterations in TGF- β signaling in their osteoblasts. We found that TGF- β regulates the mechanical properties and mineral concentration of bone matrix, which contributes to its resistance to fracture. Furthermore, reduced TGF- β signaling increased functional parameters of bone quality. These observations identify TGF- β as a key regulator of mechanical properties and composition of the bone matrix and provide the first evidence that these properties are regulated by cytokines and growth factors.

MATERIALS AND METHODS

Mice and tissue isolation

The phenotypes of Smad3^{-/-}, DNT β RII, D4, and D5 mice have been described (14-17). D4, D5 and DNT β RII mice were bred on a B6D2 background. Smad3^{+/-} and Smad3^{-/-}

mice were analyzed in C57Bl6 and 129/C57Bl6 backgrounds, with no detectable background-dependent differences. Mutant mice from each line were compared to wild-type littermates. The four wild-type groups were indistinguishable on all parameters tested. Either a representative image or an average value of the four wild-type groups is shown in the figures. Mice were genotyped using PCR analysis. Details are available upon request. Following euthanasia, femurs, tibiae, and calvarial parietal bones were isolated and cleaned of muscle tissue or dura mater. For histomorphometry and von Kossa staining, tissues were fixed in PBS-buffered formalin (2).

Atomic Force Microscopy (AFM)-based nanoindentation

Bones embedded in epoxy resin were cross-sectioned and polished to minimize surface roughness as described (18). An AFM-Triboscope system (Nanoscope III, Digital Instruments, Santa Barbara, CA) was used to perform nanoindentation testing under dry conditions as described (19). Nanoindentations with a load range from 300-600 μN produced load-deformation curves, from which the elastic modulus was calculated (Fig. 1b). Hardness was calculated based on the contact area, indentation load and contact stiffness, S , defined as the slope of the unloading curve. Sixty serial nanoindentation points, arranged in lines at least 30 μm long with a 2 μm step size were placed across the mid-tibial cortical bone of at least three animals of each genotype. Cross sections of cortical mid-femur, distal tibia, and central parietal bones were also tested.

Elastic Modulus Mapping (EMM)

INSTITUTIONAL LIBRARY

EMM of 3 or more sections of cortical mid-tibia per animal were performed under the same conditions as AFM with nanoindentation. Quantitative modulus maps were acquired using direct-force modulation (18). Briefly, by applying a small sinusoidally modulated force ($\sim 3 \mu\text{N}$) to the transducer of the nanoindenter, elastic-modulus mapping measures 256×256 pixels of modulus values with a 15 nm resolution without plastically deforming the material. The measurements and the tip contact radius were calibrated using a standard quartz sample with known elastic modulus.

Raman Micro-Spectroscopy

An HR-800 Raman spectrophotometer was used, as described (20), to evaluate organic and inorganic matrix composition of mid-tibial cortical bone that was prepared as for AFM. The HR-800 Raman spectrophotometer uses monochromatic radiation emitted by a He-Ne laser (632.8 nm) operating at 20 mW, with a $0.5 \mu\text{m}$ spot size. 2-D maps were created using a computer-controlled translation stage to move the specimen in $1 \mu\text{m}$ increments. Spectra were acquired for the phosphate (PO_4^{3-}) band around 960 cm^{-1} and for the C-H stretching mode (to measure organic content) around 2900 cm^{-1} .

X-ray tomography

X-ray tomography (XTM) studies were based on the work of Kinney (2, 21), adapted to assess the mineral concentration of bone, as described below. Whole tibias were aligned and embedded in epoxy resin as groups to allow direct comparison of wild-type and mutant bones in the same scan. Imaging with the X-ray source from the Advanced Light Source on beamline (8-3-2) at the Lawrence Berkeley National

Laboratory was performed by taking two-dimensional radiographs as the specimens were rotated through 180° in 0.5° increments. The radiographs were reconstructed by Fourier-filtered back projection separated by 11.7 μm. Each of the 1000 reconstructed slices consisted of pixels each with an edge of 11.7 μm. The attenuation coefficient (mm⁻¹) of each pixel is represented by the false colors and relates directly to bone mineral concentration. Cortical bone thickness was derived from 5 cortical distance measurements on each of 10 sections per bone.

Characterization of the Smad3^{+/-} phenotype

X-ray analyses were performed using a Faxitron (Hewlett-Packard model 43805N) as described in (16). Processing of undecalcified bone sections, von Kossa staining, and histomorphometric analyses using a Tektronix system were performed as described (2). Calvarial osteoblast cultures, RNA isolation, Western analyses, and real-time PCR analysis of Runx2 mRNA were performed as described (9, 10). Western analyses were performed using anti-phospho-Smad3/1 from Cell Signaling Technology (#9514) and anti-Smad2/3 from Santa Cruz Biotechnology (FL-425).

Macroscopic mechanical testing

Fracture toughness testing was conducted on isolated femurs. Samples hydrated in HBSS were notched using a razor blade. Testing was conducted in three-point bending (Fig. 5a) with a mechanical testing machine (ELF3200, EnduraTEC, Minnetonka, MN), consistent with ASTM Standard E-399 (22). Samples were loaded to failure in displacement control at room temperature at cross-head displacement rate of 0.01mm/s.

Fracture surfaces were examined using SEM. Fracture toughness, K_{Ic} , values were calculated using the stress-intensity solution for a circumferential through-wall flaw in a cylinder (22, 23).

Sample size and data analysis

All studies were performed on a minimum of three animals. Figures reflect average values of three mice or a representative image. For cellular studies, representative data from repeated experiments is shown. Data were analyzed using one-way ANOVA and post hoc Tukey and LSD multiple comparison tests.

RESULTS

Mouse models of increased and decreased TGF- β signaling

Since regulators of bone matrix properties have not been identified, and TGF- β regulates bone mass and architecture and the expression of bone matrix proteins (6, 14-17), we examined whether TGF- β regulates the material properties of bone matrix. We used transgenic mice with mutations in TGF- β signaling, including D4, D5, DNT β RII, Smad3 $^{+/-}$ and Smad3 $^{-/-}$ mice. D4 and D5 mice express 16- and 2.5-fold increased levels of TGF- β in bone, respectively, under the control of the osteocalcin promoter. D4 bones have more osteoblasts as compared to wild-type mice, reflecting enhanced osteoblast proliferation, but show an age-dependent decrease in volume due to increased bone remodeling (15). The phenotype of D5 bones is similar but less pronounced, consistent with the lower levels of TGF- β expression (15). In contrast, DNT β RII mice, which express

39
M
E
S
S
I
G
E
S
I
I

a “dominant negative” type II TGF- β receptor in osteoblasts, show decreased TGF- β responsiveness in osteoblasts and increased bone volume (16). Smad3^{-/-} mice, which are defective in the expression of Smad3 in all tissues, also have a bone phenotype with an osteopenic reduction in bone volume (14, 17). In addition to the direct role of TGF- β /Smad3 signaling in bone metabolism, some aspects of the Smad3^{-/-} bone phenotype may be due immune, gastrointestinal, or endocrine defects associated with systemic loss of Smad3 expression (24-26). No gross abnormalities have been reported in Smad3^{+/-} mice.

TGF- β regulates the mechanical properties of bone matrix

The regulation of bone matrix properties has largely remained uncharacterized, in part due to experimental inaccessibility. To examine the effect of TGF- β on the mechanical properties of bone matrix, independently of macro-structural variation, we used nanoindentation in combination with AFM (19). A representative AFM image of the cortical bone of a wild-type tibia shows a line of nanoindentations near an osteocyte lacuna (Fig. 1a). The force-displacement curves (Fig. 1b) resulting from nanoindentations were used to calculate the local variations in elastic (Young’s) modulus and hardness (19). The elastic modulus is a measure of stiffness, whereas hardness is a measure of strength, specifically resistance to non-elastic deformation under pressure. Bones from 2 month-old mice with altered TGF- β signaling differed in elastic modulus and hardness of the bone matrix (Fig. 1c), suggesting that TGF- β regulates these properties.

Similar to a previous study (27), the elastic modulus and hardness of tibial bone matrix of wild-type littermates were \sim 20.4 GPa and 0.76 GPa, respectively (Fig. 1d, e).

However, bone matrix from DNT β R11 mice with reduced TGF- β signaling in osteoblasts had significantly increased elastic modulus and hardness (up to 33%), relative to wild-type littermates (Fig. 1d, e). In bone where TGF- β signaling was impaired by ablation of Smad3, the elastic modulus and hardness were also significantly increased (42%). This observation suggests that TGF- β acts through Smad3 to regulate the transcription of genes that, directly or indirectly, control bone matrix composition. The elastic modulus was increased, whether osteoclasts retained (DNT β R11) or had impaired (Smad3 $^{+/-}$, Smad3 $^{-/-}$) TGF- β responsiveness. Reduced TGF- β responsiveness of osteoblasts is, therefore, sufficient to enhance the bone matrix properties. Since bone mass is reduced in Smad3 $^{-/-}$ mice (14, 17) but increased in DNT β R11 mice (16), our results also illustrate that the mechanical properties of bone matrix are independent of macro-structural changes in the tissue. Although previous reports had not differentiated Smad3 $^{+/-}$ from wild-type bone (14, 17), the elastic modulus and hardness of Smad3 $^{+/-}$ bone were as high as the Smad3 $^{-/-}$ bone values. In contrast, D4 and D5 mice with elevated TGF- β signaling had lower elastic modulus and hardness, reduced by 24% and 16%, respectively, compared to wild-type littermates. This effect was TGF- β dosage-dependent, since D5 bone, with 2.5-fold elevated TGF- β expression, showed elastic modulus and hardness values in between those for wild-type and D4 bone with 16-fold elevated TGF- β levels (Fig. 1d, e).

Unlike tibiae that are derived through endochondral replacement of cartilaginous precursors, calvaria develop through intramembranous ossification without cartilaginous intermediates. Similar to results for tibial and femoral bone matrix (data not shown), the elastic modulus and hardness were higher in calvaria with impaired TGF- β signaling, but

lower in bone with elevated TGF- β levels (Fig. 1f, g). This suggests that the effects of TGF- β on bone matrix mechanical properties are independent of TGF- β 's effects on the cartilaginous precursors or the developmental origin of osteoblasts.

To determine if the TGF- β -regulated differences in bone matrix properties were evident prior to mature matrix mineralization, we measured the elastic modulus of neonatal (day 1) cortical tibia bone matrix. Although the elastic modulus was considerably lower in neonatal bone than in the 2 month-old bone, reduced TGF- β signaling already resulted in increased elastic modulus in DNT β RII, Smad3^{+/-} and Smad3^{-/-} bone matrix (Fig. 1h). These data suggest that the mechanical quality of bone matrix is regulated by the developmental level of TGF- β signaling prior to matrix maturation.

Together, these data indicate a direct relationship between the regulation of gene expression by TGF- β and the mechanical properties of bone matrix in bone of endochondral or intramembranous origin. Increased TGF- β causes deposition of a bone matrix with decreased elastic modulus and hardness, whereas reduced TGF- β signaling causes production of a bone matrix with increased elastic modulus and hardness. Despite differences in bone mass, the similarly increased elastic moduli in Smad3^{-/-} and DNT β RII bone show that TGF- β regulates the mechanical properties of bone matrix independently of bone mass and architecture.

Bone matrix heterogeneity in mice with increased TGF- β levels

More detailed measurements of mechanical properties were obtained by elastic-modulus mapping (EMM) (18), using much lower force nanoindentations than in previous

analyses (Fig. 1). In EMM, elastic modulus is measured without plastic deformation of the bone matrix, thereby enabling high-resolution mapping of a “landscape”. This mapping showed no local differences in elastic modulus around lacunae or other physical features. The results are presented in Fig. 2a in a linear color scale, with darker areas corresponding to lower elastic modulus values. In addition, each line of modulus data points can be graphically displayed. Consistent with Fig. 1, EMM showed that impaired TGF- β signaling resulted in higher elastic modulus values, whereas elevated TGF- β signaling reduced elastic modulus values, compared to wild-type bone matrix (Fig. 2a).

EMM also revealed considerable heterogeneity in the local elastic modulus of D4 bone matrix that was not observed in wild-type mice or in any other mouse lines tested (Fig. 2a, 2b). Although 90% of the D4 bone had a reduced elastic modulus, small patches had a modulus that was higher than in wild-type bone. These high local values did not correlate with the location of osteocyte lacunae. To examine if they correlated with matrix composition, we used high-resolution (500 nm) Raman micro-spectroscopy, which maps the mineral (hydroxyapatite) and organic content of bone matrix by measuring peak intensities for PO_4^{3-} at 960 cm^{-1} and C-H stretch at 2900 cm^{-1} (20). This mapping of the composition revealed considerable local heterogeneity in mineral/organic content in the D4 bone matrix. Certain areas had very high mineral and low collagen content, while others had low mineral and normal collagen content. Regions with the highest mineral content had dramatically elevated local elastic modulus values close to 40 GPa. Although the cause remains unknown, this heterogeneity may contribute to the reported tissue-level variability in mineralization (15).

TGF- β signaling regulates bone mineral concentration

We also studied the ability of TGF- β to define the relative mineral concentration in bone matrix using synchrotron x-ray computed tomography (XTM) (21). Unlike micro-CT, XTM uses a monochromatic high-energy x-ray source, and the level of photon absorption correlates directly with the mineral concentration. Elevated TGF- β signaling (D4, D5) resulted in decreased mineral concentration throughout the tibia compared to wild-type bone from 2 month-old mice (Fig. 3a, c). Conversely, reduced TGF- β signaling in DNT β RII or Smad3^{+/-} mice led to increased mineral concentration (Fig. 3a-c), indicating a correlation of the concentration of mineral deposited in the bone matrix with TGF- β signaling. Smad3^{-/-} bone deviated from this relationship, exhibiting reduced mineral concentration compared to wild-type (Fig. 3c).

Our results correlated TGF- β signaling with hardness, elastic modulus and mineral concentration of the bone matrix. Increased TGF- β signaling led to diminished mineral concentration and inferior mechanical properties, whereas decreased TGF- β signaling enhanced these properties (Figs. 1, 3, Table 1). However, Smad3^{-/-} bones showed reduced mineral concentration, even though DNT β RII and Smad3^{+/-} bones had elevated mineral concentration (Fig. 3c). The reported Smad3^{-/-} bone phenotype (14, 17), with its decreased cortical bone thickness and trabecular bone volume also deviated from what was expected based on the D4, D5 and DNT β RII bone phenotypes (15, 16). We hypothesized that this discrepancy was a progressive secondary effect on bone resulting from systemic loss of Smad3. Smad3^{-/-} mice exhibit immune, endocrine, and gastrointestinal defects (24-26) – any of which might affect bone metabolism. To test this hypothesis, XTM was used to

evaluate the mineral concentration of 1 day-old bones when the systemic effects of Smad3 deficiency should as yet be minimal. Prior to birth, the pup acquires nutrients from the maternal-fetal circulation, bypassing the gastrointestinal system, while the neonatal immune and reproductive systems are immature. As shown in Figure 3d, the mineral concentration in neonatal bone was much lower than in mature bone (Fig. 3a, b). Importantly, neonatal Smad3^{-/-} bone, unlike 2 month-old Smad3^{-/-} bone, had increased mineral concentration relative to wild-type littermates (Fig. 3e). The increased mineral concentration (Fig. 3e) and elastic modulus (Fig. 1h) of neonatal Smad3^{-/-} bone was similar to neonatal DNTβRII bone, in which TGF-β receptor signaling is reduced only in osteoblasts. This supports that some properties of the contradictory 2 month-old Smad3^{-/-} bone phenotype are secondary to systemic effects of loss of Smad3. Therefore, prior to complicating systemic effects on the bone matrix, reduced TGF-β signaling in osteoblasts consistently resulted in increased bone matrix mechanical properties and mineral concentration.

Characterization of the Smad3^{+/-} bone phenotype

In the description of the Smad3^{-/-} bone phenotype (14, 17), the Smad3^{+/-} phenotype was presented as similar to wild-type bone. However, our data indicate that Smad3^{+/-} bone matrix differs from wild-type or Smad3^{-/-} bone matrix. We therefore evaluated the mass and architecture of Smad3^{+/-} bones. Consistent with previous reports (14, 17), Smad3^{-/-} femurs had reduced bone mass relative to wild-type femurs when radiographically or histologically assessed (Fig. 4a-d). Surprisingly, Smad3^{+/-} femurs had increased radiodensity relative to wild-type bones (Fig. 4a), reflecting increased mineral

concentration (Fig. 3b) and bone mass (Fig. 4b-d). Thus, Smad3^{+/-} mice possess increased bone mass, while Smad3^{-/-} mice have reduced bone mass. Smad3^{+/-} bones were most similar, in each parameter assessed, to DNTβRII bones, despite the different approaches used to reduce TGF-β/Smad responsiveness. The similarly increased bone mass, mineral concentration and mechanical properties in DNTβRII and Smad3^{+/-} bones stand in contrast to the phenotypes of D4 and D5 bones with increased TGF-β signaling (Table 1). The Smad3^{-/-} bone phenotype likely combines bone-specific, i.e., increased osteoblast apoptosis (14), and progressive secondary effects of systemic Smad3 absence on the bone metabolism and health of the mice as mentioned above (24-26).

To further characterize the reduced TGF-β signaling in Smad3^{+/-} versus wild-type bones, we utilized primary calvarial osteoblasts, cultured from wild-type, Smad3^{+/-}, or Smad3^{-/-} bones. The expression of Smad3 and its activation in response to TGF-β in Smad3^{+/-} osteoblasts were intermediate between wild-type and Smad3^{-/-} cells (Fig. 4e). In Smad3^{+/-} cells, the level of Smad3 phosphorylation in response to 1 ng/ml TGF-β was lower than that of wild-type cells treated with 0.5 ng/ml TGF-β (Fig. 4e). This reduction in Smad3 activation impacted the ability of TGF-β to inhibit osteoblast differentiation, as assessed by the repression of Runx2 mRNA expression (Fig. 4f), alkaline phosphatase activity, and matrix mineralization (data not shown). Therefore, the similarity of the Smad3^{+/-} and DNTβRII bone phenotypes likely results from a comparable reduction in the TGF-β responsiveness of osteoblasts.

Effects of TGF- β on the macro-mechanical properties of bone

The overall quality of bone is determined by bone mass, architecture and bone matrix quality; defects in any of these properties predispose bone to fracture. To investigate the role of TGF- β signaling in the macro-mechanical properties of bone, we subjected femurs to a sharply notched three-point bending test, coupled with scanning electron microscopy of the fracture site (Fig. 5). The notch in the bone initiates fracture in response to imposed bending stresses, leading to crack propagation (22). The resistance to fracture is expressed as the fracture toughness, K_{Ic} , indicating the maximum stress intensity on the bone before initiating fracture from the notch.

Femurs from D4 and D5 mice showed a 31% or 29% decrease in fracture toughness, respectively, relative to wild-type bones (Fig. 5b). Conversely, bones from DNT β RII or Smad3 $^{+/-}$ mice with decreased TGF- β responsiveness, exhibited a 43% and 49% higher fracture toughness relative to wild-type, which is consistent with the increased energy to failure in DNT β RII bone (16). When assessed similarly, 2 month old Smad3 $^{-/-}$ bone had a 30% lower resistance to fracture than wild-type bone (Fig. 5b), consistent with its decreased bone mass (Fig. 4) and bone mineral concentration at this time (Fig. 3). Similar results were obtained for work of fracture (data not shown).

Wild-type, DNT β RII and Smad3 $^{+/-}$ bones exhibited extensive crack deflection, and bone fragments always remained attached after catastrophic fracture (Fig. 5c). Such crack deflection increases the energy needed for fracture, and may improve the toughness. In contrast, D4 and D5 femurs displayed a more perpendicular fracture, little crack deflection, and complete separation of the bone fragments at failure. Smad3 $^{-/-}$ bone showed more crack deflection than D4 and D5 bones, but less than wild-type, DNT β RII, and Smad3 $^{+/-}$

bones, perhaps due to the increased elastic modulus and hardness of the Smad3^{-/-} bone matrix (Fig. 1). These data identify TGF- β signaling as a regulator of fracture resistance and show that reduced TGF- β signaling in DNT β R^{II} and Smad3^{+/-} mice increases resistance to fracture.

DISCUSSION

The properties of bone matrix and their regulation by growth factors have remained largely uncharacterized. Using mice with different levels of TGF- β signaling in osteoblasts, we show that TGF- β is a determinant of the material properties of the bone matrix (Table 1). These findings extend our understanding of the role of TGF- β as a regulator of bone mass (6, 14-17) and indicate a relationship between regulation of gene expression by TGF- β , through Smad3, and the mechanical properties of the bone matrix. TGF- β represents the first cytokine pathway shown to regulate the mechanical properties and composition of bone matrix. We also describe methods to assess bone matrix properties independently of bone mass and architecture. These critical material properties of the bone matrix should be evaluated, in addition to bone mass and architecture, when studying effects of growth factors, hormones, or drugs on bone quality.

Exactly how TGF- β signaling regulates the properties of bone matrix remains to be characterized. The role of Smad3 as a mediator of TGF- β signaling in bone is apparent from the similarity of the DNT β R^{II} and Smad3^{+/-} phenotypes. TGF- β and Smad3 regulate osteoblast gene expression, in part by repressing the function of Runx2 (9, 10), a key transcription factor in osteoblast differentiation. Using this and other transcription

mechanisms, TGF- β /Smad3 regulates the expression of bone matrix proteins such as osteocalcin, osteopontin and collagen I (9, 11), each of which can affect matrix mineralization (13). For example, osteocalcin limits the hydroxyapatite crystal formation, and increases the resistance to bone fracture (13, 28, 29). Thus, the regulation of gene expression in osteoblasts by TGF- β may affect not only the protein composition, but also the material properties of bone matrix.

Although bone matrix properties and their regulators remain largely uncharacterized, natural and experimental mutations in matrix proteins suggest their importance (5, 30). That bone matrix properties are regulated by TGF- β also has significant physiological and clinical implications. While the role of TGF- β in osteoporosis remains unclear, mutations have been identified in the TGF- β gene in osteoporotic patients with normal bone mass (31). TGF- β has been implicated in other pathologies involving bone, including bone metastatic tumors, osteoarthritis, and bone fracture (6, 32). TGF- β levels are elevated at sites of tumor metastasis or bone fracture (6, 32). Although TGF- β is required to initiate fracture repair, elevated TGF- β levels, as in D4 and D5 bone, may compromise the material properties of repaired bone matrix.

Our evidence suggests that the Smad3^{-/-} bone phenotype (14, 17) is a combined result of bone-specific and secondary effects of systemic Smad3 loss. At birth, before activity of the gastrointestinal, endocrine, or immune systems, the mineral concentration of Smad3^{-/-} bone is increased to the same extent as for Smad3^{+/-} and DNT β RII bones (Fig. 3d, e). With maturity, mineral concentration, fracture resistance and bone mass remain elevated in DNT β RII and Smad3^{+/-} bones, but these values drop below wild-type

levels in Smad3^{-/-} bones (Table 1). Together, these observations suggest that the DNT β RII and Smad3^{+/-} phenotypes are more informative of the direct role of TGF- β in bone matrix than the Smad3^{-/-} phenotype. The phenotype of 2 month-old Smad3^{-/-} bone highlights the importance of systemic factors in controlling bone metabolism as well as the primary role of Smad3 in the prevention of premature osteocyte apoptosis and growth plate ossification (14, 17). We conclude that a reduction of TGF- β signaling in bone increases functional parameters of bone quality including bone mass, elastic modulus and hardness, mineral concentration, and resistance to fracture. These properties stand in contrast to the phenotypes of D4 and D5 bone, which express elevated levels of TGF- β (Table 1).

Finally, our results suggest that reduction of TGF- β signaling should perhaps be considered as a therapeutic target to treat bone disorders. This is particularly interesting as TGF- β inhibitors are in preclinical or clinical trials for treatment of cancer metastases (33). The possible effects of these agents on bone-matrix properties should be investigated.

ACKNOWLEDGEMENTS

This research was supported by an Arthritis Foundation Hulda Irene Duggan Arthritis Investigator Award to T.A., NIH grants P60 DE-13058 (Project III) to R.D., RO1 DE015633 to R.K.N and R.O.R., T32 DE07306 to G.B., and P01 DE09859 to M.B., G.W.M., and S.J.M, and was conducted in a facility constructed with support from NCRN grant C06. The Advanced Light Source is supported by the Director, Office of Science, Office of Basic Energy Sciences, of the U.S. Department of Energy under Contract No. DE-AC02-05CH11231. We thank A.P. Tomsia and J.H. Kinney for useful discussions, R.A. Nissenson for critical review of the manuscript, W. Yao and N.E. Lane for assistance with histomorphometry, G. Nomomura for sample preparation, and S. Ho for Raman micro-spectroscopy.

REFERENCES

1. Currey, J. D. (1999) *J Exp Biol* **202**, 2495-503.
2. Lane, N. E., Yao, W., Kinney, J. H., Modin, G., Balooch, M. & Wronski, T. J. (2003) *J Bone Miner Res* **18**, 2105-15.
3. Poli, V., Balena, R., Fattori, E., Markatos, A., Yamamoto, M., Tanaka, H., Ciliberto, G., Rodan, G. A. & Costantini, F. (1994) *EMBO J* **13**, 1189-96.
4. Jamsa, T., Rho, J. Y., Fan, Z., MacKay, C. A., Marks, S. C., Jr. & Tuukkanen, J. (2002) *J Biomech* **35**, 161-5.
5. Misof, K., Landis, W. J., Klaushofer, K. & Fratzl, P. (1997) *J Clin Invest* **100**, 40-5.
6. Alliston, T. N. & Derynck, R. (2000) in *Skeletal Growth Factors*, ed. Canalis, E. (Lippincott Williams & Wilkins, Philadelphia), pp. 233-249.
7. Feng, X. H. & Derynck, R. (2005) *Annu Rev Cell Dev Biol*.
8. ten Dijke, P. & Hill, C. S. (2004) *Trends Biochem Sci* **29**, 265-73.
9. Alliston, T., Choy, L., Ducky, P., Karsenty, G. & Derynck, R. (2001) *EMBO J* **20**, 2254-72.
10. Kang, J. S., Alliston, T., Delston, R. & Derynck, R. (2005) *EMBO J* **24**, 2543-55.

11. Harris, S. E., Bonewald, L. F., Harris, M. A., Sabatini, M., Dallas, S., Feng, J. Q., Ghosh-Choudhury, N., Wozney, J. & Mundy, G. R. (1994) *J Bone Miner Res* **9**, 855-63.
12. Rydziel, S., Varghese, S. & Canalis, E. (1997) *J Cell Physiol* **170**, 145-52.
13. Hunter, G. K., Hauschka, P. V., Poole, A. R., Rosenberg, L. C. & Goldberg, H. A. (1996) *Biochem J* **317**, 59-64.
14. Borton, A. J., Frederick, J. P., Datto, M. B., Wang, X. F. & Weinstein, R. S. (2001) *J Bone Miner Res* **16**, 1754-64.
15. Erlebacher, A. & Derynck, R. (1996) *J Cell Biol* **132**, 195-210.
16. Filvaroff, E., Erlebacher, A., Ye, J., Gitelman, S. E., Lotz, J., Heillman, M. & Derynck, R. (1999) *Development* **126**, 4267-79.
17. Yang, X., Chen, L., Xu, X., Li, C., Huang, C. & Deng, C. X. (2001) *J Cell Biol* **153**, 35-46.
18. Balooch, G., Marshall, G. W., Marshall, S. J., Warren, O. L., Asif, S. A. & Balooch, M. (2004) *J Biomech* **37**, 1223-32.
19. Oliver, W. C. & Pharr, G. M. (2004) *J Mater Res* **19**, 3-20.
20. Schulze, K. A., Balooch, M., Balooch, G., Marshall, G. W. & Marshall, S. J. (2004) *J Biomed Mater Res* **69A**, 286-93.

21. Kinney, J. H., Haupt, D. L., Balooch, M., Ladd, A. J., Ryaby, J. T. & Lane, N. E. (2000) *J Bone Miner Res* **15**, 1981-91.
22. Anderson, T. (1994) *Fracture Mechanics: Fundamentals and Applications*, 2nd ed. (CRC Press, Boca Raton, FL).
23. Zahoor, A. (1989) in *Ductile Fracture Handbook* (EPRI, Palo Alto, CA) Report No. NP-6301.
24. Ashcroft, G. S., Yang, X., Glick, A. B., Weinstein, M., Letterio, J. L., Mizel, D. E., Anzano, M., Greenwell-Wild, T., Wahl, S. M., Deng, C. & Roberts, A. B. (1999) *Nat Cell Biol* **1**, 260-6.
25. Zhu, Y., Richardson, J. A., Parada, L. F. & Graff, J. M. (1998) *Cell* **94**, 703-14.
26. Tomic, D., Miller, K. P., Kenny, H. A., Woodruff, T. K., Hoyer, P. & Flaws, J. A. (2004) *Mol Endocrinol* **18**, 2224-40.
27. Turner, C. H., Rho, J., Takano, Y., Tsui, T. Y. & Pharr, G. M. (1999) *J. Biomech* **32**, 437-441.
28. Ducey, P., Desbois, C., Boyce, B., Pinero, G., Story, B., Dunstan, C., Smith, E., Bonadio, J., Goldstein, S., Gundberg, C., Bradley, A. & Karsenty, G. (1996) *Nature* **382**, 448-52.
29. Roy, M. E., Nishimoto, S. K., Rho, J. Y., Bhattacharya, S. K., Lin, J. S. & Pharr, G. M. (2001) *J Biomed Mater Res* **54**, 547-553.

30. Fong, H., White, S. N., Paine, M. L., Luo, W., Snead, M. L. & Sarikaya, M. (2003) *J Bone Miner Res* **18**, 2052-9.
31. Langdahl, B. L., Knudsen, J. Y., Jensen, H. K., Gregersen, N. & Eriksen, E. F. (1997) *Bone* **20**, 289-94.
32. Guise, T. A. & Chirgwin, J. M. (2003) *Clin Orthop Relat Res*, S32-8.
33. Dumont, N. & Arteaga, C. L. (2003) *Cancer Cell* **3**, 531-6.

Tables

Table 1

Mouse Line	D4	D5	WT	DNT β R11	Smad3+/-	Smad3-/- 1 day	Smad3-/- 8 weeks
TGF- β Signaling							
Elastic Modulus & Hardness							
Bone Mineral Concentration							
Fracture Toughness						NS	
Bone Mass	¹⁴	¹⁴		¹⁵		NS	^{16,17}

NS= not studied, ¹⁴⁻¹⁷Refer to previous work cited in References

Figures and Captions

Figure 1

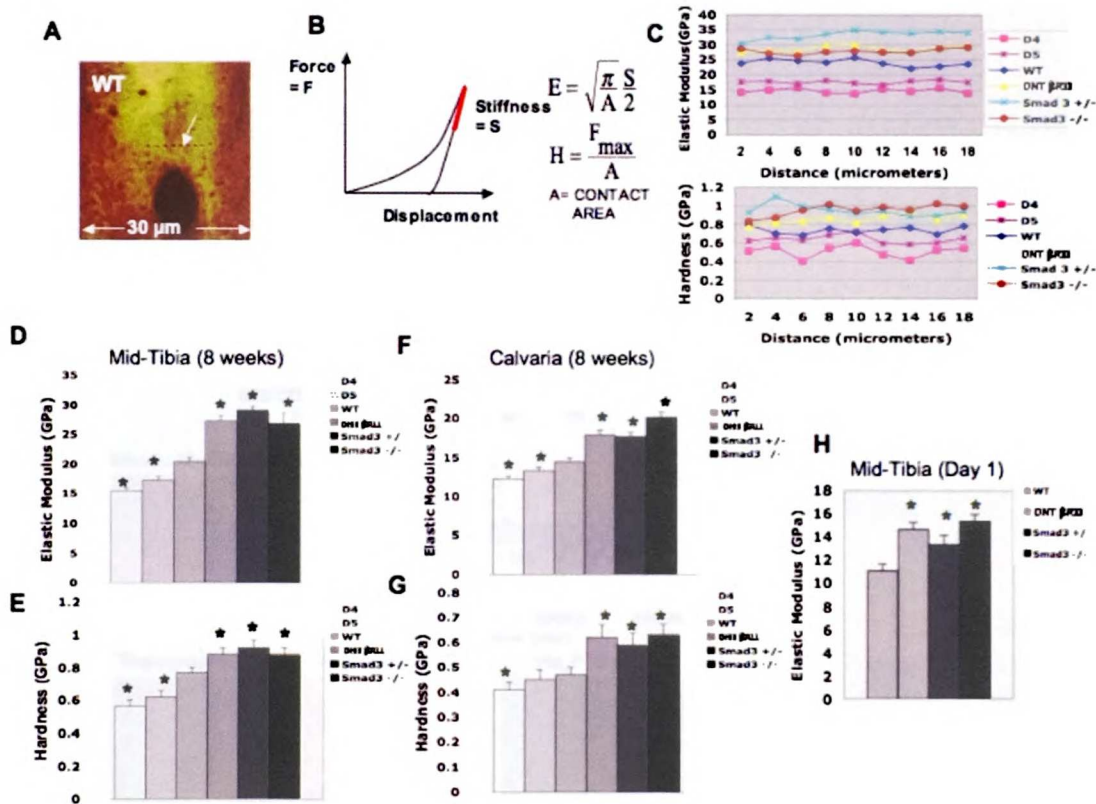


Figure 1. TGF- β signaling regulates the mechanical properties of bone matrix. (A) AFM topography shows a line of nine nanoindentations (white arrow) near an osteocyte lacuna in bone. (B) Force displacement curves were used to calculate the elastic modulus, E (derived from the stiffness, S) and hardness, H . (C) Individual elastic modulus (top panel) and hardness (bottom panel) values are for one line of consecutive nanoindentations in bone of each genotype. Bones from 2 month-old animals with elevated TGF- β signaling (D4 and D5 mice) had decreased elastic modulus (D, F) and hardness (E, G). Two month (D-G) and neonatal (H) bones with impaired TGF- β signaling (DNT β R2, Smad3 $^{+/-}$, and Smad3 $^{-/-}$ mice) had increased elastic modulus and hardness. (D), (E), and (H) show values for bone of endochondral origin (tibiae), whereas (F) and (G) show values for calvarial bones. Error bars show standard deviation and stars indicate values that are significantly different from wild-type values ($p < 0.001$).

Figure 2

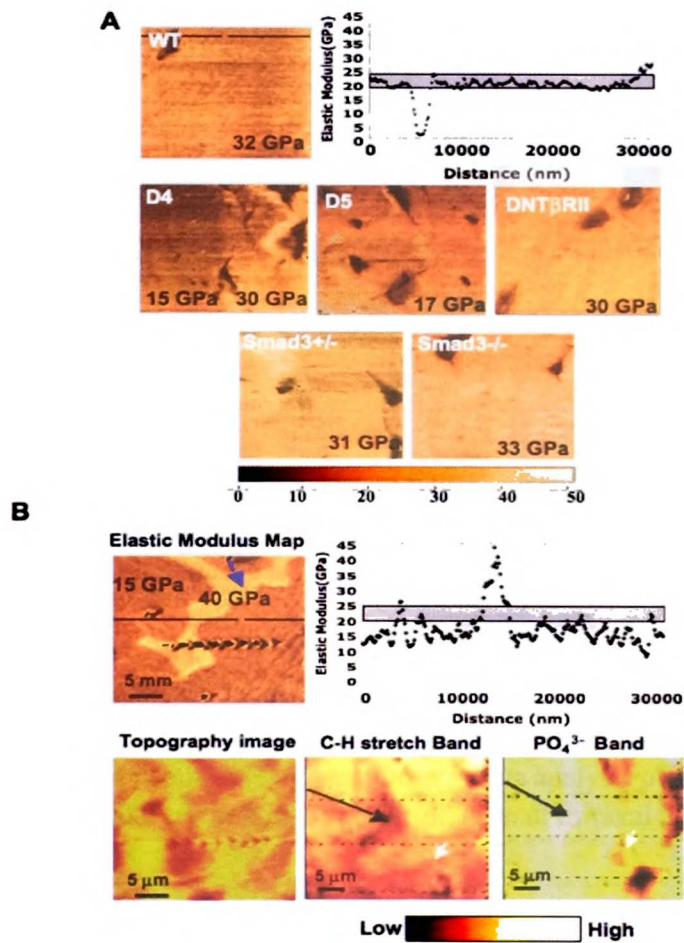


Figure 2. Mapping of the mechanical properties and composition of bone matrix reveals local variation in D4 bone matrix. (A) EMM was performed on mid-tibial cortical bone for each genotype. Representative maps show the elastic modulus in a color gradient throughout the 30 x 30 μm² area. A graphic representation shows the 256 modulus data points corresponding to the black line in the map. Values drop at the site of an osteocyte lacuna. The average range of wild-type values is shown on the graph (gray bar), and average values are indicated on the maps. Only D4 matrix exhibited heterogeneity. (B) Evaluation of the same region of D4 bone matrix by EMM and AFM topography imaging revealed heterogeneous areas of elastic modulus ranging from 10 to 40 GPa (blue arrow on map) that did not correspond to topographical variation. “Placemaker” indents were applied to allow assessment of the same region using Raman micro-spectroscopy. Modulus variability correlated with heterogeneity of the collagen (C-H stretch band) or hydroxyapatite (PO₄³⁻ band) composition, as determined using Raman micro-spectroscopy, and is indicative of defects in inorganic/organic content in D4 bone matrix. Lighter colors represent higher Raman peaks while darker colors indicate lower peaks. Areas with high mineral and low collagen content (black arrow) had increased elastic modulus, while elastic modulus

Figure 4

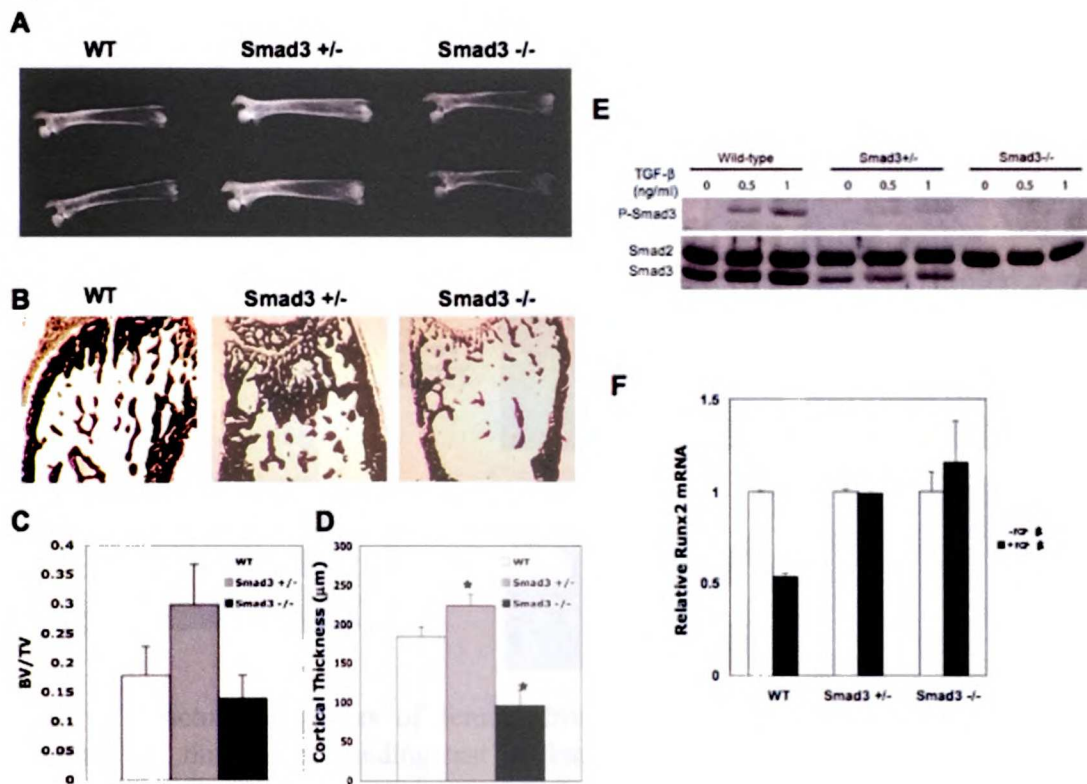


Figure 4. Increased bone mass in Smad3^{+/-} mice with reduced osteoblast TGF- β responsiveness. X-ray analysis of femurs (A) and histomorphometry of von Kossa stained tibiae (B) revealed increased radiodensity, trabecular bone volume and cortical bone thickness in Smad3^{+/-} bone, relative to wild-type and Smad3^{-/-} bone. (C) represents the relative bone volume over total volume, as determined by histomorphometry analysis, and (D) shows differences in cortical bone thickness, as determined by XTM ($p < 0.001$). (E) Western analysis shows Smad2 and Smad3 expression and phospho-Smad3 (P-Smad3) in calvarial osteoblasts from wild-type, Smad3^{+/-} and Smad3^{-/-} mice. Cells were treated with the indicated dose of TGF- β following 6 h of serum starvation. (F) Real-time PCR analysis of Runx2 mRNA expression in calvarial osteoblasts in the absence or presence of 1ng/ml TGF- β . Values are normalized to RPL19 expression and are shown relative to untreated cells of the same genotype.

Figure 5

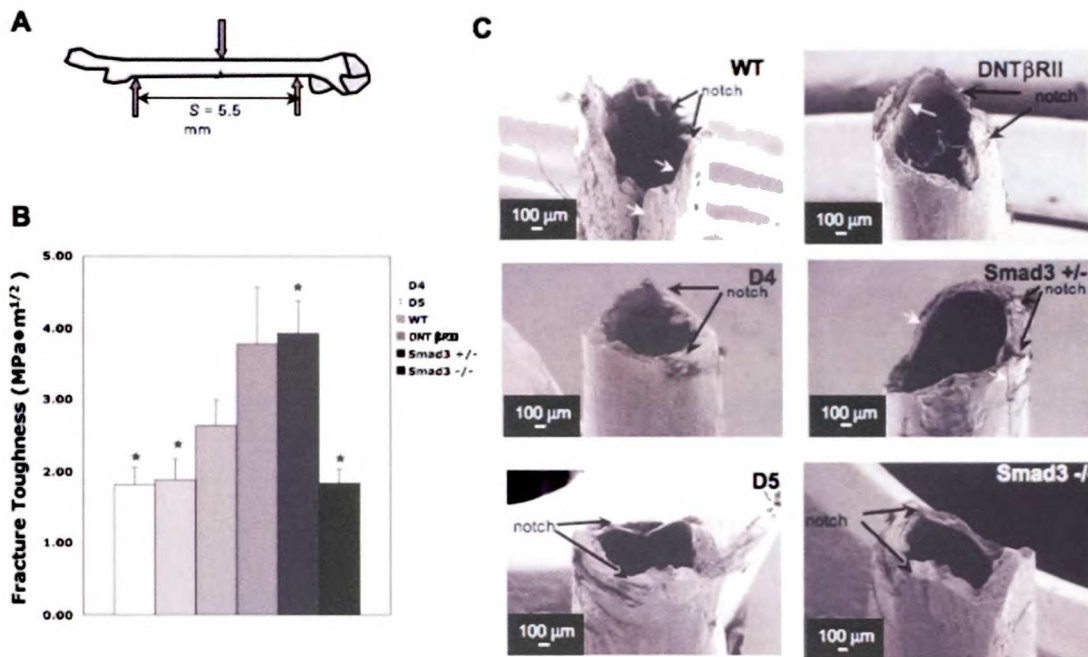


Figure 5. Fracture toughness of femurs from mice with different levels of TGF- β signaling. A three-point bending test of femurs, where fracture was initiated from a sharpened notch (A), was used to measure the fracture toughness of bone, K_c (B). Elevated TGF- β signaling (D4, D5) decreased while reduced TGF- β signaling (DNT β RII, Smad3 $^{+/-}$) increased K_c compared to wild-type bone (* = $p < 0.05$). (C) As shown by SEM, fracture resistant DNT β RII and Smad3 $^{+/-}$ bones exhibited extensive crack deflection (white arrows), whereas perpendicular fractures were observed in D4, D5, and Smad3 $^{-/-}$ bones. The location of the initiating notch is indicated.

Chapter 6

Discussion, Conclusion, and Future Work

Discussion and Conclusion

In this thesis work, we have investigated the local mechanical properties and composition of both teeth and bone. In teeth, we accurately assessed the properties of the dentin-enamel junction and cementum-dentin junction by investigating both local mechanical and chemical properties of the junctions and found that previous measurements were probe-size and load dependant. In bone, we found that TGF- β and Glucocorticoids both regulate local mechanical properties and composition of bone matrix, which in turn influence the fracture toughness.

In Chapter 2, we utilized high resolution Raman micro-spectroscopy to investigate the cementum-dentin and dentin-enamel junctions. As a result of this study, we found that although no Raman peak shifts were detected in the PO_4^{3-} (inorganic phase), the C-H stretching mode (organic phase) revealed significant Raman peak shifts (4.6 cm^{-1}) between dentin, the DEJ, and enamel. In addition, the DEJ width was measured using both the PO_4^{3-} mode as well as the C-H stretching mode and was found to be in close agreement with previous nanoindentation studies. The most interesting finding is that the DEJ and the CDJ are zones of chemical transition rather than separate phases. The presence of organic peak shifts between dentin and enamel is not surprising because in dentin the organic component is primarily collagen type I molecules while in enamel it is other non-collagenous proteins.

In Chapter 3, we applied Elastic Modulus Mapping, a high spatial resolution ($\sim 15 \text{ nm}$) AFM-based technique, to study the DEJ in dry conditions. Since the technique allows elastic modulus determination without permanent indentation, the results are more likely to be independent of probe size, which has been shown to be a problem with other

techniques. We found that the DEJ width was approximately 2-3 μm , significantly lower than previously reported. In addition, because of the high spatial resolution of our Elastic Modulus Mapping technique, the quantitative characteristics of the peritubular-intertubular junction (PIJ) were elucidated in human dentin for the first time. We found the PIJ width to be 1-2 μm . These studies led to new discoveries of the properties of the DEJ and PIJ in the tooth and the importance of eliminating probe-size dependency to accurately assess local variation of mechanical properties at the nanometer level in small areas of calcified tissues.

In Chapters 4 and 5, we utilized several high-resolution bioengineering techniques to investigate the effect of growth factor/hormone signaling on bone mechanical properties. In Chapter 4, we studied the effect of glucocorticoid (GC) treatment in mice on local bone mechanical properties and matrix composition. Glucocorticoids are frequently prescribed for many inflammatory conditions including arthritis, pulmonary diseases as well as skin conditions. While they are potent anti-inflammatory agents, chronic use results in a number of adverse side effects, the most common being osteoporosis. While patients on GC-treatment have elevated bone fragility, the mechanism by which this occurs is still not well understood. Because GC's have been shown to effect osteoblasts and osteoclasts in vitro, we hypothesized that GC's regulate localized bone matrix mechanical properties, in addition to its known effect on macro-scale architecture.

To determine the effect of GC-treatment on localized mechanical properties, we studied trabecular bone from 2-month old mice treated with GC's (GC) compared to mice treated with placebo (PL), as well as ovariectomized estrogen-deficient mice (OVX)

compared to Sham-operated controls (Sham). Using Elastic Modulus Mapping, we found a localized reduction in elastic modulus surrounding the osteocyte lacunae in GC-treated mouse trabecular bone not seen in PL treated mice. Furthermore, this “halo” of reduced modulus surrounding the osteocyte lacunae, seen in GC mice, was coupled with reduced inorganic/organic ratio assessed by Raman micro-spectroscopy. Therefore, in addition to reduced modulus, there was reduced mineral concentration surrounding the osteocyte lacunae in GC-treated mice. GC-treated mice were then compared to OVX and Sham-operated controls. GC and OVX mice showed a reduction in whole bone strength compared to Placebo (GC control) and Sham-operated controls (OVX control); however, the reduction in modulus and inorganic/organic ratio seen in GC-mice was not seen in OVX mice or controls. This indicates that although both GC mice and OVX mice show reduced strength, only GC’s regulate local mechanical properties and inorganic/organic ratio and these localized changes may play an additional role in determining fracture severity in response to GC-treatment. We believe these localized changes in GC-treated mouse trabecular bone plays an important role in overall bone fragility. Whether there are localized changes in mechanical properties of bone from patients on GC’s is still unknown.

In Chapter 5, we studied the effect of TGF- β signaling on mechanical properties and composition of bone matrix. Utilizing six different mouse models with altered levels of TGF- β in bone, we found that TGF- β regulates local mechanical properties and mineralization of bone independent of its effects on macro-scale bone architecture. Nanoindentation studies revealed that partial reduction in TGF- β signaling (Smad3^{+/-} and E1 mice), led to an increase in elastic modulus and hardness in calvarial bone as well

S

1921
1922
1923
1924
1925
1926
1927
1928
1929
1930
1931
1932
1933
1934
1935
1936
1937
1938
1939
1940
1941
1942
1943
1944
1945
1946
1947
1948
1949
1950
1951
1952
1953
1954
1955
1956
1957
1958
1959
1960
1961
1962
1963
1964
1965
1966
1967
1968
1969
1970
1971
1972
1973
1974
1975
1976
1977
1978
1979
1980
1981
1982
1983
1984
1985
1986
1987
1988
1989
1990
1991
1992
1993
1994
1995
1996
1997
1998
1999
2000
2001
2002
2003
2004
2005
2006
2007
2008
2009
2010
2011
2012
2013
2014
2015
2016
2017
2018
2019
2020
2021
2022
2023
2024
2025
2026
2027
2028
2029
2030
2031
2032
2033
2034
2035
2036
2037
2038
2039
2040
2041
2042
2043
2044
2045
2046
2047
2048
2049
2050
2051
2052
2053
2054
2055
2056
2057
2058
2059
2060
2061
2062
2063
2064
2065
2066
2067
2068
2069
2070
2071
2072
2073
2074
2075
2076
2077
2078
2079
2080
2081
2082
2083
2084
2085
2086
2087
2088
2089
2090
2091
2092
2093
2094
2095
2096
2097
2098
2099
2100

sco

as long bone, while elevated levels of TGF- β signaling (D4 and D5 mice) led to an opposite phenotype. Using Elastic Modulus Mapping, we found that mice with 16-fold elevated levels of TGF- β signaling (D4 mice) showed nanometer localized heterogeneity of mechanical properties not seen in any other mouse.

Synchrotron x-ray tomography and 3-point bending revealed that partial reduction of TGF- β signaling in Smad3^{+/-} mice and mice with the dominant negative TGF- β receptor (E1 mice) led to increased mineral concentration and fracture toughness; however, complete loss of Smad3 (Smad3^{-/-} mice) led to an opposite phenotype with reduced fracture toughness and mineral concentration. This was a surprising result, as based on the other mouse lines, it would be expected that complete ablation of smad3 would lead to increased fracture toughness and mineral concentration. We hypothesized that this discrepancy was a progressive secondary effect on bone resulting from systemic loss of Smad3. As discussed in Chapter 5, Smad3^{-/-} mice exhibit immune, endocrine, and gastrointestinal defects any of which might affect bone metabolism. To test this hypothesis, XTM was used to evaluate the mineral concentration of 1 day-old bones when the systemic effects of Smad3 deficiency should as yet be minimal. Prior to birth, the pup acquires nutrients from the maternal-fetal circulation, bypassing the gastrointestinal system, while the neonatal immune and reproductive systems are immature. By testing neonatal smad3^{-/-} bone for mineral concentration using XTM, we found that the mineral concentration of Smad3^{-/-} bone is increased to the same extent as for Smad3^{+/-} and DNT β R^{II} bones. With maturity, mineral concentration, fracture resistance and bone mass remain elevated in DNT β R^{II} and Smad3^{+/-} bones, but these values drop below wild-type levels in Smad3^{-/-} bones. Together, these observations

8
M
E
S
S
A
G
E
S
I
N
T
H
E
S
E
S
E
S
I
O
N
S

suggest that the DNT β RII and Smad3 $^{+/-}$ phenotypes are more informative of the direct role of TGF- β in bone matrix than the Smad3 $^{-/-}$ phenotype. The phenotype of 2 month-old Smad3 $^{-/-}$ bone highlights the importance of systemic factors in controlling bone metabolism as well as the primary role of Smad3 in the prevention of premature osteocyte apoptosis and growth plate ossification.

Based on the results from Chapter 5, the importance of studying more than one property was evident, as the discrepancy in the phenotypes of the 8-week-old Smad3 $^{+/-}$ and Smad3 $^{-/-}$ mice would not have been observed if only nanoindentation tests were conducted. The elevated modulus and reduced fracture toughness seen in Smad3 $^{-/-}$ mice needs to be studied further; however, it should be noted that the linear increase in modulus of a two-phase composite with increasing fraction of the stiffer (in this case, mineral) phase represents a first-order rule-of-mixtures model of composite behavior. In reality, other factors such as the orientation and distribution of the stiffer (mineral) phase and its bonding to the matrix are additional factors that can play an important role. We can only presume here that the organization of the crystal mineral phase is sufficiently altered in the Smad3 $^{-/-}$ mice to cause this change in stiffness.

The investigation of overall bone matrix mechanical properties in GC-mice and TGF- β signaling mice led to new discoveries on how growth factor/hormone signaling can regulate nanometer scale mechanical properties and composition that play key roles in determining bone fracture under load. Traditional macro-bone strength and bone architecture tests will always be important in understanding bone fragility; however, our studies have shown that localized mechanical properties and composition of bone matrix can also play key roles in determining how bone responds under load. Furthermore, while

nanometer scale mechanical properties and composition of bone matrix in genetically modified mouse bone has not been assessed in great detail in the bone community, its clinical relevance and its influence on bone fragility are highly apparent from these studies.

Shortcomings

In this thesis, we used state of the art technology to measure localized material properties of trabecular bone, cortical bone, and teeth. However, there are also a number of shortcomings. In Chapters 2 and 3, our assessment of the DEJ width was determined by estimating where the junction began and ended based on our micro-Raman spectroscopy, nanoindentation, and Elastic Modulus Mapping results. However, future studies should be done to mathematically model where the junction begins which would provide an improved estimate of the DEJ width. Furthermore, in chapter 3, all dynamic stiffness mapping measurements were done in dry conditions; however, future studies should be done under wet conditions, since these conditions are closer to physiological conditions. In addition, although dry values are usually a few GPa higher than wet values, in some conditions such as Dentinogenesis Imperfecta type II, a genetic defect in teeth, the wet values are much lower than dry values and reflect differences in the intrafibrillar and extrafibrillar components of the tissue (1). The possibilities of such alterations could not be discerned in the present work.

In Chapter 4, we studied only one dose of GCs and one time point, so we cannot generalize about dose response or time of exposure. In addition, it is not clear whether these changes persist, or whether remineralization occurs after cessation of GC

8
M
E
M
O
R
I
S
S

administration. These issues should be addressed in future experiments. Nevertheless, our observation that there are focal changes in tissue properties within the trabeculae, which would increase bone fragility, is consistent with clinical observations in which some patients treated with glucocorticoids suffer fractures at higher bone mineral density values than in postmenopausal women. Lastly, we performed our experiments on both male and female mice. Since Glucocorticoid-induced osteoporosis has been well validated in the male mouse model at 6 months of age and OVX mice are female, we chose to use both male and female mice. However, we do not think that the sex difference compromised our findings because both groups lost similar amounts of trabecular bone mass and whole bone strength during the 21 day experiment and the differences we observed in the changes in elastic modulus and mineralization around the osteocyte in prednisolone-treated animals was not seen in any of the other three experimental groups.

In Chapter 5, one shortcoming was the fact that we did not address the issue of bone turnover. It is known that TGF- β affects osteoblast proliferation, differentiation, and mineralization; therefore, changing levels of TGF- β will affect bone turnover. However, we feel that this affect is minimal as we are measuring the local mechanical properties of the bone matrix laid down by the osteoblast and our results are focusing on osteoblast-specific actions and not that of the osteoclast. Nevertheless, further studies should be done to determine the affect bone turnover has on local mechanical properties of bone matrix. This study also focused mainly on the effect of TGF- β on cortical bone and not much work was done in investigating the trabecular region; therefore, trabecular bone should be addressed in future studies.

In Chapter 5, one of our shortcomings was the fact that we did not address the issue of bone turnover. It is known that TGF- β affects osteoblast proliferation, differentiation, and mineralization; and therefore, changing levels of TGF- β will affect bone turnover. However, we feel that this affect is minimal as we are measuring the local mechanical properties of the bone matrix laid down by the osteoblast and our results are focusing on osteoblast-specific actions and not that of the osteoclast. Nevertheless, further studies should be done to determine the affect bone turnover has on local mechanical properties of bone matrix. This study was also mainly focusing on the effect of TGF- β on cortical bone and not much work was done in investigating the trabecular region; therefore, this will be addressed in future studies.

Future Work

Effect of concurrent Risedronate treatment on bone matrix properties of glucocorticoid-induced osteoporotic mice

As described in Chapter 4 and noted in the summary above, glucocorticoids are frequently prescribed for many inflammatory conditions including arthritis, pulmonary diseases, and skin conditions. Chronic use often results in a number of adverse side effects, the most common being osteoporosis. Glucocorticoid-induced osteoporosis (GIOP) commonly results from suppression of bone formation and enhancement of bone resorption, which alters bone structure and induces bone fragility (2-4). Bisphosphonates, acting as anti-resorptive agents, are effective therapies and are widely used for metabolic bone diseases, such as GIOP, Paget's disease, and estrogen-deficiency bone loss (5-8). Furthermore, bisphosphonate therapy can reduce the risk of new vertebral fracture in both

estrogen-deficiency as well as GIOP; however, the mechanism by which they increase bone strength and reduce vertebral fracture risk is still unclear.

Risedronate, one such bisphosphonate, has been shown to reduce the risk of vertebral and non-vertebral fractures (6). Although bone mineral density (BMD) increases with Risedronate treatment, the increased BMD only explains a small percentage of the reduction in vertebral fracture risk (8). Furthermore, Risedronate treatment leads to maximal BMD after approximately three years of treatment while decreased vertebral fracture risk is observed within the first year of treatment (9-11). This suggests that in addition to whole bone density, Risedronate may be regulating other bone matrix properties, studied in Chapters 4 and 5, that can ultimately influence bone fragility (12, 13).

Risedronate, like other amino-bisphosphonates, has been reported to have effects on many aspects of bone metabolism, including acting directly on osteoclasts through isoprenoid biosynthesis and protein prenylation (14, 15) as well as caspase cleavage of Mst1 kinase (16), ultimately leading to inhibition of bone resorption and osteoclast apoptosis (11, 12). Furthermore, Risedronate, as well as other bisphosphonates such as alendronate and ibandronate, have been shown to bind and inhibit hydroxyapatite (HAP) crystal growth (17); it is also known to be more potent in promoting surface HAP nucleation than other known bisphosphonates (17). Risedronate has also been recently shown to increase expression of osteoblast markers such as Runx2 and Collagen Type I leading to enhanced osteoblast proliferation and initial differentiation (18). Presumably, the role of Risedronate in binding and regulating HAP nucleation and osteoblast and

osteoclast activity suggests that it will most likely play an important role in regulating the local mechanical properties of the bone matrix.

In Chapter 4, we found that glucocorticoid (GC) treatment in mice leads to increased osteocyte lacunae size, a hypomineralized zone surrounding the osteocyte lacunae, as well as local changes in mechanical properties surrounding the osteocyte lacunae. Whether concurrent treatment with Risedronate in GC-treated mice can rescue this phenotype and whether these changes occur in GC-treated patients, are still unknown; however, it may be quite important in determining the overall resistance to bone fracture in patients with bone metabolic diseases. Following methods similar to those in Chapters 4 and 5, experiments should be conducted using Risedronate in GC-treated mice to determine changes in local and macroscopic bone properties. This would give further insight into how Risedronate regulates bone properties and further establish its efficacy in treating bone metabolic diseases.

TGF- β chemical inhibitors

As shown in Chapter 5 in this thesis work, partial reduction of TGF- β signaling in mice leads to an increase in bone matrix mechanical properties, degree of mineralization, and fracture toughness. Therefore, in addition to anticancer therapeutic benefits of TGF- β inhibitors as suggested in previous studies (19, 21, 21), reduction in TGF- β signaling may lead to possible therapeutic benefits in other bone-related diseases as well.

Recent literature suggests that inhibition of autocrine and paracrine TGF- β in tumors can delay metastasis by affecting motility, angiogenesis, stroma formation and remodeling, and immunosuppression (19). In addition, recently it has been shown that

mice expressing soluble TGF β RII under regulation of the MMTV/LTR promoter exhibit high TGF- β -antagonists. In addition these mice do not exhibit severe inflammatory response as seen in TGF- β knockout mice, indicating an anti-toxicity advantage with chemical inhibitors (20). However, the use of TGF- β inhibitors in treatment of bone diseases is still not well understood. Numerous strategies for TGF- β inhibition are currently in development, including TGF- β ligand blocking through antibodies and the use of recombinant fusion proteins containing the ectodomains of TGF- β RII, as well as the use of ATP competitive inhibitors, SBI-43152 (GlaxoSmithKline), NPC-30345 and SD-208 (SCIOS Inc.), and LY-364947 (Lilly Research) aimed at directly blocking the catalytic activity of the TGF- β I receptor. SB-43152 has been studied extensively *in vitro* and has been shown to antagonize the proliferation of cancer cells (19, 20, 21, 22). SB-43152 has also been shown recently to induce osteoblast differentiation and alkaline phosphatase activity in human mesenchymal stem cells (hMSCs) (23). In addition, SD-208 has been shown to inhibit growth and invasiveness of murine and human glioma cells *in vitro* and *in vivo* (24-27). Therefore, the use of chemical TGF- β inhibitors can be adapted for the study of bone matrix development *in vivo* as it has been already adapted for cancer treatment. The investigation of the effects of partially inhibiting TGF- β signaling by chemical inhibitors and the related changes in bone matrix mechanical properties and fracture toughness may lead to important discoveries on how TGF- β inhibitors can possibly be used as therapeutic interventions to bone diseases. This can be done by comparing the bone matrix mechanical properties of mice treated with TGF- β inhibitors and mice treated with vehicle.

8
K
R
E
D
I
T
S
I
N
T
E
R
N
A
T
I
O
N
A
L
S
E
M
I
N
A
R
Y

References

1. Kinney JH, Habelitz S, Marshall SJ, Marshall GW. The importance of intrafibrillar mineralization of collagen on the mechanical properties of dentin. *J Dent Res* 2003 82: 957-961.
2. Saag K. G. Glucocorticoid-induced Osteoporosis *Endocrinol Metab Clin North Am*. Mar; 32 (1):135-57, vii. (2003)
3. Cooper C., Coupland C., Mitchell M., Rheumatoid arthritis, corticosteroid therapy and hip fracture. *Ann. Rheum. Dis.* Jan; 54 (1): 49-52. (1995)
4. Lane N. E. An update on glucocorticoid-induced osteoporosis. *Rheum Dis Clin North Am* Feb; 27 (1):235-53 (2001)
5. Delaney M. F., Hurwitz S., Shaw J., LeBoff M. S. Bone density changes once weekly with risedronate in postmenopausal women *J Clin Densitom.* Spring; 6 (1): 45-50 (2003)
6. Saag K. G. et al. Alendronate for the prevention and treatment of glucocorticoid induced osteoporosis. Glucocorticoid-induced osteoporosis intervention study group. *N Engl J Med* Jul 30; 339 (5): 292-9 (1998)
7. Eastell R. et al. Relationship of early changes in bone resorption to the reduction in fracture risk with risedronate. *J Bone Miner Res.* Jun; 18 (6): 1051-6 (2003)
8. Bauer D. C. et al. Change in bone turnover and hip, non-spine, and vertebral fracture in alendronate-treated women: the fracture intervention trial. *J Bone Miner Res.* Aug; 19 (8): 1250-8 (2004)

9. Watts, N. B. Focus on primary care postmenopausal osteoporosis: an update. *Obstet Gynecol Surv.* Dec; (55): S49-55 (2000)
10. Ettinger B. et al. Reduction of vertebral fracture risk in postmenopausal women with osteoporosis treated with raloxifene: results from a 3-year randomized clinical trial. Multiple outcomes of raloxifene evaluation (MORE) investigators. *JAMA* Aug 18; 282 (7): 637-45 (1999)
11. Van Staa T. P., Laan R. F., Barton I. P., Cohen S., Reid D. M., & Cooper C. Bone density threshold and other predictors of vertebral fracture in patients receiving oral glucocorticoid therapy *Arthritis Rheum.* Nov; 48 (11): 3224-9 (2003).
12. Wallach S. et al. Effects of risedronate treatment on bone density and vertebral fracture in patients on corticosteroid therapy. *Calcif Tissue Int.* Oct; 67 (4): 277-85 (2000).
13. Borah B., Dufresne T. E., Chmielewski P. A., Johnson T. D., Chines A., Manhart M. D. Risedronate preserves bone architecture in postmenopausal women with osteoporosis as measured by three-dimensional microcomputed tomography. *Bone* Apr; 34 (4): 734-46. (2004)
14. Borah B., Ritman E. L., Dufresne T. E., Jorgensen S. M., Liu S., Sacha J., Phipps R. J., Turner R. T. The effect of risedronate on bone mineralization as measured by micro-computed tomography with synchrotron radiation: correlation to hisomorphometric indices of turnover. *Bone* Jul; 37 (1): 1-9 (2005)
15. Luckman S. P., Hughes D. E., Coxon F. P., Graham R., Russell G., Rogers M. J. Nitrogen-containing bisphosphonates inhibit the mevalonate pathway and prevent

- post-translational protein prenylation of GTP-binding proteins, including Ras. *J Bone Miner Res.* Apr; 13 (4): 581-9 (1998).
16. Coxon F. P., Helfrich M. H., Van't Hof R., Sebti S., Ralston S. H., Hamilton A., Rogers M. J. Protein geranylgeranylation is required for osteoclast formation, function, and survival: inhibition by bisphosphonates and GGTI-298.
 17. Reska, A. A., Halasy-Nagy J. M., Masarachia P. J., Rodan G. A. Bisphosphonates act directly on the osteoclast to induce caspase cleavage of mst1 kinase during apoptosis. A link between inhibition of the mevalonate pathway and regulation of an apoptosis-promoting kinase. *J Biol Chem* Dec 3; 274 (49): 34967-73 (1999).
 18. Nancollas G. H., Tang R., Phipps R. J., Henneman Z., Gulde S., Wu W., Mangood A., Russell R. G., Ebetino F. H. Novel insights into actions of bisphosphonates on bone: Differences in interactions with hydroxyapatite. *Bone* Jul 19 (2005)
 19. von Knoch F., Jaquier C., Kowalsky M., Schaeren S., Alabre C., Martin I., Rubash H. E., Shanbhag A. S. Effects of bisphosphonates on proliferation and osteoblast differentiation of human bone marrow stromal cells. *Biomaterials* Dec; 26 (34): 6941-9 (2005)
 20. Dumont N, Arteaga CL 2003 Targeting the TGF beta signaling network in human neoplasia. *Cancer Cell* 3(6):531-6.
 21. Mori Y, Ishida W, Bhattacharyya S, Li Y, Platanias LC, Varga J 2004 Selective inhibition of activin receptor-like kinase 5 signaling blocks profibrotic transforming growth factor beta responses in skin fibroblasts. *Arthritis Rheum* 50(12):4008-21.

22. Hjelmeland MD, Hjelmeland AB, Sathornsumetee S, Reese ED, Herbstreith MH, Laping NJ, Friedman HS, Bigner DD, Wang XF, Rich JN 2004 SB-431542, a small molecule transforming growth factor-beta-receptor antagonist, inhibits human glioma cell line proliferation and motility. *Mol Cancer Ther* **3**(6):737-45.
23. Inman GJ, Nicolas FJ, Callahan JF, Harling JD, Gaster LM, Reith AD, Laping NJ, Hill CS 2002 SB-431542 is a potent and specific inhibitor of transforming growth factor-beta superfamily type I activin receptor-like kinase (ALK) receptors ALK4, ALK5, and ALK7. *Mol Pharmacol* **62**(1):65-74.
24. Maeda S, Hayashi M, Komiya S, Imamura T, Miyazono K 2004 Endogenous TGF-beta signaling suppresses maturation of osteoblastic mesenchymal cells. *Embo J* **23**(3):552-563.
25. Matsuyama S, Iwadate M, Kondo M, Saitoh M, Hanyu A, Shimizu K, Aburatani H, Mishima HK, Imamura T, Miyazono K, Miyazawa K 2003 SB-431542 and Gleevec inhibit transforming growth factor-beta-induced proliferation of human osteosarcoma cells. *Cancer Res* **63**(22):7791-8.
26. Uhl M, Aulwurm S, Wischhusen J, Weiler M, Ma JY, Almirez R, Mangadu R, Liu YW, Platten M, Herrlinger U, Murphy A, Wong DH, Wick W, Higgins LS, Weller M 2004 SD-208, a novel transforming growth factor beta receptor I kinase inhibitor, inhibits growth and invasiveness and enhances immunogenicity of murine and human glioma cells in vitro and in vivo. *Cancer Res* **64**(21):7954-61.
27. Watabe T, Nishihara A, Mishima K, Yamashita J, Shimizu K, Miyazawa K, Nishikawa S, Miyazono K 2003 TGF-beta receptor kinase inhibitor enhances

growth and integrity of embryonic stem cell-derived endothelial cells. *J Cell Biol*
163(6):1303-11.

UCSF LIBRARY

2074R

San Francisco
LIBRARY

7537585



3 1378 00753 7585

For Not to be taken
from the room.
reference

